

601833

WADD TR 61-72  
VOLUME XXXVII

203

114 pg - \$250

**RESEARCH AND DEVELOPMENT  
ON ADVANCED GRAPHITE MATERIALS  
VOLUME XXXVII. STUDIES OF GRAPHITE DEPOSITED  
BY PYROLYTIC PROCESSES**

TECHNICAL REPORT No. WADD TR 61-72, VOLUME XXXVII

MAY 1964

AIR FORCE MATERIALS LABORATORY  
RESEARCH AND TECHNOLOGY DIVISION  
AIR FORCE SYSTEMS COMMAND  
WRIGHT-PATTERSON AIR FORCE BASE, OHIO

Project No. 7350, Task No. 735002

Project No. 7381, Task No. 738102

Project No. 7-817

(Prepared under Contract No. AF 33(616)-6915 by the  
Research Laboratory, Parma, Ohio and the  
Advanced Materials Laboratory, Lawrenceburg, Tennessee  
National Carbon Company, Division of Union Carbide Corporation;  
P. H. Higgs, R. L. Finicle, R. J. Bobka,  
E. J. Seldin and K. J. Zeitsch, Authors)

## NOTICES

When Government drawings, specifications, or other data are used for any purpose other than in connection with a definitely related Government procurement operation, the United States Government thereby incurs no responsibility nor any obligation whatsoever; and the fact that the Government may have formulated, furnished, or in any way supplied the said drawings, specifications, or other data, is not to be regarded by implication or otherwise as in any manner licensing the holder or any other person or corporation, or conveying any rights or permission to manufacture, use, or sell any patented invention that may in any way be related thereto.

Qualified requesters may obtain copies of this report from the Defense Documentation Center (DDC), (formerly ASTIA), Cameron Station, Bldg. 5, 6010 Duke Street, Alexandria, Virginia, 22314.

This report has been released to the Office of Technical Services, U.S. Department of Commerce, Washington 25, D. C., in stock quantities for sale to the general public.

Copies of this report should not be returned to the Research and Technology Division, Wright-Patterson Air Force Base, Ohio, unless return is required by security considerations, contractual obligations, or notice on a specific document.

## FOREWORD

This volume is the thirty-seventh of the WADD Technical Report 61-72 series describing various phases of research and development on advanced graphite materials conducted by National Carbon Company, a Division of Union Carbide Corporation, under USAF Contract No. AF 33(616)-6915.

The work covered in this report was conducted from May, 1960 through May, 1962 at the Advanced Materials Laboratory and the Research Laboratory of National Carbon Company under the management of R. M. Bushong, Director of the Advanced Materials Project, J. C. Bowman, Director of Research, W. P. Eatherly, Assistant Director of Research and R. C. Stroup, Manager of the Advanced Materials Laboratory.

The contract for this R&D program was initiated under Project No. 7350, "Refractory Inorganic Non-Metallic Materials," Task No. 735002, "Refractory Inorganic Non-Metallic Materials: Graphitic, Project No. 7381, "Materials Application," Task No. 738102, "Materials Processes," and Project No. 7-817, "Process Development for Graphite Materials." The work was administered by the Air Force Materials Laboratory, Research and Technology Division, Major R. H. Wilson, L. J. Conlon and W. P. Conrardy acting as Project Engineers.

Other volumes in this WADD Technical Report 61-72 series are:

- |        |   |
|--------|---|
| Volume | I - Observations by Electron Microscopy of Dislocations in Graphite, by R. Sprague                                      |
| Volume | II - Applications of Anisotropic Elastic Continuum Theory to Dislocations in Graphite, by G. B. Spence                  |
| Volume | III - Decoration of Dislocations and Low Angle Grain Boundaries in Graphite Single Crystals, by R. Bacon and R. Sprague |
| Volume | IV - Adaptation of Radiographic Principles to the Quality Control of Graphite, by R. W. Wallouch                        |
| Volume | V - Analysis of Creep and Recovery Curves for ATJ Graphite, by E. J. Seldin and R. N. Draper                            |
| Volume | VI - Creep of Carbons and Graphites in Flexure at High Temperature, by E. J. Seldin                                     |

- Volume VII - High Density Recrystallized Graphite by Hot-Forming, by E. A. Neel, A. A. Kellar, K. J. Zeitsch
- Supplement - High Density Recrystallized Graphite by Hot-Forming, by G. L. Rowe and M. B. Carter
- Volume VIII - Electron Spin Resonance in Polycrystalline Graphite, by L. S. Singer and G. Wagoner
- Volume IX - Fabrication and Properties of Carbonized Cloth Composites, by W. C. Beasley and E. L. Piper
- Volume X - Thermal Reactivity of Aromatic Hydrocarbons, by I. C. Lewis and T. Edstrom
- Supplement - Thermal Reactivity of Aromatic Hydrocarbons, by I. C. Lewis and T. Edstrom
- Volume XI - Characterization of Binders Used in the Fabrication of Graphite Bodies, by E. De Ruiter, A. Halleux, V. Sandor and H. Tschanler
- Supplement - Characterization of Binders Used in the Fabrication of Graphite Bodies, by E. de Ruiter, J. F. M. Oth, V. Sandor and H. Tschanler
- Volume XII - Development of an Improved Large Diameter Fine Grain Graphite for Aerospace Applications, by C. W. Waters and E. L. Piper
- Supplement - Development of an Improved Large Diameter Fine Grain Graphite for Aerospace Applications, by R. L. Racicot and C. W. Waters
- Volume XIII - Development of a Fine-Grain Isotropic Graphite for Structural and Substrate Applications, by R. A. Howard and E. L. Piper
- Supplement - Development of a Fine-Grain Isotropic Graphite for Structural and Substrate Applications, by R. A. Howard and R. L. Racicot
- Volume XIV - Study of High Temperature Tensile Properties of ZTA Grade Graphite, by R. M. Hale and W. M. Fassell, Jr.

- Volume XV - Alumina-Condensed Furfuryl Alcohol Resins, by C. W. Boquist, E. R. Nielsen, H. J. O'Neil and R. E. Patcher
- Volume XVI - An Electron Spin Resonance Study of Thermal Reactions of Organic Compounds, by L. S. Singer and I. C. Lewis
- Volume XVII - Radiography of Carbon and Graphite, by T. C. Furnas, Jr. and M. R. Rosumny
- Volume XVIII - High Temperature Tensile Creep of Graphite, by E. J. Seldin
- Volume XIX - Thermal Stresses in Anisotropic Hollow Cylinders, by Tu-Lung Weng
- Volume XX - The Electric and Magnetic Properties of Pyrolytic Graphite, by G. Wagoner and B. H. Eckstein
- Volume XXI - Arc Image Furnace Studies of Graphite, by M. R. Null and W. Lozier
- Volume XXII - Photomicrographic Techniques for Carbon and Graphite, by G. L. Peters and H. D. Shade
- Volume XXIII - A Method for Determining Young's Modulus of Graphite at Elevated Temperatures, by S. O. Johnson and R. B. Dull
- Volume XXIV - The Thermal Expansion of Graphite in the c-Direction, by C. E. Lowell
- Volume XXV - Lamellar Compounds of Nongraphitized Petroleum Cokes, by H. F. Volk
- Volume XXVI - Physical Properties of Some Newly Developed Graphite Grades, by R. B. Dull
- Volume XXVII - Carbonization Studies of Aromatic Hydrocarbons, by I. C. Lewis and T. Edstrom
- Volume XXVIII - Polarographic Reduction of Polynuclear Aromatics, by I. C. Lewis, H. Beibecki and S. L. Bushong

- Volume XXIX - Evaluation of Graphite Materials in a Subscale Solid Propellant Rocket Motor, by D. C. Hiler and R. B. Dull
- Supplement - Evaluation of Graphite Materials in a Subscale Solid Propellant Rocket Motor, by S. O. Johnson and R. B. Dull
- Volume XXX - Oxidation-Resistant Graphite-Base Composites, by K. J. Zeitsch and J. Criscione
- Volume XXXI - Impregnation of Graphite, by C. E. Baylett, M. A. Spring and M. B. Carter
- Volume XXXII - Studies of Binder Systems for Graphite, by T. Edstrom, I. C. Lewis, R. L. Racicot and C. F. Stout
- Volume XXXIII - Investigation of Hot Worked Recrystallized Graphites, by J. H. Turner and M. B. Carter
- Volume XXXIV - Oxidation Resistant Coatings for Graphite, by D. A. Schulz, P. H. Higgs and J. D. Cannon
- Volume XXXV - Methods of Measuring Mechanical Properties of Graphite in the 20° to 2700°C Temperature Range, by M. B. Manofsky and R. B. Dull
- Volume XXXVI - Studies of the Quality of Petroleum Coke from a Pilot Scale Delayed Coker, by C. F. Stout, M. Janes and J. A. Biehl

## ABSTRACT

Work on pyrolytic or vapor-deposited graphite under this program has been limited to mechanism studies and property measurements. Methods of depositing high quality pyrolytic graphite are described with evidence as to the cause of conical growths and delaminations within the structure of the material. Results are presented on the use of hydrogen, helium and argon as diluents, and on the use of chlorine as an additive in the pyrolytic process. The mean deposition rate is shown to be a function of hydrocarbon concentration, diluent type, gas velocity, temperature and pressure. Theoretical studies of the equilibrium composition of methane as affected by changes in temperature and pressure are presented.

Feasibility studies on the production of graphite by carbon vapor deposition were conducted which indicate that nonlamellar graphite with a predetermined degree of anisotropy can be produced by this method.

Room temperature pull strength of graphite yarn has been increased as much as 360 per cent by reinforcement of the yarn with thin coatings of pyrolytic carbon; both single and multiple strand yarns have been coated.

This report has been reviewed and is approved.



W. G. RAMKE

Chief, Ceramics and Graphite Branch  
Metals and Ceramics Division  
Air Force Materials Laboratory

## TABLE OF CONTENTS

	<u>PAGE</u>
1. INTRODUCTION. . . . .	1
2. PYROLYTIC CARBON FORMED BY THERMAL DECOMPOSITION OF HYDROCARBONS. . . . .	2
2.1. Effect of Diluent Gases on Deposition Rate of Pyrolytic Carbon . . . . .	4
2.2. Effect of Pressure on Deposition Rate of Pyrolytic Carbon . . . . .	7
2.3. Efficiency of Deposition of Pyrolytic Carbon. . . . .	8
2.4. Effect of Additives on Deposition of Pyrolytic Carbon. . . . .	10
2.5. Factors Affecting the Density of Pyrolytic Carbon. . . . .	12
2.6. Effect of Substrate on the Structure of Pyrolytic Carbon. . . . .	15
2.7. Effect of Annealing on Density and Structure of Pyrolytic Carbon . . . . .	25
2.8. Physical Properties of Pyrolytic Carbon . . . . .	33
2.8.1. Specific Resistance . . . . .	33
2.8.2. Modulus of Rupture . . . . .	34
2.8.3. Coefficient of Thermal Expansion. . . . .	35
2.8.4. High Temperature Creep and Elastic Constant Determination . . . . .	36
3. PYROLYTIC CARBON COATINGS ON GRAPHITE YARN. . . . .	43
4. VAPOR DEPOSITED GRAPHITE. . . . .	62
4.1. Induction Heating for Vapor Deposition of Pyrolytic Carbon . . . . .	62
4.2. Resistance Heating for Vapor Deposition of Pyrolytic Carbon . . . . .	65
5. CONCLUSIONS. . . . .	71
5.1. Pyrolytic Carbon Formed by Thermal Decompo- sition of Hydrocarbon Gas . . . . .	71
5.2. Pyrolytic Carbon Coatings on Graphite Yarn. . . . .	72
5.3. Vapor Deposited Graphite . . . . .	72

TABLE OF CONTENTS (CONT'D.)

	<u>PAGE</u>
6. RECOMMENDATIONS . . . . .	73
6.1. Pyrolytically Coated Yarn . . . . .	73
6.2. Vapor Deposited Graphite . . . . .	73
APPENDIX I. USE OF PREDICTABILITY CHARTS IN THE CALIBRATION OF FLOWMETERS . .	74
APPENDIX II. EFFECT OF TEMPERATURE, PRESSURE AND COMPOSITION OF INFLUENT GAS ON THE EQUILIBRIUM COMPOSITION OF METHANE . . . . .	79

## LIST OF ILLUSTRATIONS

<u>FIGURE</u>		<u>PAGE</u>
1.	Sectional Drawing of Apparatus for Coating Graphite with Pyrolytic Carbon . . . . .	3
2.	Optical System Correction Curve . . . . .	4
3.	Deposition Rate of Pyrolytic Carbon as a Function of Deposition Temperature at a Total Pressure of 28 cm Hg . . . . .	5
4.	Deposition Rate of Pyrolytic Carbon as a Function of Methane Flux at a Total Pressure of 28 cm Hg . . . . .	6
5.	Deposition Rate of Pyrolytic Carbon as a Function of Total Pressure . . . . .	7
6.	Deposition Efficiency of Pyrolytic Carbon as a Function of Deposition Temperature at 28 cm Hg . . . . .	8
7.	Deposition Efficiency of Pyrolytic Carbon as a Function of Total Pressure . . . . .	9
8.	Deposition Efficiency of Pyrolytic Carbon as a Function of Methane Flux at 28 cm Hg . . . . .	10
9.	Per Cent Deposition Rate Increase Due to Use of Chlorine in Coating Gas Mixture . . . . .	11
10.	Density of Pyrolytic Carbon as a Function of Deposition Temperature at Various Total Pressures . . . . .	12
11.	The Density of Pyrolytic Carbon as a Function of Total Pressure . . . . .	13
12.	Density Comparison of Pyrolytic Carbon Deposited by Conventional and Chlorinated Processes as a Function of Temperature . . . . .	14
13.	Structure of Low Temperature Pyrolytic Carbon, 500X Deposition Temperature: 1690°C, Density: 1.36 g/cc . . . . .	15

LIST OF ILLUSTRATIONS (CONT'D.)

<u>FIGURE</u>		<u>PAGE</u>
14.	Structure of a Medium Density Pyrolytic Carbon, 500 X Deposition Temperature: 2000°C, Density: 1.768 g/cc . . . . .	16
15.	Structure of a High Density Pyrolytic Carbon, 500 X Deposition Temperature: 2200°C, Density: 2.24 g/cc . . . . .	16
16.	Pyrolytic Carbon Deposited on a Lapped Graphite Surface, 500X . . . . .	17
17.	Pyrolytic Carbon Deposited on an Unlapped Graphite Surface, 500X . . . . .	17
18.	Sectional Drawing of an Apparatus for the Depo- sition of Pyrolytic Carbon - Upper Section . . . . .	18
19.	Apparatus for the Deposition of Pyrolytic Carbon - Lower Section . . . . .	19
20.	Comparison of Good and Poor Pyrolytic Carbon Deposition. . . . .	20
21.	Appearance of Conical Surface Growths as a Function of Distance Between Gas Inlet and Substrate . . . . .	21
22.	High Density Pyrolytic Carbon with Needle Structure . . . . .	22
23.	Illustration of a Soot Particle Originating a Large Cone in an Otherwise Needle Structure Pyrolytic Carbon . . . . .	23
24.	Structural and Density Changes in Pyrolytic Carbon as a Result of Annealing, 500X . . . . .	26
25.	Structural and Density Changes in Pyrolytic Carbon as a Result of Annealing, 500X. . . . .	27

LIST OF ILLUSTRATIONS (CONT'D.)

<u>FIGURE</u>		<u>PAGE</u>
36.	Structural and Density Changes in Pyrolytic Carbon as a Result of Annealing, 500X . . . . .	28
27.	Structure and Density Changes in Pyrolytic Carbon as a Result of Annealing, 500X. . . . .	29
28.	Structural and Density Changes in Pyrolytic Carbon as a Result of Annealing, 500X . . . . .	30
29.	Density Changes in Pyrolytic Carbon as a Result of Annealing versus Deposition Temperature . . . . .	32
30.	Volumetric and C-Direction Shrinkage of Pyrolytic Carbon as a Result of Annealing . . . . .	33
31.	Specific Resistance of "As Deposited" and "As Annealed" Pyrolytic Carbon versus Density . . . . .	34
32.	Creep of "As Deposited" Pyrolytic Carbon versus Time and Temperature . . . . .	37
33.	Creep of Annealed Pyrolytic Carbon versus Time and Temperature . . . . .	38
34.	Creep of Pyrolytic Carbon versus Time and Temperature, "A" Orientation . . . . .	39
35.	Creep of Pyrolytic Carbon versus Time and Temperature, "B" Orientation . . . . .	40
36.	Creep of ATJ Graphite . . . . .	41
37.	Schematic Drawing of Apparatus for Coating Graphite Yarn with Pyrolytic Carbon . . . . .	43
38.	Equipment for Coating Graphite Yarn with Pyrolytic Carbon . . . . .	44
39.	Interior View of Yarn Coating Apparatus in Operation . . . . .	45

LIST OF ILLUSTRATIONS (CONT'D.)

<u>FIGURE</u>		<u>PAGE</u>
40.	Pyrolytic Yarn Pull-Strength Testing Apparatus . . .	46
41.	Pull Strength of Graphite Yarn Coated with Pyrolytic Carbon at a Process Speed of 80 in/min as a Function of the Methane Concentration in the Coating Gas . . . . .	47
42.	Pull Strength of Graphite Yarn Coated with Pyrolytic Carbon at a Process Speed of 100 in/min as a Function of the Methane Concentration in the Coating Gas . . . . .	48
43.	Pull Strength of Graphite Yarn Coated with Pyrolytic Carbon at a Process Speed of 120 in/min as a Function of the Methane Concentration in the Coating Gas . . . . .	49
44.	Pull Strength of Graphite Yarn Coated with Pyrolytic Carbon at a Process Speed of 150 in/min as a Function of the Methane Concentration in the Coating Gas . . . . .	50
45.	Pull Strength of Graphite Yarn Coated with Pyrolytic Carbon at a Process Speed of 175 in/min as a Function of the Methane Concentration in the Coating Gas . . . . .	51
46.	Pull Strength of Graphite Yarn Coated with Pyrolytic Carbon at a Process Speed of 188 in/min as a Function of the Methane Concentration in the Coating Gas . . . . .	52
47.	Pull Strength of Graphite Yarn Coated with Pyrolytic Carbon at a Process Speed of 200 in/min as a Function of the Methane Concentration in the Coating Gas . . . . .	53
48.	Pull Strength of Graphite Yarn Coated with Pyrolytic Carbon at a Process Speed of 225 in/min as a Function of the Methane Concentration in the Coating Gas . . . . .	54

LIST OF ILLUSTRATIONS (CONT'D.)

<u>FIGURE</u>		<u>PAGE</u>
49.	Comparison of Uncoated (Top) and Pyrolytically Coated (Bottom) Graphite Yarn . . . . .	56
50.	Graphite Yarn Fibers Coated with Pyrolytic Carbon, 1000 X . . . . .	56
51.	A Strand of Graphite Yarn Illustrating Depth of Penetration of Pyrolytic Carbon into the Individual Fibers, 500X. . . . .	57
52.	A Comparison of a Single Strand of Uncoated (Top) and Pyrolytically Coated (Bottom) Graphite Yarn, 12X . . . . .	58
53.	Single Strand Graphite Yarn Coated with Pyrolytic Carbon and Bent at 170° Angle, 12X . . . . .	59
54.	Single Strand of Pyrolytically Coated Graphite Yarn Relaxed from 170 to 45° Angle, 12X. . . . .	59
55.	Single Strand of Pyrolytically Coated Graphite Yarn Relaxed from 170 to 20° Angle, 12X. . . . .	60
56.	Single Strand of Pyrolytically Coated Graphite Yarn Completely Relaxed from 170° Angle, 12X . . .	60
57.	Graphite Assembly for Production of Vapor Deposited Pyrolytic Graphite by Induction Heating. . . .	62
58.	Macrograph of Vapor Deposited Pyrolytic Carbon, 12X . . . . .	63
59.	Pyrolytic Carbon by Vapor Deposition, 50X, 100X and 250X . . . . .	64
60.	Porosity Characteristic of Vapor Depositing Carbon . . . . .	65
61.	Apparatus for Deposition of Vapor Deposited Graphite by Resistance Heating . . . . .	66

LIST OF ILLUSTRATIONS (CONT'D.)

FIGURE		PAGE
62.	Pyrolytic Graphite Produced by Vapor De- position . . . . .	67
63.	Porosity Characteristics of Vapor Deposited Graphite . . . . .	68
64.	Structure Gradient in Vapor Deposited Pyrolytic Graphite, 500X . . . . .	69
65.	Isotropic Structure of Vapor Deposited Pyrolytic Graphite, 500X . . . . .	69
66.	Predictability Chart for Use in Flowmeter Calibration . . . . .	75
67.	Variation of $\log K_p$ with Temperature . . . . .	83
68.	Equilibrium Composition ( $\frac{x}{a}$ ) Variation with $\log K_p$ and Pressure, No Added Gases . . . . .	84
69.	Equilibrium Composition ( $\frac{x}{a}$ ) of the Pyrolysis Mixture at $P = 0.1$ atm s Moles $H_2$ Added to Give a dilution Ratio $r = \frac{s}{a}$ . . . . .	89
70.	Equilibrium Composition ( $\frac{x}{a}$ ) of the Pyrolysis Mix- ture at $P = 1$ atm s Moles $H_2$ Added to Give a Dilution Ratio $r = \frac{s}{a}$ . . . . .	90
71.	Equilibrium Composition ( $\frac{x}{a}$ ) of the Pyrolysis Mix- ture at $P = 5$ atm s Moles $H_2$ Added to Give a Dilution Ratio $r = \frac{s}{a}$ . . . . .	91
72.	Maximum Permissible Temperatures for Zero Yields of Carbon . . . . .	92
73.	Equilibrium Composition ( $\frac{x}{a}$ ) of the Pyrolysis Mix- ture at $P = 0.1$ atm m Moles Inert Gas Added to Give a Dilution Ratio $t = \frac{m}{a}$ . . . . .	96

LIST OF ILLUSTRATIONS (CONT'D.)

<u>FIGURE</u>		<u>PAGE</u>
74.	Equilibrium Composition ( $\frac{x}{a}$ ) of the Pyrolysis Mixture at P = 1 atm m Moles Inert Gas Added to Give a Dilution Ratio $t = \frac{m}{a}$ . . . . .	97
75.	Equilibrium Composition ( $\frac{x}{a}$ ) of the Pyrolysis Mixture at P = 5 atm m Moles Inert Gas Added to Give a Dilution Ratio $t = \frac{m}{a}$ . . . . .	98

## LIST OF TABLES

<u>TABLE</u>	<u>PAGE</u>
1. Physical Changes in Pyrolytic Carbon upon Annealing to 2800°C . . . . .	31
2. Rupture Strengths of Pyrolytic Carbon . . . . .	35
3. Thermal Expansion of Pyrolytic Carbon . . . . .	36
4. The Elastic Constant K for Pyrolytic Graphite . . . . .	42
5. Typical Results of Physical Tests on Coated and Uncoated Ten-Strand Graphite Yarn . . . . .	55
6. Comparison of Tenacity for Uncoated and Pyrolytic Coated Graphite Yarn . . . . .	61
7. Data on Ball Floats . . . . .	77
8. Sample Calibration Table for Air at 70°F and 1 atm in Flowmeter No. 1 with Sapphire Ball . . . . .	78
9. The Equilibrium Constant for the Pyrolysis of Methane . . . . .	82
10. Equilibrium Composition of the Pyrolysis Mixture with no Added Gases . . . . .	85
11. Equilibrium Composition of the Pyrolysis Mixture; Hydrogen Added, No Inert Gas Added P = 0.1 atm . . . . .	86
12. Equilibrium Composition of the Pyrolysis Mixture; Hydrogen Added, No Inert Gases Added P = 1 atm . . . . .	87
13. Equilibrium Composition of the Pyrolysis Mixture; Hydrogen Added, No Inert Gas Added P = 5 atm . . . . .	88
14. Maximum Permissible Temperatures for Zero Yields of Carbon . . . . .	92

LIST OF TABLES (CONT'D.)

<u>TABLE</u>		<u>PAGE</u>
15.	Equilibrium Composition of the Pyrolysis Mixture; Inert Gas Added, No Hydrogen Added P = 0.1 atm . . . . .	93
16.	Equilibrium Composition of the Pyrolysis Mixture; Inert Gas Added, No Hydrogen Added P = 1 atm . . . . .	94
17.	Equilibrium Composition of the Pyrolysis Mixture; Inert Gas Added, No Hydrogen Added P = 5 atm . . . . .	95

## 1. INTRODUCTION

Pyrolytic carbon or graphite is a material formed by the thermal decomposition of a carbonaceous gas or by the condensation of sublimed carbon vapor. The material formed by thermal decomposition is lamellar in nature and is characterized by high strength, excellent thermal conductivity in the A-B direction, poor thermal conductivity in the C direction and a high degree of anisotropy. The vapor deposited graphite on the other hand has a finely-divided, randomly-oriented graphite structure. The vapor deposited graphite can exhibit complete or varying degrees of isotropy depending upon the conditions of vaporization and condensation.

Graphite and carbon yarn have also been coated with pyrolytic carbon to mechanically increase the strength of the yarn. Microthin coatings of pyrolytic carbon applied to graphite yarn can produce a yarn with a strength 360 per cent of that of the original material. Depending upon the conditions of deposition, the yarn can be made quite stiff(simulating a fine wire) or flexible as it was in its original state. In any case, this yarn when woven into cloth should significantly improve the strength and usefulness of the carbon or graphite cloth.

---

Manuscript released by the authors July 1963 for publication as a WADD Technical Documentary Report.

## 2. PYROLYTIC CARBON FORMED BY THERMAL DECOMPOSITION OF HYDROCARBONS

---

The formation of pyrolytic carbon is an involved process consisting of the thermal decomposition of a carbon bearing gas in association with gas phase reactions. The structure and physical properties of the material are directly affected by the following process variables: (a) temperature of the substrate, (b) partial pressure of the hydrocarbon, (c) partial pressure of the diluent (if used), (d) flow rate of the gas (or gases), (e) length of the path between the point of introduction of the coating gas and the substrate, (f) velocity of the gaseous impingement, (g) total pressure of the system, and (h) substrate surface structure.

The initial work was conducted in a water-cooled stainless steel vacuum chamber. The sample used was an R-0020 (experimental grade) graphite strip 0.4 cm by 0.5 cm by 11.5 cm which was resistively heated. A schematic detailed drawing of the apparatus is shown in Figure 1. The gas manifold was designed as a mixing system so that different combinations of gases could be fed into the chamber at known flow rates and partial pressures. As the gases left the manifold, they passed through a calcium sulfate drying tower and were diffused, upon entering the chamber, by a multiple jet nozzle. A magnetically driven fan, located in series with the nozzle, further mixed the gases as they entered the nozzle. Rotameters were used to meter the gas flow into the system and the rates were calculated by use of the predictability charts supplied with the meters. (See sample calculation, Appendix I). Although the flow rates were varied during the experimental series, the total pressure of the system could be held constant by controlling the pressure independently with a cold-trapped Cartesian manostat. The system pressure was monitored by a mercury manometer and a thermocouple gauge.

The graphite samples were supported in a horizontal position by water-cooled copper electrodes set in the base plate. Deformation of the sample by thermal expansion was eliminated by holding the sample with graphite clamps, which permitted the sample to slip as it was heated. Careful adjustment of the clamps allowed this slipping to take place without electrical arcing.

The surface temperature of the sample was read with a standard optical pyrometer which was sighted through a right angle prism mounted over the top observation port. For this particular sample configuration, the temperature was found to be essentially constant over the center 8 cm of the sample. The plot of the correction curve for this optical system is shown in Figure 2. The correction given was added to the

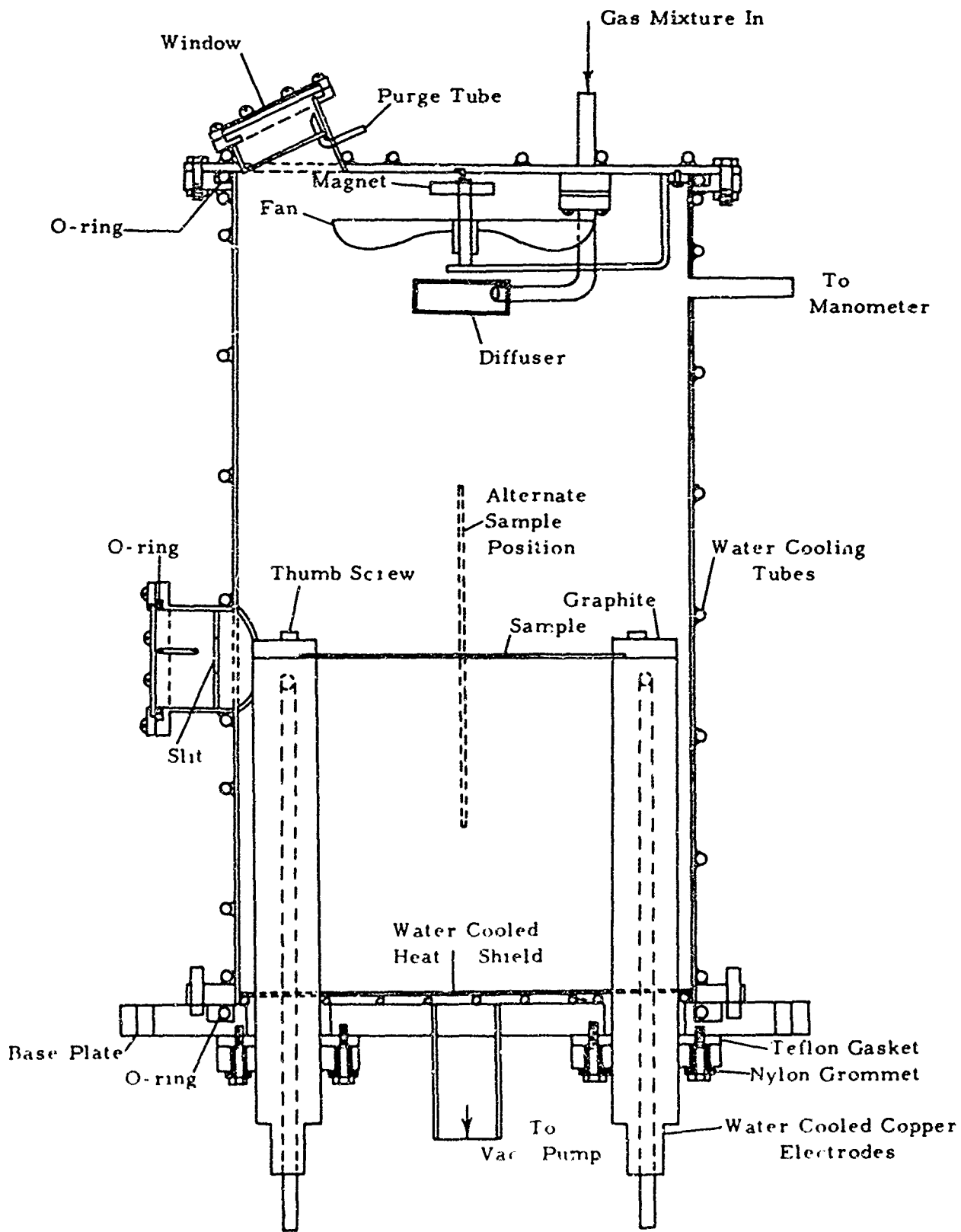


Figure 1. Secti nal Drawing of Apparatus for Coating Graphite with Pyrolytic Carbon

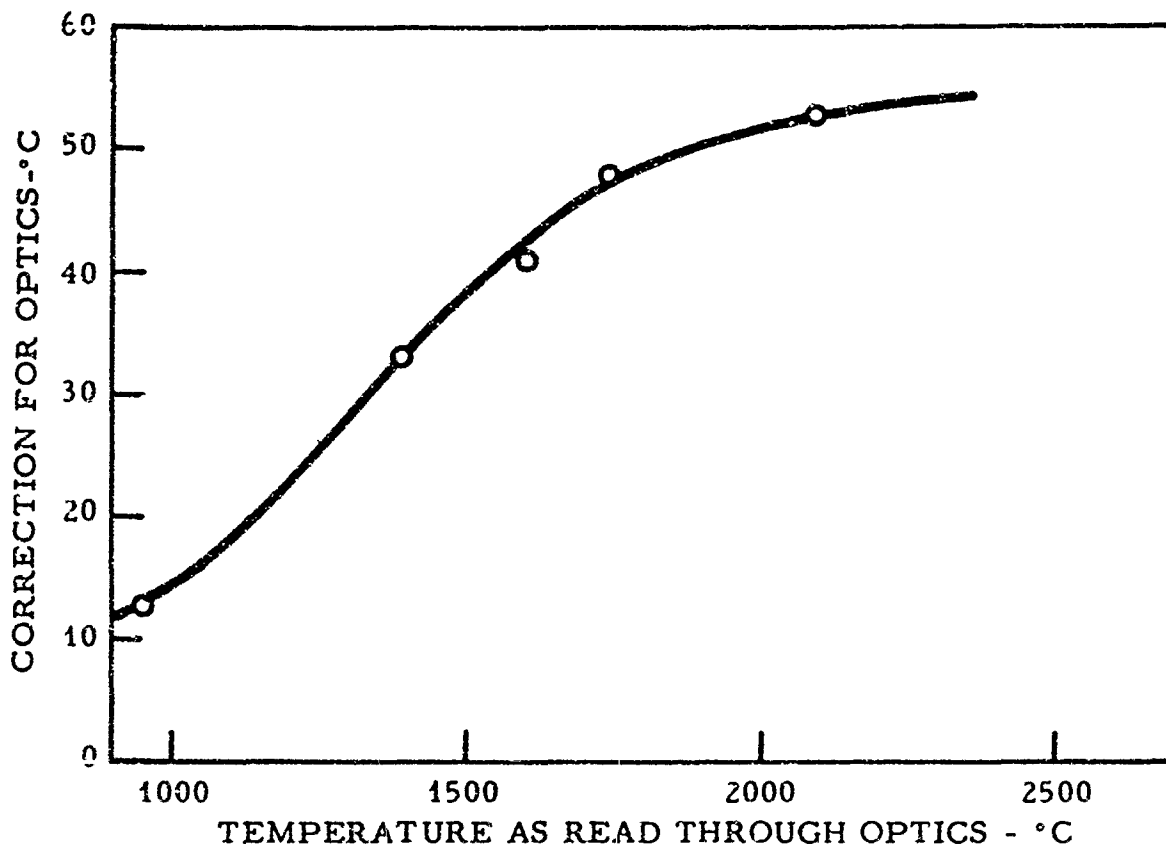


Figure 2. Optical System Correction Curve

actual pyrometer reading.

The following procedure was used in all experiments: the sample was raised to the desired temperature in vacuo, and the flow rate and pressure of the diluent gas were adjusted to the desired values. When equilibrium was obtained, the methane was admitted at the desired partial pressure and deposition of the pyrolytic carbon was continued under constant conditions for the duration of the experiment. The surface temperature of the sample was kept constant by increasing the power input to compensate for the decreasing resistance of the sample. At the end of the specified coating period, the methane flow was stopped and the power held constant until the residual methane was exhausted. The temperature of the sample was again measured to determine the effect of soot dispersion, if any, in the gaseous atmosphere.

#### 2.1. Effect of Diluent Gases on Deposition Rate of Pyrolytic Carbon

The effect of different diluent gases on the deposition rate

at various temperatures is shown in Figure 3. The deposition rate is essentially the same when either argon or helium is used as the diluent. Hydrogen used as the diluent, however, gives a somewhat lower deposition rate than argon or helium. The deposition rate is expressed as grams of carbon deposited per square centimeter of original surface area per unit time. This method of expression does not take into account the change in surface area due to the deposition and therefore defines the maximum deposition rate.

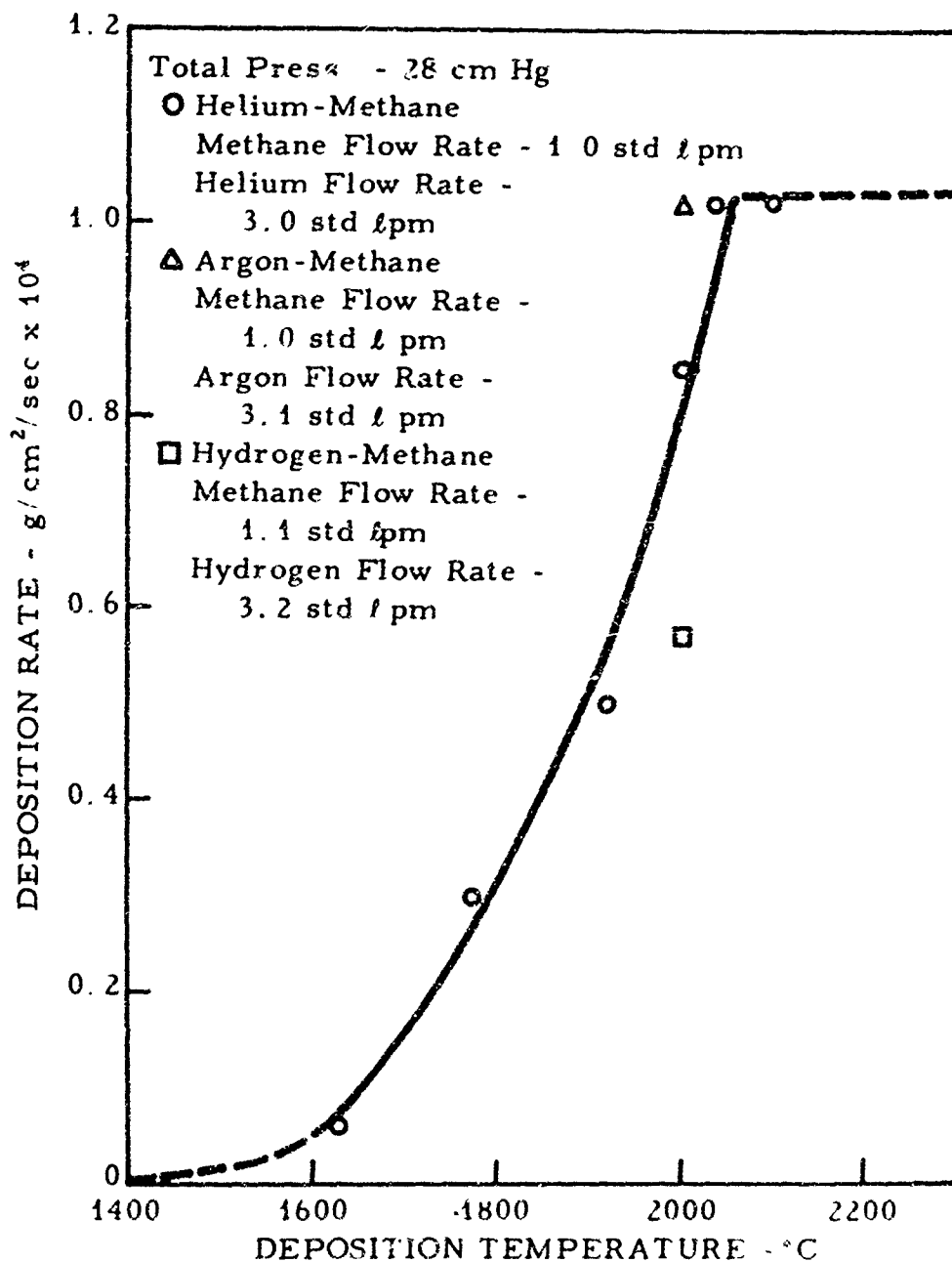


Figure 3. Deposition Rate of Pyrolytic Carbon as a Function of Deposition Temperature at a Total Pressure of 28 cm Hg

Since the maximum deposition rate was experienced at 2000°C, this temperature was used as a basis for investigation of the effects of other variables on the deposition rate. Therefore, at a constant temperature of 2000°C and a total pressure of 28 cm Hg, the concentration of methane in the chamber was increased to determine the effect of the availability of carbon on the deposition rate. The term "flux" is used to express the gas concentrations. This term is based on the number of moles of gas per square centimeter of interior surface area of the chamber (5560 cm<sup>2</sup>) per unit time. When the results were plotted, the effect of the methane concentration in conjunction with He, Ar and H<sub>2</sub> as diluent gases were clearly illustrated (see Figure 4). The use of argon or helium as diluents gave essentially the same deposition rate while the use of hydrogen lowered the deposition rate by approximately 50 per cent. The lower deposition rate indicated the importance of the gas phase reactions and also demonstrated the displacement of the equilibrium of the reaction to the left,  $(\text{CH}_4 \rightleftharpoons \text{C} + 2\text{H}_2)$  thus decreasing the yield of carbon. (See Appendix II)

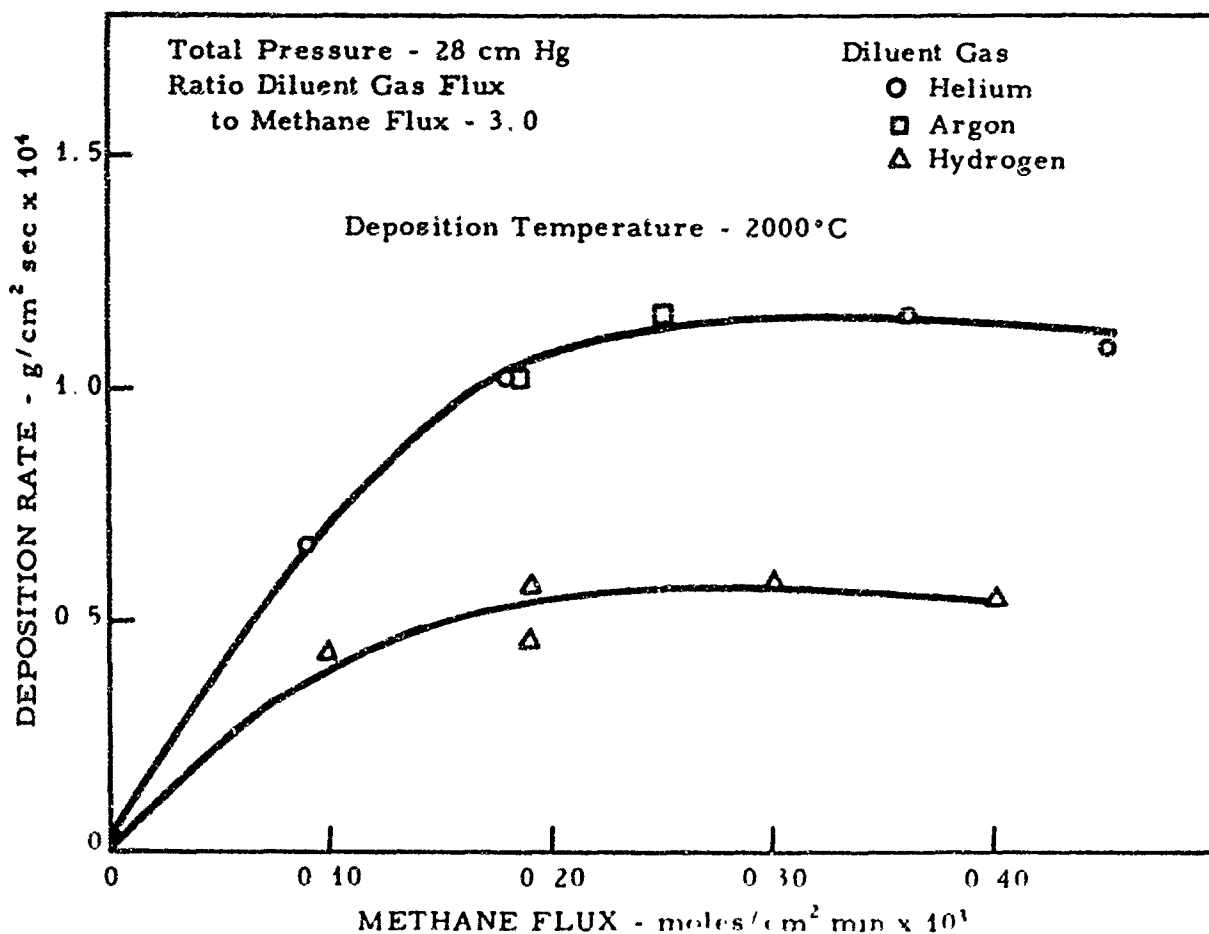


Figure 4. Deposition Rate of Pyrolytic Carbon as a Function of Methane Flux at a Total Pressure of 28 cm Hg

## 2.2. Effect of Pressure on Deposition Rate of Pyrolytic Carbon

Investigation of the effect of the total pressure of the system showed a marked increase in the deposition rate from 1 cm to about 30 cm. From that point to atmospheric pressure the deposition rate continued to increase, but at a much smaller rate. Figure 5 shows a plot of the deposition rate as a function of the total pressure of the system.

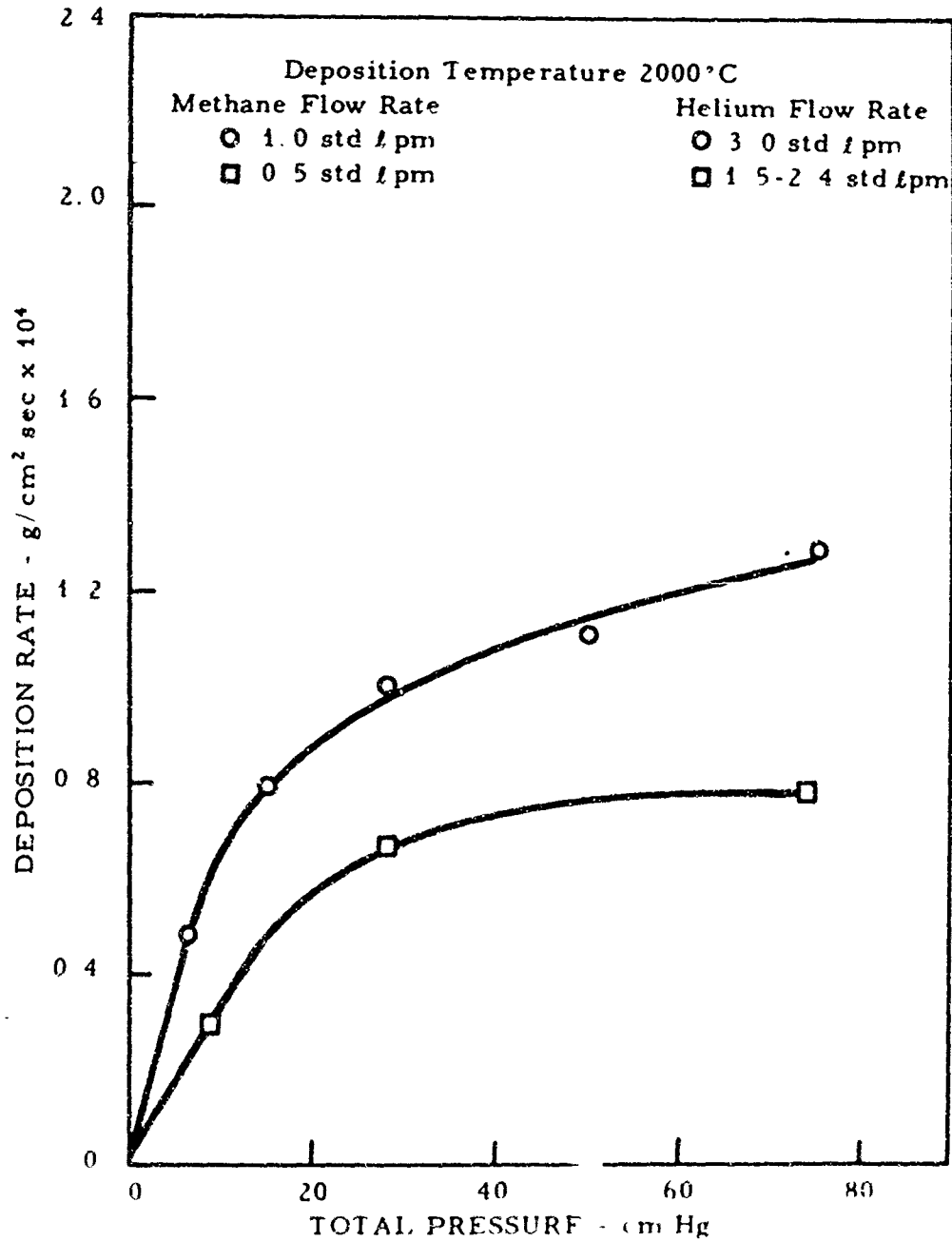


Figure 5. Deposition Rate of Pyrolytic Carbon as a Function of Total Pressure

### 2.3. Efficiency of Deposition of Pyrolytic Carbon

The deposition efficiency, which is defined as the ratio of the number of moles of carbon deposited to the number of moles of carbon available in the methane, was investigated as a function of temperature, pressure, and methane flux. The efficiency followed the same general trend as the deposition rate in that it increased with increasing temperature and also increased with increasing pressure up to about 28 cm Hg where it began to level off. The effect of temperature and pressure on the deposition efficiency is illustrated in Figures 6 and 7 respectively.

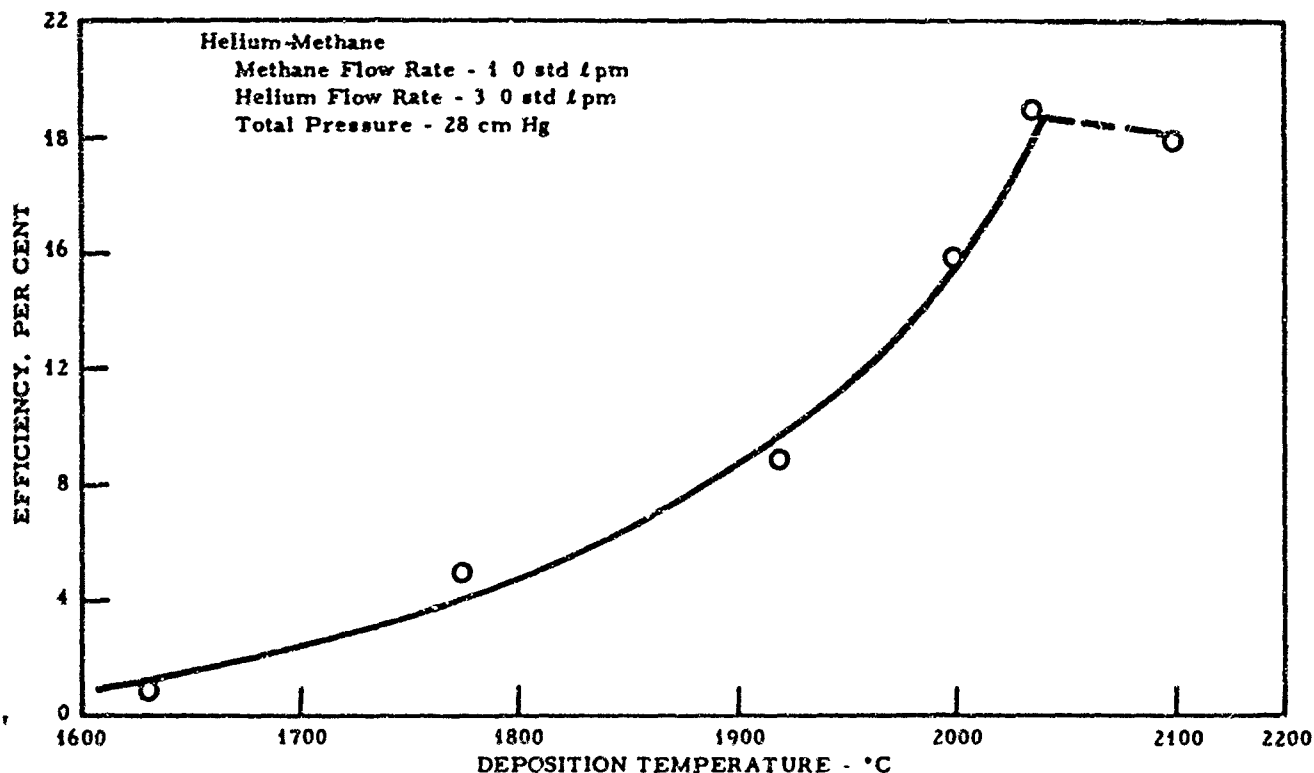


Figure 6. Deposition Efficiency of Pyrolytic Carbon as a Function of Deposition Temperature at 28 cm Hg

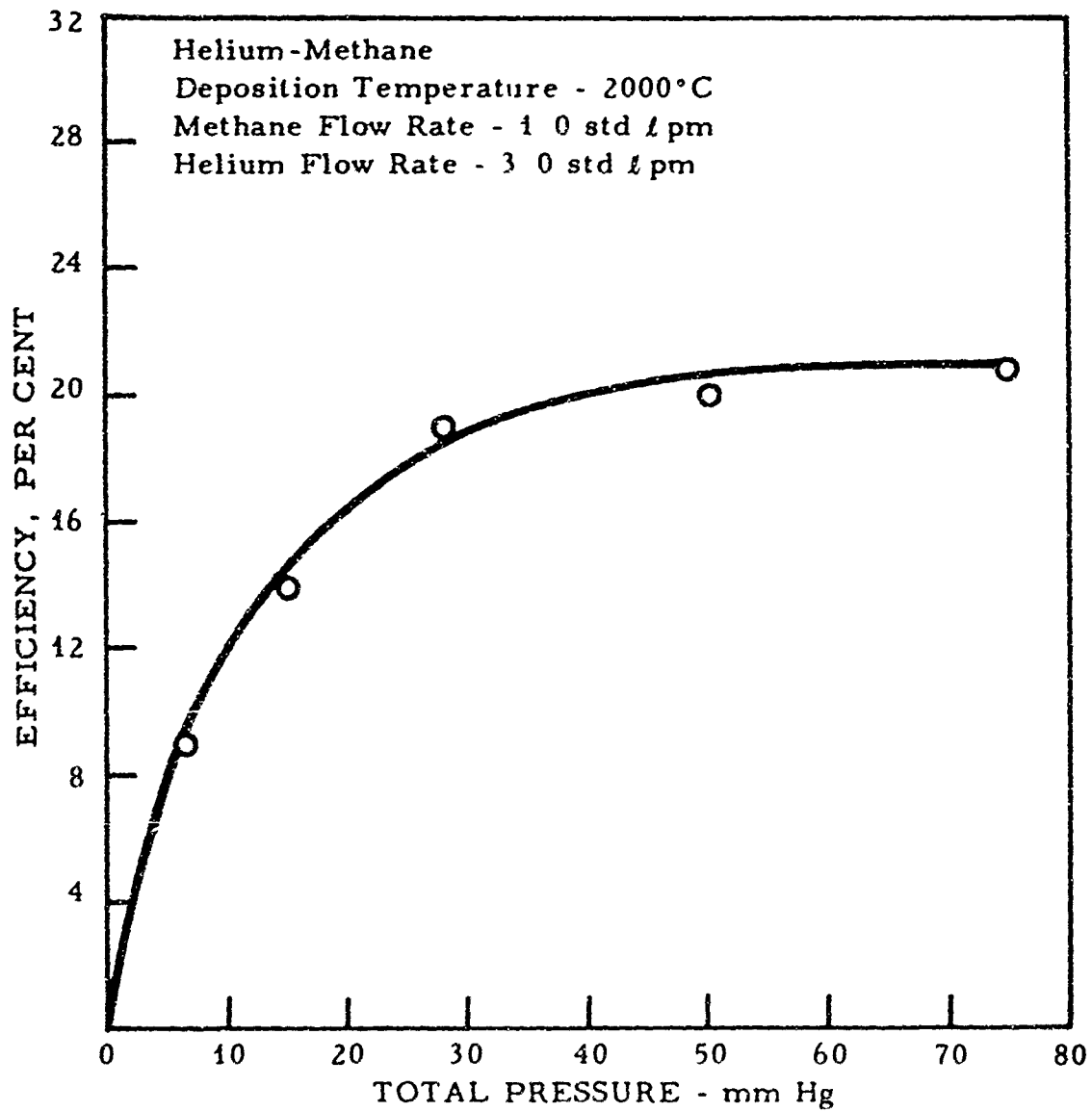


Figure 7. Deposition Efficiency of Pyrolytic Carbon as a Function of Total Pressure

In Figure 8, the deposition efficiency is plotted as a function of the methane flux. It is interesting to note (Figure 8) that the deposition efficiency was essentially the same when helium or argon was used as the diluent while the efficiency was much less when hydrogen was used as the diluent gas. This set of curves further illustrates the effect a chemically active specie of gas has on the deposition rate and efficiency.

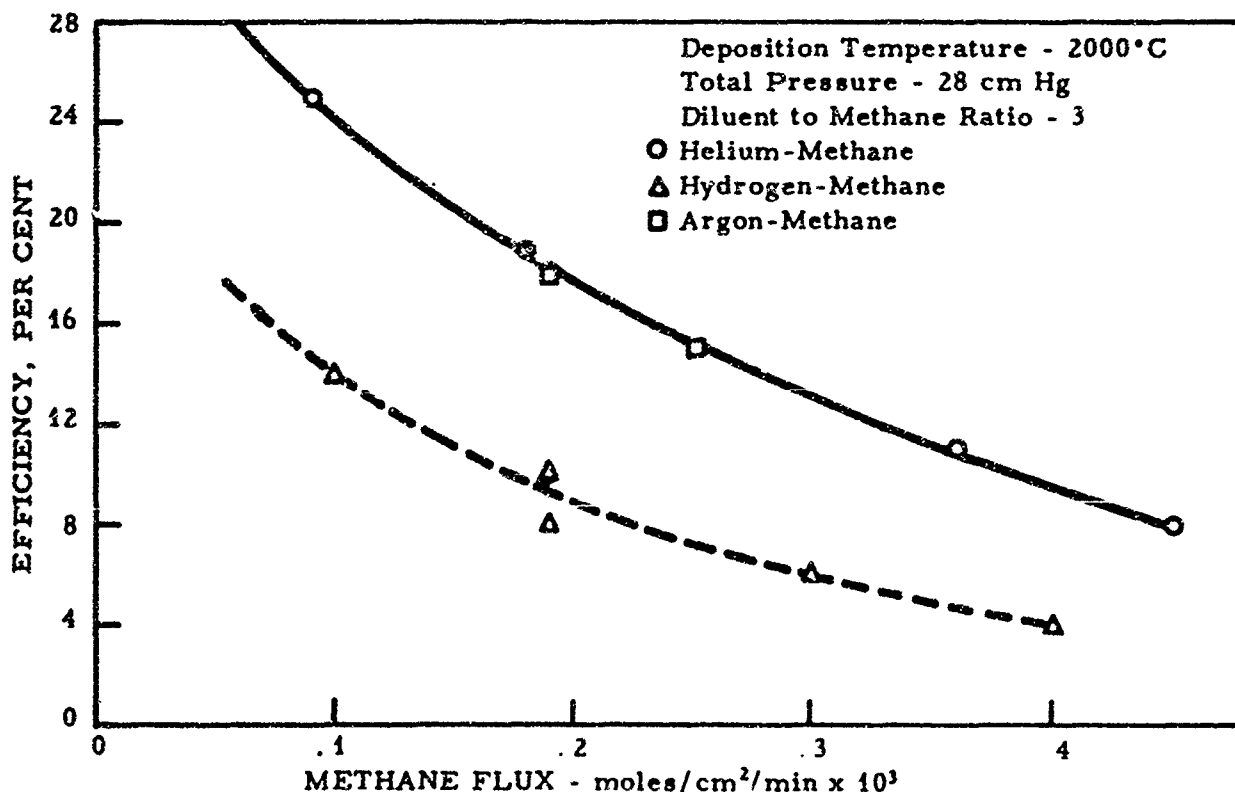


Figure 8. Deposition Efficiency of Pyrolytic Carbon as a Function of Methane Flux at 28 cm Hg

#### 2.4. Effect of Additives on Deposition of Pyrolytic Carbon

Along with the investigation of the efficiency as a function of the above parameters, a study was conducted to determine the effect on the deposition process of the addition of chlorine to the coating gas mixture. The results of this study showed that the addition of a certain concentration of chlorine was very beneficial.

Figure 9 shows the increase in deposition rate, as a function of temperature, which occurred when chlorine was added to the coating gas mixture. The additive level of chlorine was quite small and was within a critical range. The basic gas composition used for these experiments consisted of a 95 per cent argon, 5 per cent methane mixture with a total flow of 84 std. ft<sup>3</sup>/hr. Additive levels between 0.0327 and 1.175 parts per hundred, by volume, of the base gas flow were investigated. Within this range, it was determined that an additive level of 0.179 parts per hundred chlorine produced the most beneficial effects; i. e., increased efficiency, increased density, smoother and less lamellar coatings. When, at 2000°C, an additive level of 0.357 parts per hundred chlorine was used, severe laminations occurred but the density remained essentially constant at 2.2 g/cc. When the chlorine level was increased to 1.175 parts per hundred the severity of the laminations increased and the density decreased to 1.87 g/cc.

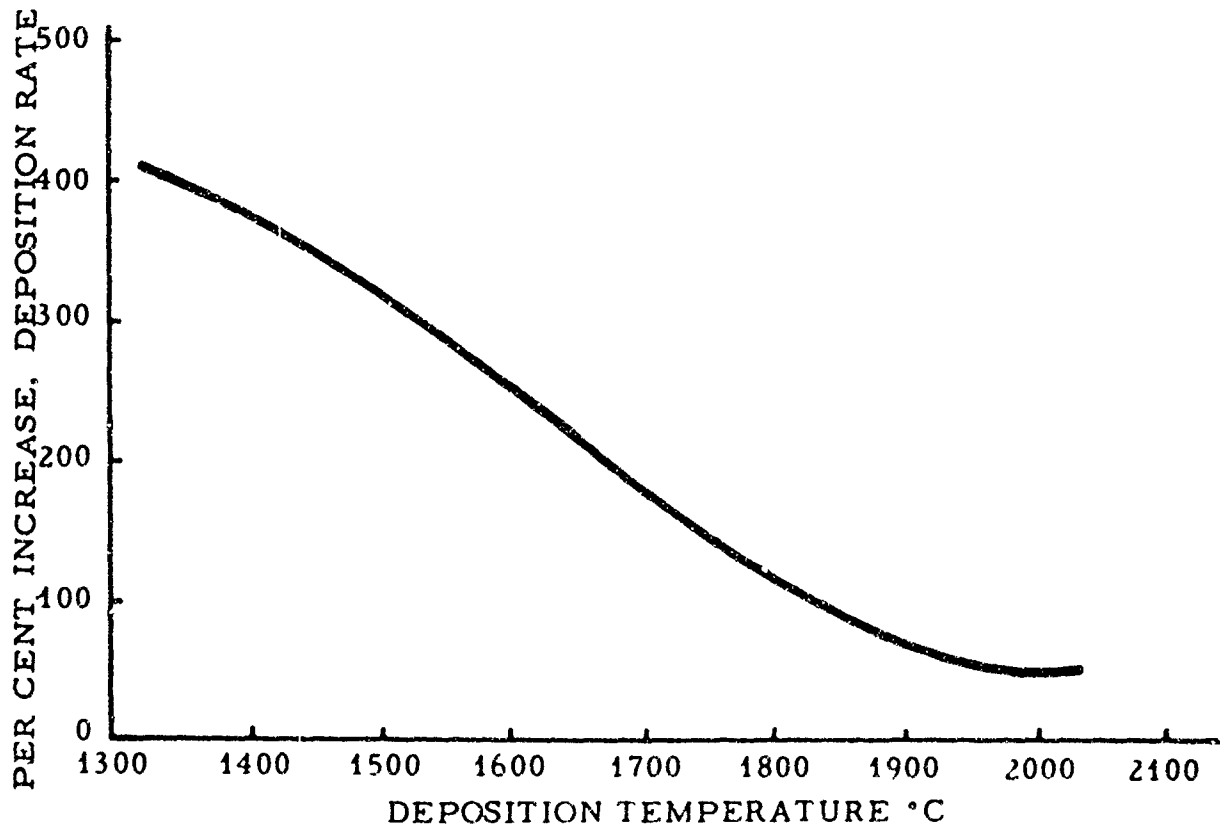


Figure 9. Per Cent Deposition Rate Increase Due to Use of Chlorine in Coating Gas Mixture

## 2.5. Factors Affecting the Density of Pyrolytic Carbon

The density of the pyrolytic carbon was measured by two principal methods; (a) the standard floatation method where the sample was immersed in a solution of bromoform and ethyl alcohol, the density of the solution was adjusted until the sample neither floated nor sank, and the density of the solution was measured by a Westphal balance, and (b) by water displacement. These densities were checked by a pressurized helium technique and a pore volume analysis. All methods gave good agreement.

The density of pyrolytic carbon is dependent on several factors, chief among which are the deposition temperature and pressure. In Figures 10 and 11 the density is plotted as a function of temperature

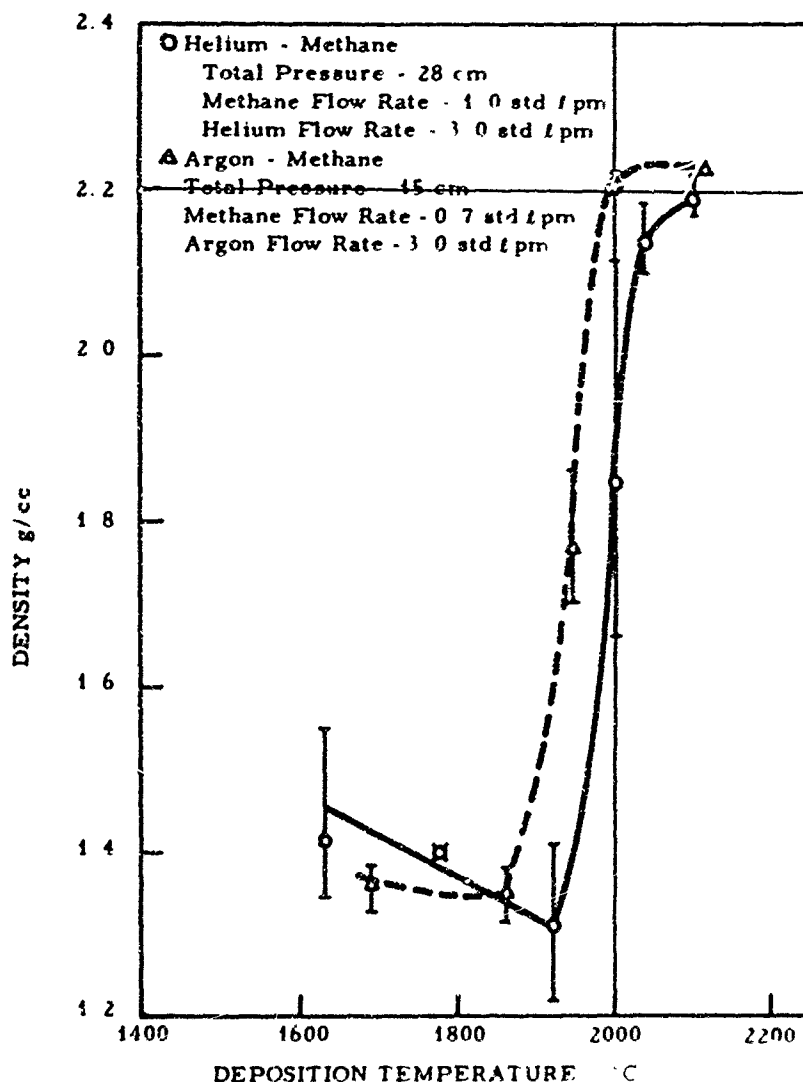


Figure 10. Density of Pyrolytic Carbon as a Function of Deposition Temperature at Various Total Pressures

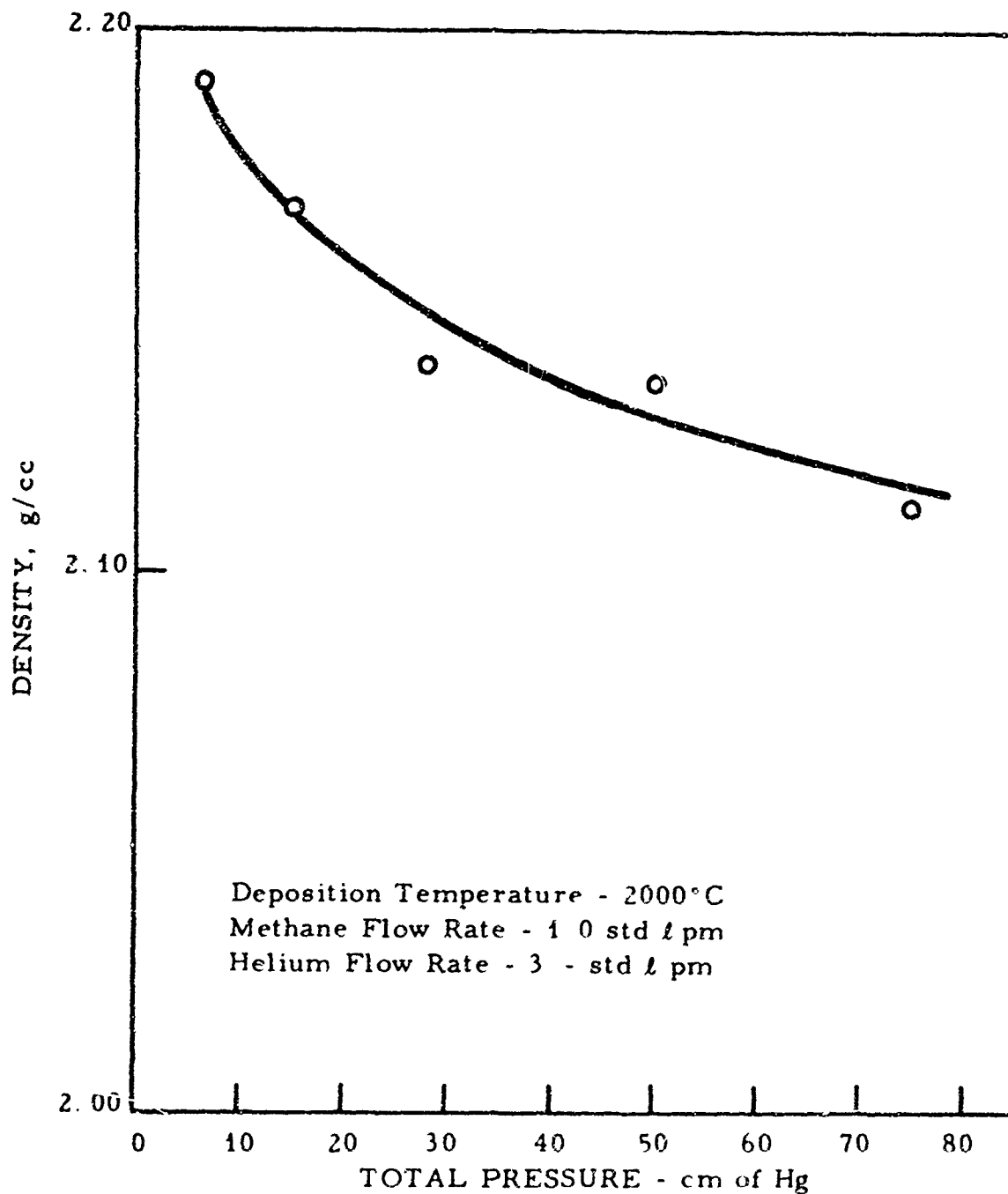


Figure 11. The Density of Pyrolytic Carbon as a Function of Total Pressure

and pressure. Examination of Figure 10 shows that the density of the pyrolytic carbon produced with argon as the diluent was slightly greater than with helium. Consideration of the data presented in Figure 11, however, shows that this density increase could be predicted since the argon-methane deposition was carried out at a lower pressure than that of the helium-methane deposition. Figure 11 also illustrates the tendency for the

density to level off at pressures in excess of 28 cm Hg.

Figure 12, a plot of the density as a function of deposition temperature at atmospheric pressure, shows the effect of the addition

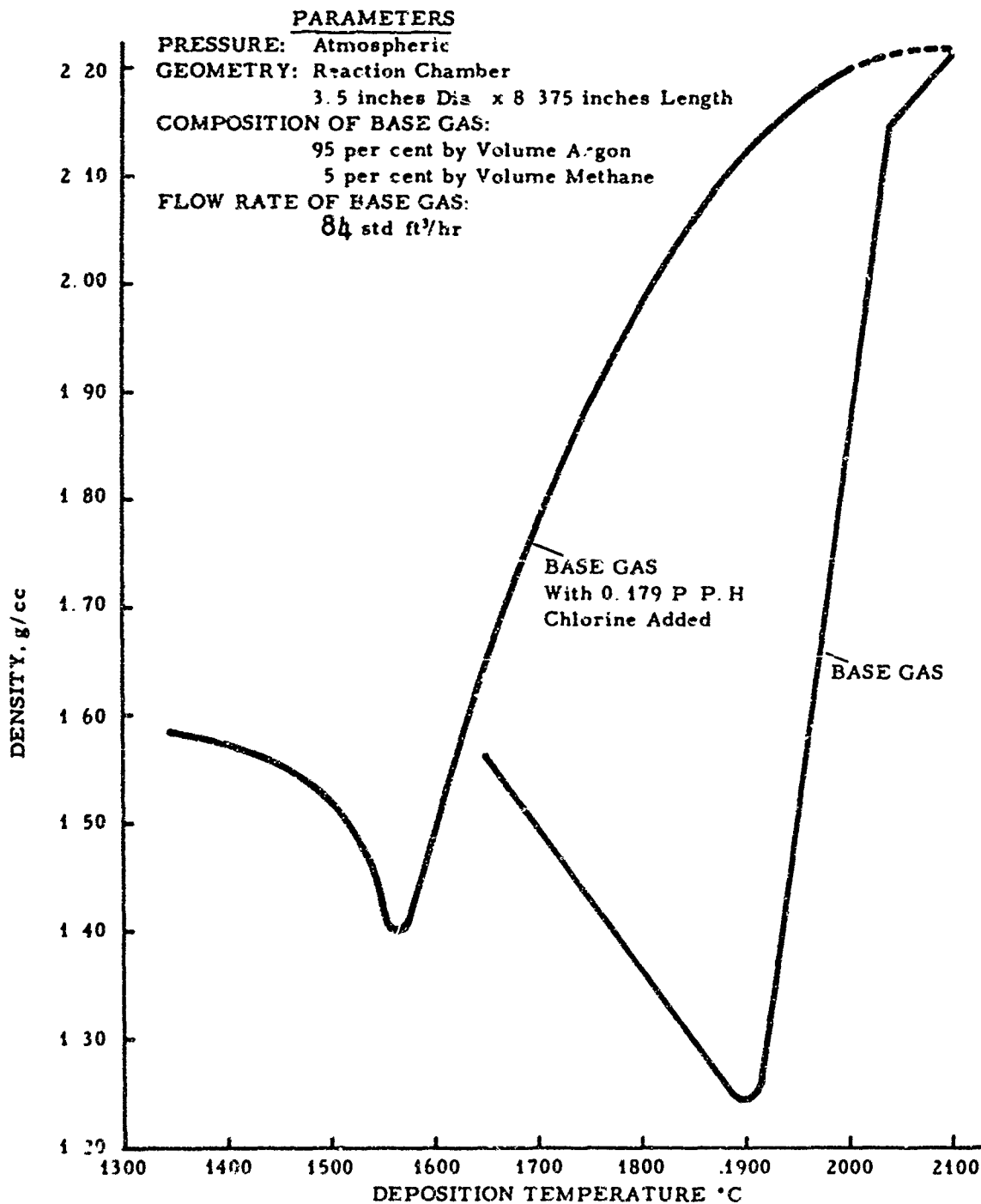


Figure 12. Density Comparison of Pyrolytic Carbon Deposited by Conventional and Chlorinated Processes as a Function of Temperature

of 0.179 parts per hundred chlorine to the coating gas mixture. The curve representing the conventional process (no chlorine added) follows the density profile presented in Figures 10 and 11. However, the addition of the chlorine raised, and moved to a lower temperature, the typical minimum density of the unchlorinated pyrolytic carbon and allowed near theoretical densities to be achieved at 2000°C.

## 2.6. Effect of Substrate on the Structure of Pyrolytic Carbon

Typical low, medium and high density pyrolytic carbon structures are shown in Figures 13, 14 and 15. The material has a highly-oriented, conical structure and, in Figure 15, is laminated. An investigation as to the cause of these conical growths was begun. The first step in this direction was to study the effect of the substrate surface on the deposited structure. In this area, dry lapping was found to be the most effective means of preparing the graphite substrate. Comparisons of material deposited on lapped and unlapped surfaces, respectively, are shown in Figures 16 and 17. The substrate in both cases was ATJ. In the ensuing experiments, it became evident that cones could occur in otherwise perfect pyrolytic bodies and that the number of cones per unit area might increase gradually from one end of the body to the other. This indicated that these disturbances of the pyrolytic body were not necessarily a random phenomenon and could be dependent on the geometry of the coating apparatus.

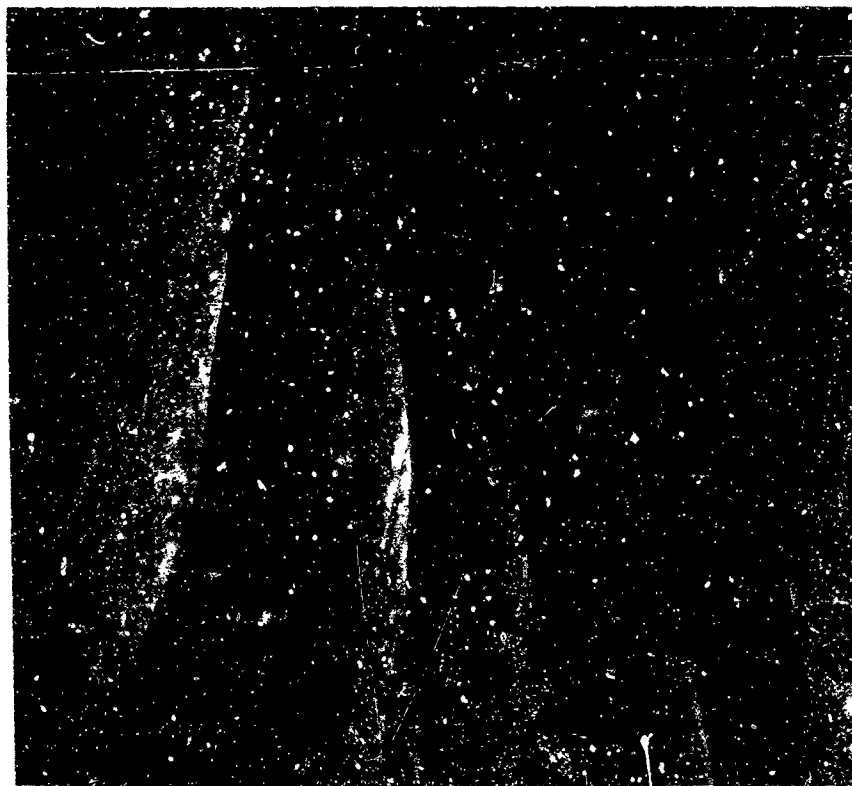


Figure 13. Structure of Low Temperature Pyrolytic Carbon, 500X  
Deposition Temperature: 1690°C, Density: 1.36 g/cc

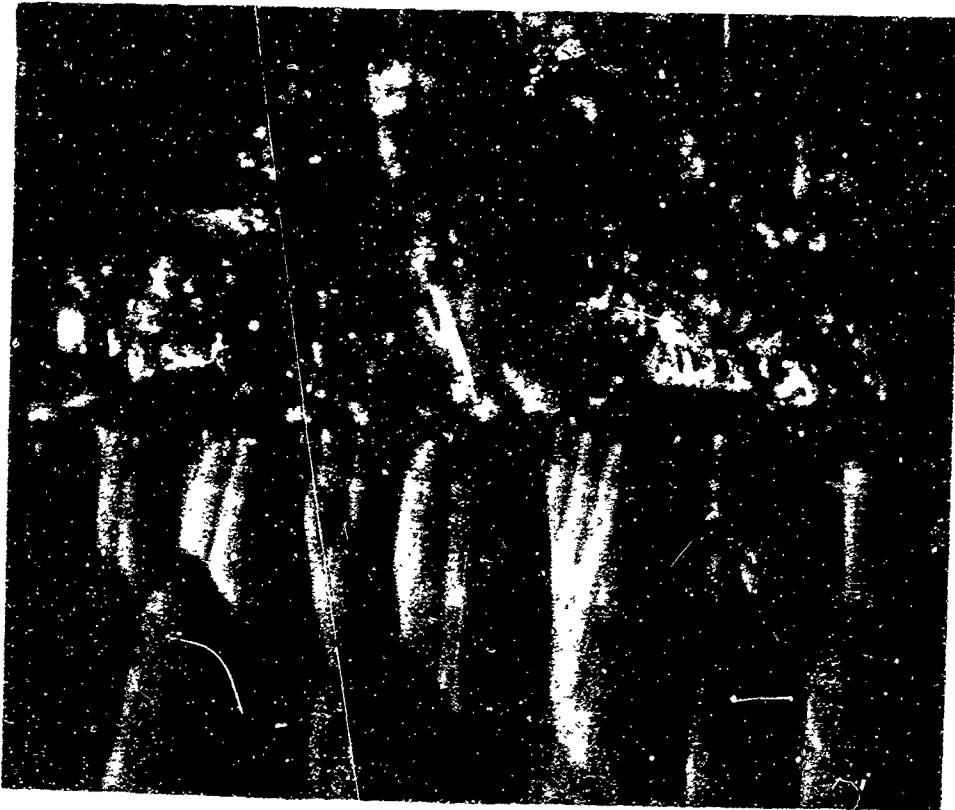


Figure 14. Structure of a Medium Density Pyrolytic Carbon, 500X  
Deposition Temperature: 2000°C, Density: 1.768 g/cc



Figure 15. Structure of a High Density Pyrolytic Carbon, 500X  
Deposition Temperature: 2200°C, Density: 2.24 g/cc

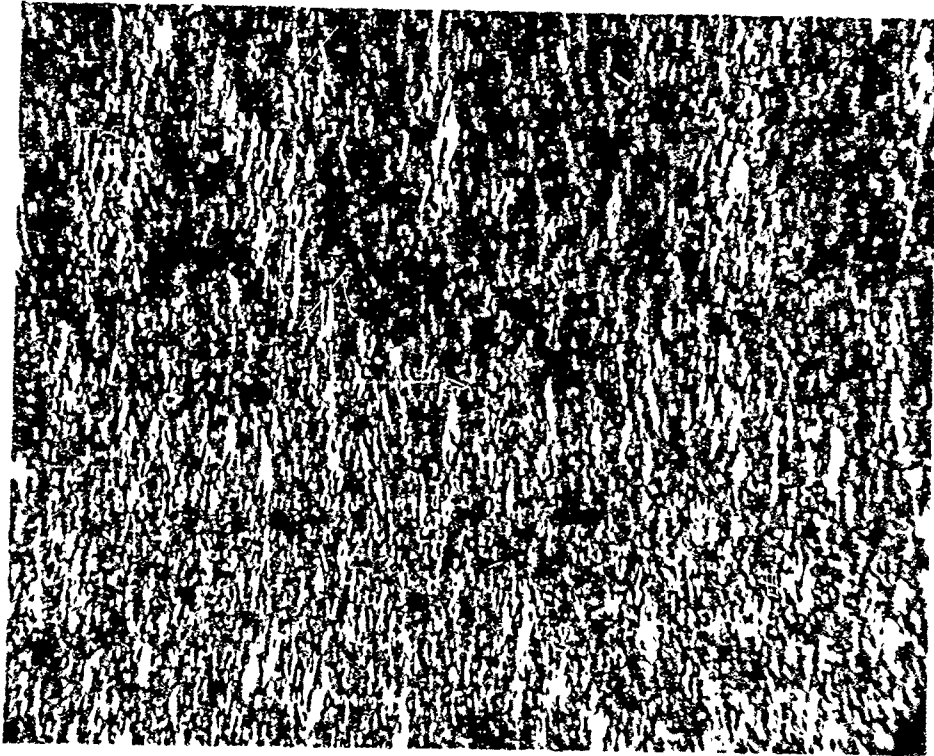


Figure 16. Pyrolytic Carbon Deposited on a Lapped Graphite Surface, 500X

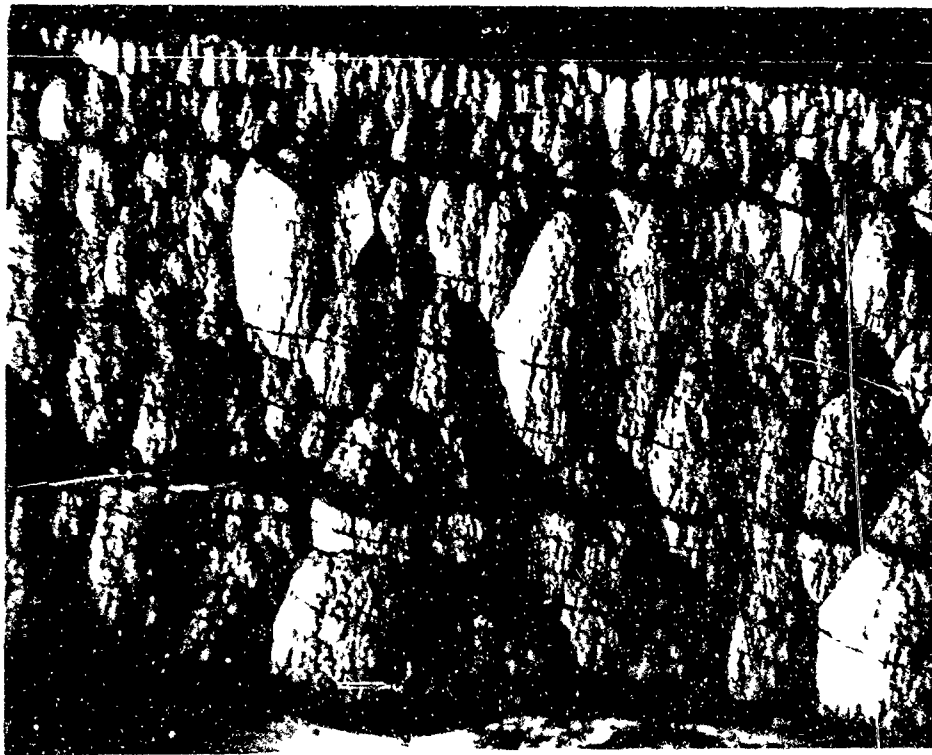


Figure 17 Pyrolytic Carbon Deposited on an Unlapped Graphite Surface, 500X

With the foregoing points in mind, the apparatus as depicted in Figures 18 and 19 was constructed. The substrate, a flat disc, has a

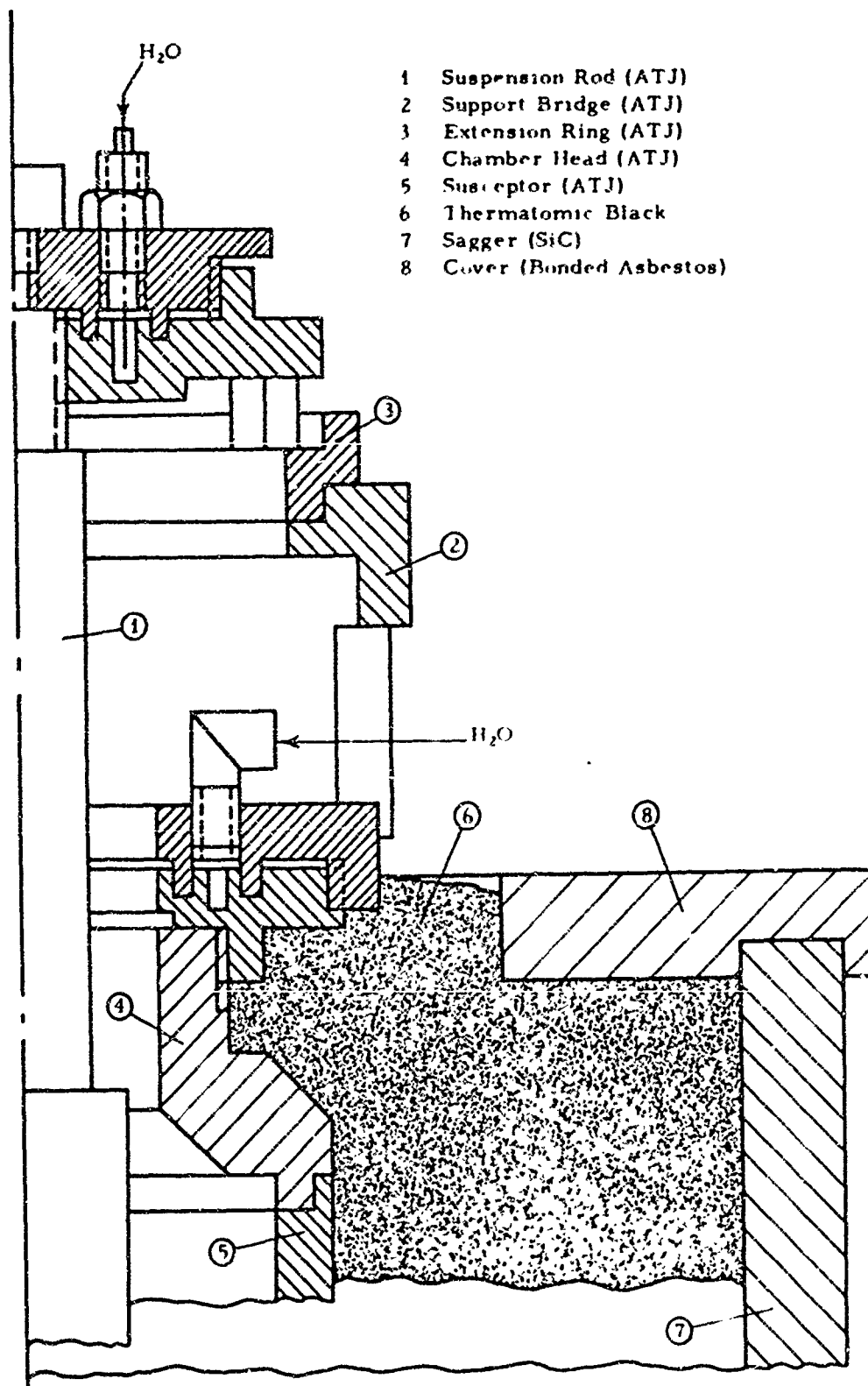


Figure 18. Sectional Drawing of an Apparatus for the Deposition of Pyrolytic Carbon - Upper Section

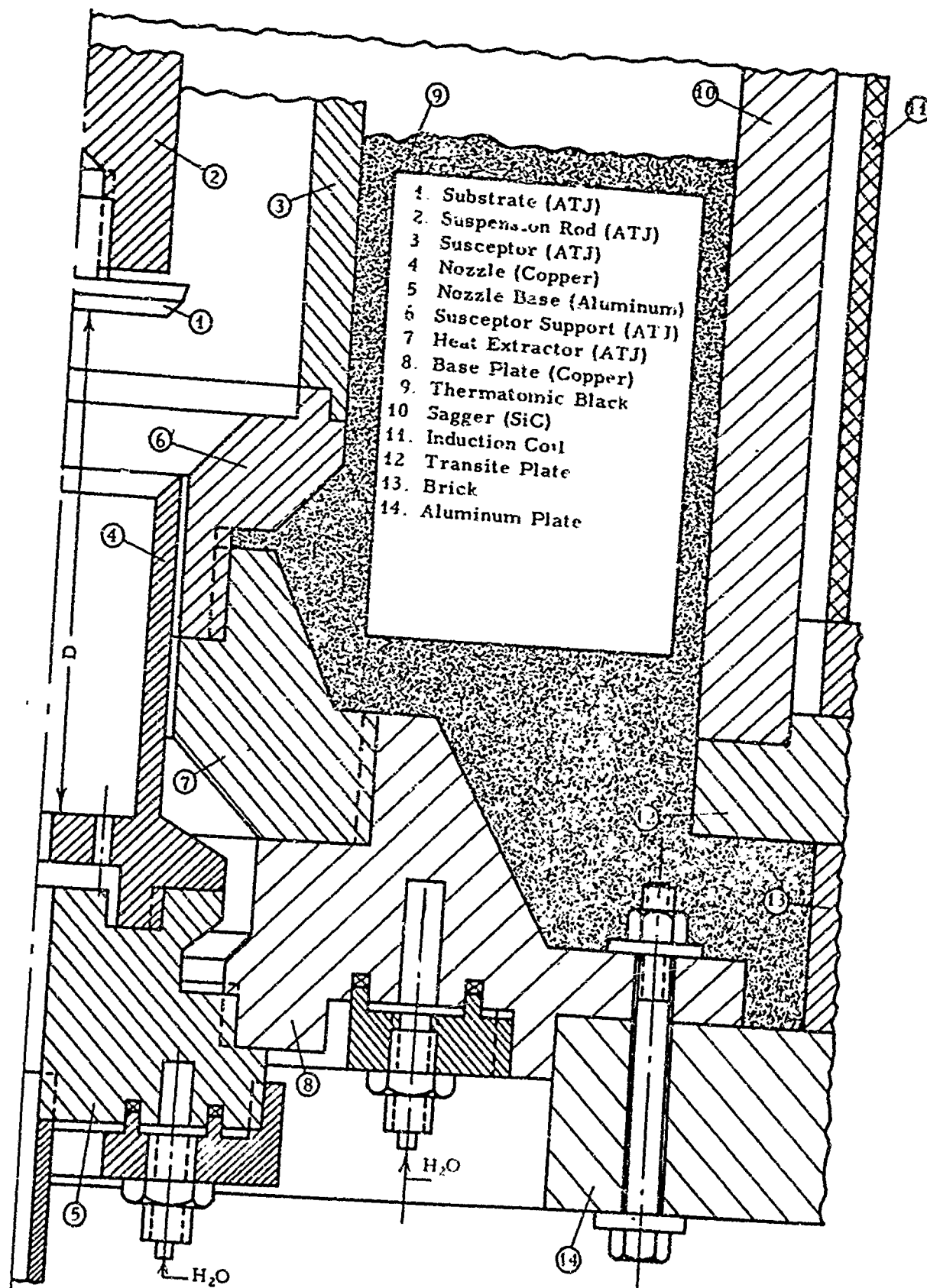


Figure 19. Apparatus for the Deposition of Pyrolytic Carbon - Lower Section

small threaded shaft which is screwed into a graphite suspension rod. The upper part of the suspension rod is water cooled and rests on a graphite support on top of the furnace. Extension rings between the support bridge and the suspension rod assembly allow adjustment of the distance between the inlet nozzle and the substrate. The substrate is heated by radiation from a susceptor which is heated by induction using a 10,000 cycle, 100 KW, motor generator unit. The whole rod assembly can be withdrawn from the furnace for substrate removal and lowered back into the furnace with a new substrate without a power shutdown. The exhaust gas, passing through the water cooled exhaust port, prevents oxidation of the rod and substrate during removal. The temperature of the substrate is read directly through the copper insert nozzle until the carbonaceous gas is introduced. After introduction of the carbon-bearing gas (methane), the temperature can no longer be read directly on the surface of the substrate because of the formation of soot clouds. The temperature, therefore, is controlled by maintaining the temperature of the susceptor at a constant level. In this apparatus as in the resistance heated one, discussed previously, these soot clouds can cause an error in temperature readings up to 80°C.

Visual examination of the pyrolytic carbon surface became the main criterion for process evaluation since the elimination of cones was the primary goal. Figure 20 illustrates the difference between a good and a bad surface. The surface of the piece at the left is free of blemishes but surface blemishes are quite evident in the piece on the right and photomicrographs of the material established the presence of a cone under each of the blemishes.

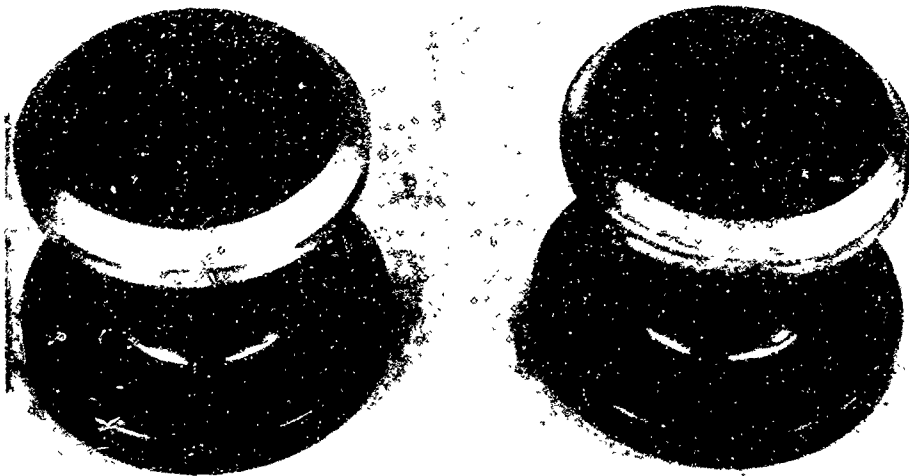


Figure 20. Comparison of Good and Poor Pyrolytic Carbon Deposition

In order to determine the cause of conical growths, which seemed to appear in a pattern, the distance between the substrate and the inlet nozzle was varied with all other conditions being held constant. The results of these experiments along with the processing conditions are shown in Figure 21. As the distance between the nozzle and the

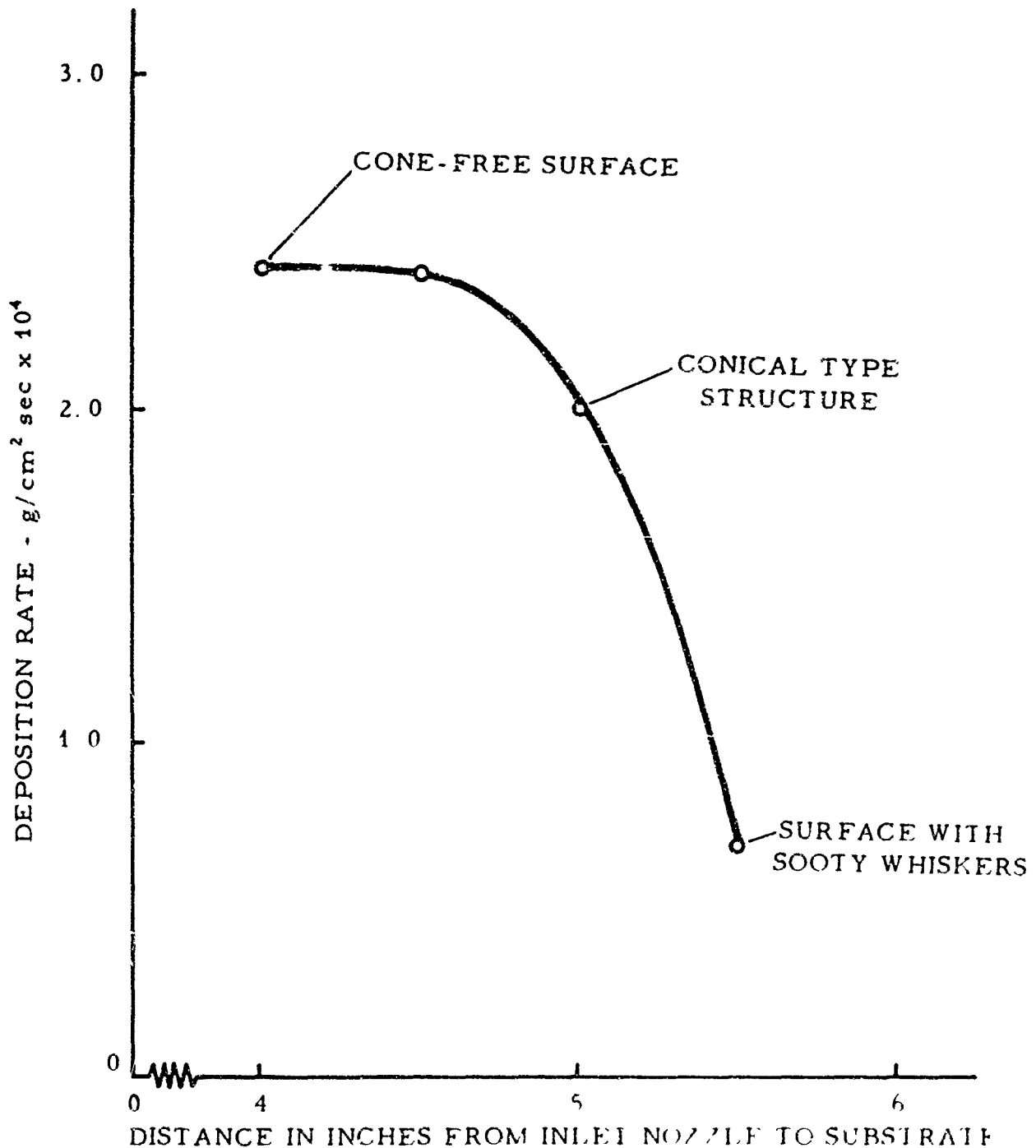


Figure 21. Appearance of Conical Surface Growths as a Function of Distance Between Gas Inlet and Substrate

substrate increased, the deposition rate decreased and the cone growth appeared until, at a large distance from the nozzle, long sooty whiskers were formed. This finding suggested the following explanation. As the carbonaceous gas enters the deposition chamber its temperature increases rapidly, and as soon as it becomes superheated, with respect to the temperature of thermodynamic equilibrium (see Appendix II), some carbon nuclei appear in fine dispersion. As these nuclei travel toward increasingly higher temperatures, they begin to grow due to collisions with carbonaceous gas molecules. Consequently, the concentration of the carbonaceous gas molecules decreases in this direction. Substrates placed at various points in the gas path, therefore, encounter substantially different conditions. When the substrate is located in the range of primary nucleation, pyrolytic carbon with a fine cone structure (see Figure 22) is deposited. When located further downstream, where most nuclei have grown to a considerable size, the deposition rate is

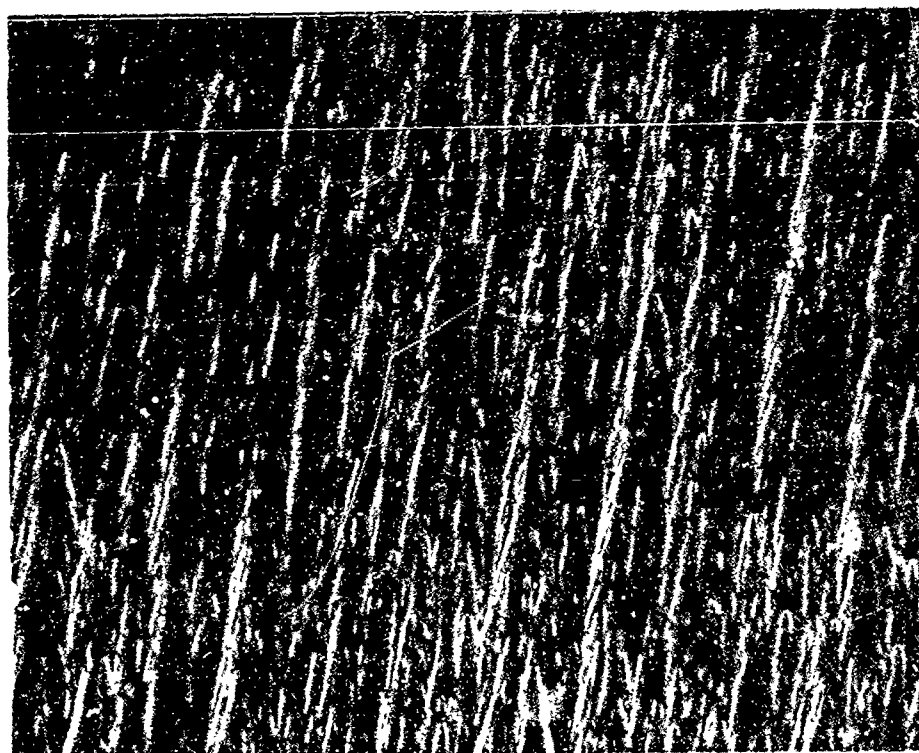


Figure 22. High Density Pyrolytic Carbon with Needle Structure

lower due to the lower concentration of carbonaceous gas, and any settling of the growth nuclei (soot particles) on the surface causes flagrant cone growth.

The fact that soot particles (or other projections in the substrate surface) are responsible for cone formation is illustrated in Figure 23. This cone formation caused by soot particles applies only to random soot particles adhering to the surface and thereby creating a projection. When a completely smooth layer of soot was applied to the substrate prior to coating and the sample was coated with the substrate placed the proper distance from the inlet nozzle, no more cones appeared than when there was no soot layer present. The soot layer, however, did cause poorer adhesion of the coating to the substrate which made separation of the two quite easy.



Figure 23. Illustration of a Soot Particle Originating a Large Cone in an Otherwise Needle Structure Pyrolytic Carbon

In normal deposition (substrate not intentionally covered with soot) the number of soot particles which manage to settle on the substrate surface depends strongly on the identity and concentration of the carbonaceous gas used. If a molecule of methane hits the surface of the substrate, two molecules of hydrogen are released which form a stream away from the surface thus protecting the surface from most of the approaching soot particles. This phenomenon can actually be observed. Looking down along the suspension rod during a very slow (non-turbulent) pyrolytic process, two dark layers can be seen; one around the rod and the other covering the wall of the chamber. Between the two layers is a bright ring. The bright ring can be easily distinguished as a cloud of finely dispersed soot, while the darker areas are due to the lower temperature of the chamber bottom which can be seen through the soot-free zones but not through the soot cloud. If substrates are located far from the inlet nozzle, conditions for pyrolytic deposition are highly unfavorable in two respects; (a) the soot particles have grown to large dimensions and (b) the concentration of the carbonaceous gas molecules is so low that practically no protective hydrogen barrier is formed.

The velocity of impingement of the carbonaceous gas on the substrate is an additional factor influencing the growth of cones. It was found that cone formation first decreased and then increased with increasing overall velocity. This can be interpreted as follows: a moderate increase in velocity shortens the time for nuclei to grow, thus decreasing the size of the soot particles arriving at the substrate surface, whereas too high a velocity destroys the protective hydrogen barrier.

In summary, the following conclusions for preventing cone growths are formulated:

- 1) The path of the carbonaceous gas mixture should be shortened as much as possible and should be equal for all parts of the body to be coated.
- 2) Although moderately high gas velocities are desirable to prevent growth of nuclei, excessively high velocities are detrimental because they cause a breakdown of the hydrogen barrier.
- 3) High concentrations of the carbon bearing gas are detrimental since they enhance the fast growth of nuclei.
- 4) If a gas is added which reacts with the carbon nuclei to form a stable gaseous compound, and if the quantity of this gas can be controlled in such a manner that this gas

is completely reacted before reaching the substrate, the formation of nuclei and their growth can be controlled. Such is believed to describe the manner in which the chlorine addition, mentioned earlier in the report, affected the deposition efficiency and density of the product

Throughout the experimental series it was noted that much less soot formation occurred when hydrogen was used as the diluent. Although it did not act in the same manner as chlorine and fluorine in forming stable high temperature compounds, the effect was somewhat the same. Besides depressing the equilibrium of the reaction, hydrogen forced recombination of the carbon molecules into compounds with higher cracking temperatures and thereby reduced the sooting and effectively allowed more of the pyrolyzing gases to strike the substrate surface.

In the foregoing conclusions, items 1, 2 and 3 are interrelated. For instance, if the gas path is very short a low velocity in high concentration can be tolerated. However, if the gas path is long, the concentration must be kept low and the velocity as high as possible without destroying the hydrogen barrier.

#### 2.7. Effect of Annealing on Density and Structure of Pyrolytic Carbon

Pyrolytic carbon samples covering a range of densities were heated to 2800°C to determine the effect of annealing upon the density and structure of the material. Five samples of pyrolytic carbon having densities from 1.36 to 2.22 g/cc were cut in half and the mating faces notched for identification. Photomicrographs were taken of the notched edges of one set of these halves. The matching pieces of these samples were annealed for half an hour. Photomicrographs were taken of the notched edges of the five annealed sections. These "as deposited" and "as annealed" photomicrographs are shown in Figures 24 through 28. Four other samples were annealed to 2800°C (with no hold time) and the physical changes which took place in all nine samples are tabulated in Table 1.

From the data in Table 1, it is evident that pyrolytic carbon in the mid-density range (circa 1.8 g/cc) does not change much in the annealing process. Material which exhibits a low density, however, is profoundly affected by annealing as evidenced in Figures 26 and 27 where the grain pattern or orientation is grossly distorted. The high density material, which already had a fine-grained structure, loses all traces of conical growth patterns upon annealing as shown in Figure 28.



As Deposited, Density 2.008 g/cc



After Annealing, Density 2.049 g/cc

Figure 24. Structural and Density Changes in Pyrolytic Carbon as a Result of Annealing, 500X

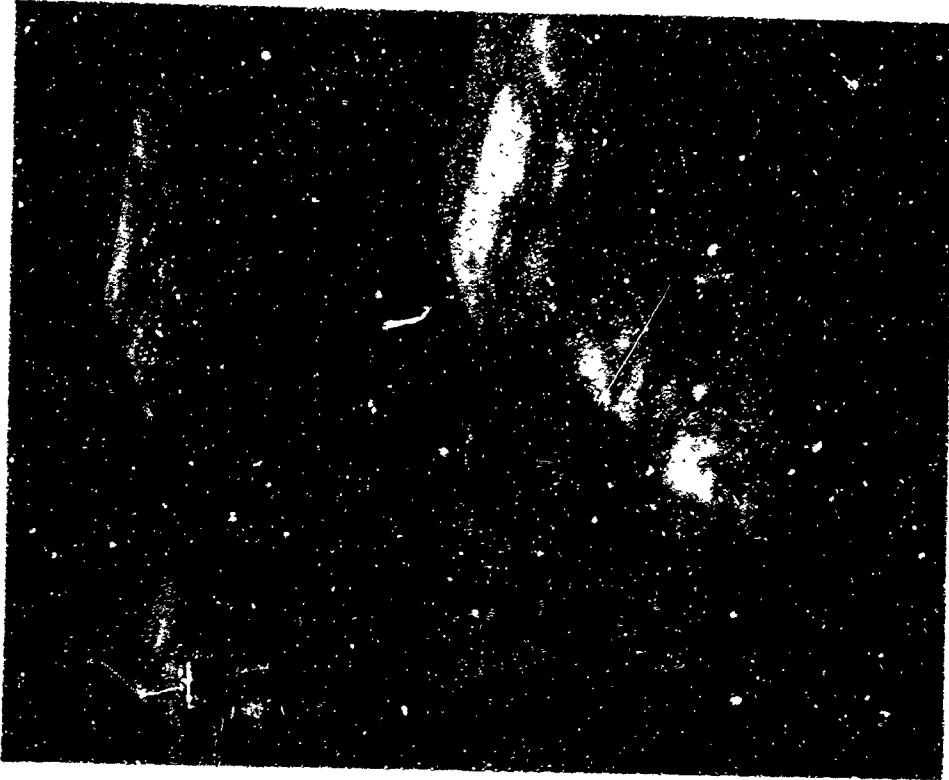


As Deposited, Density 1.78 g/cc

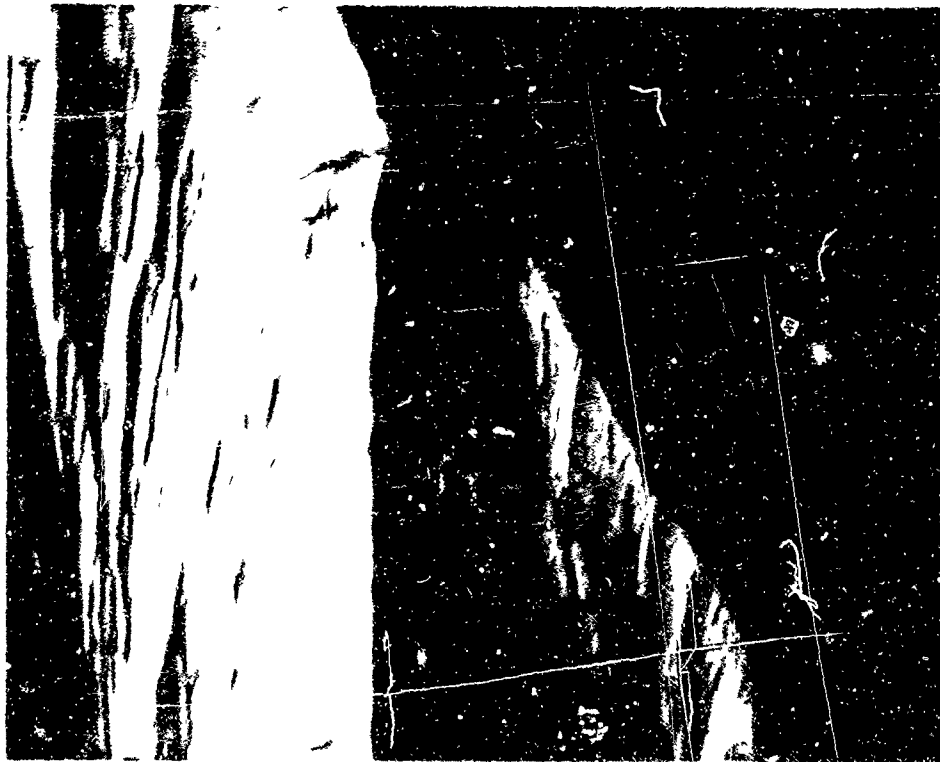


After Annealing, Density 1.86 g/cc

Figure 25. Structural and Density Changes in Pyrolytic Carbon as a Result of Annealing, 500X

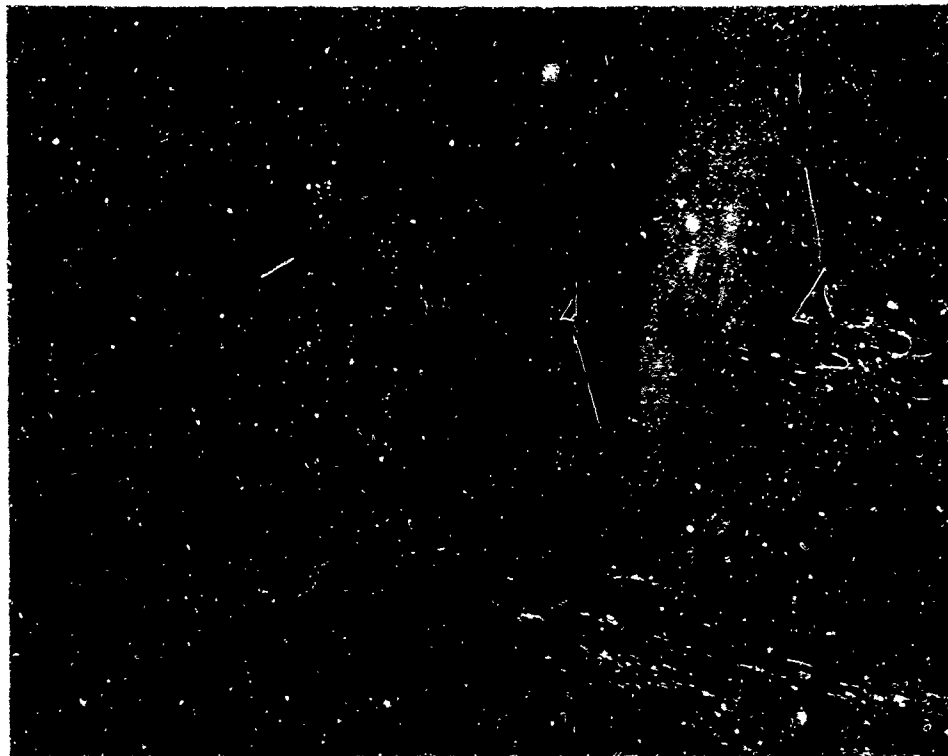


As Deposited, Density 1.55 g/cc



After Annealing, Density 2.208 g/cc

Figure 26. Structural and Density Changes in Pyrolytic Carbon as a Result of Annealing, 500X



As Deposited, Density 1.38 g/cc



After Annealing, Density 2.179 g/cc

Figure 27. Structure and Density Changes in Pyrolytic Carbon as a Result of Annealing, 500X



As Deposited, Density 2.215 g/cc



After Annealing, Density 2.225 g/cc

Figure 28. Structural and Density Changes in Pyrolytic Carbon as a Result of Annealing, 500X

Table 1. Physical Changes in Pyrolytic Carbon upon Annealing to 2800°C

Condition at 2800°C 1/2 hour hold	Density g/cc	Dimensions <sup>a</sup> , inches				Wgt Loss Per Cent	Vol Loss Per Cent	C-Direction Shrinkage Per Cent	Spec. Pres micro-atm-cm
		$\Delta l$	l	W	$\Delta W$				
As deposited	2.215	0.2875	0.2240	0.0301	0.04	1.7	4.3	--	
As annealed	2.225	0.2968	0.2309	0.0288					
	+ .010	+ .0093	+ .0069	- .0013					
As deposited	2.008	0.2349	0.2085	0.0530	0.11	2.0	4.2	--	
As annealed	2.047	0.2371	0.2108	0.0515					
	+ .041	+ .0022	+ .0023	- .0012					
As deposited	1.783	0.3479	0.2031	0.0278	0.25	4.56	3.6	--	
As annealed	1.859	0.3511	0.2058	0.0268					
	+ .076	+ .0032	+ .0027	- .0010					
As deposited	1.557	0.2512	0.2259	0.0272	0.26	29.8	14.7	--	
As annealed	2.208	0.2491	0.2230	0.0232					
	+ .651	- .0021	- .0029	- .0040					
As deposited	1.380	0.2551	0.2260	0.0842	0.14	36.8	21.6	--	
As annealed	2.179	0.2393	0.2111	0.0659					
	+ .799	- .0158	- .0149	- .0183					
Condition at 2800°C									
No hold									
As deposited	2.220	1.0430	0.2034	0.0300	0.18	1.5	1.0	430	
As annealed	2.225	1.0535	0.2056	0.0297				55	
	+ .003	+ .0105	+ .0022	- .0003					
As deposited	2.196	0.7083	0.2145	0.0313	0.30	2.0	2.9	687	
As annealed	2.211	0.7193	0.2185	0.0304				210	
	+ .015	+ .0110	+ .0041	- .0009					
As deposited	2.145	1.3829	0.1930	0.0312	0.12	1.5	1.6	719	
As annealed	2.178	1.3968	0.1951	0.0307				550	
	+ .033	+ .0139	+ .0021	- .0005					
As deposited	1.253	0.8608	0.2030	0.0761	0.19	15.4	11.8	2450	
As annealed	1.479	0.8670	0.2043	0.0674				2460	
	+ .226	- .0062	+ .0013	- .0090					

<sup>a</sup>W - in A-B plane  
e - parallel to C axis

One obvious and well known effect of annealing, illustrated in Figures 24 and 25, is the convex delamination that occurs in pyrolytic carbon having large cones in the structure. This demonstrates that the deposition within the cone is not planar and the laminations are due to the curvature of the surface.

The density plotted as a function of deposition temperature for the "as deposited" and annealed samples is illustrated in Figure 29. The volume and C-Direction shrinkage resulting from annealing are plotted as a function of the "as deposited" density (Figure 30).

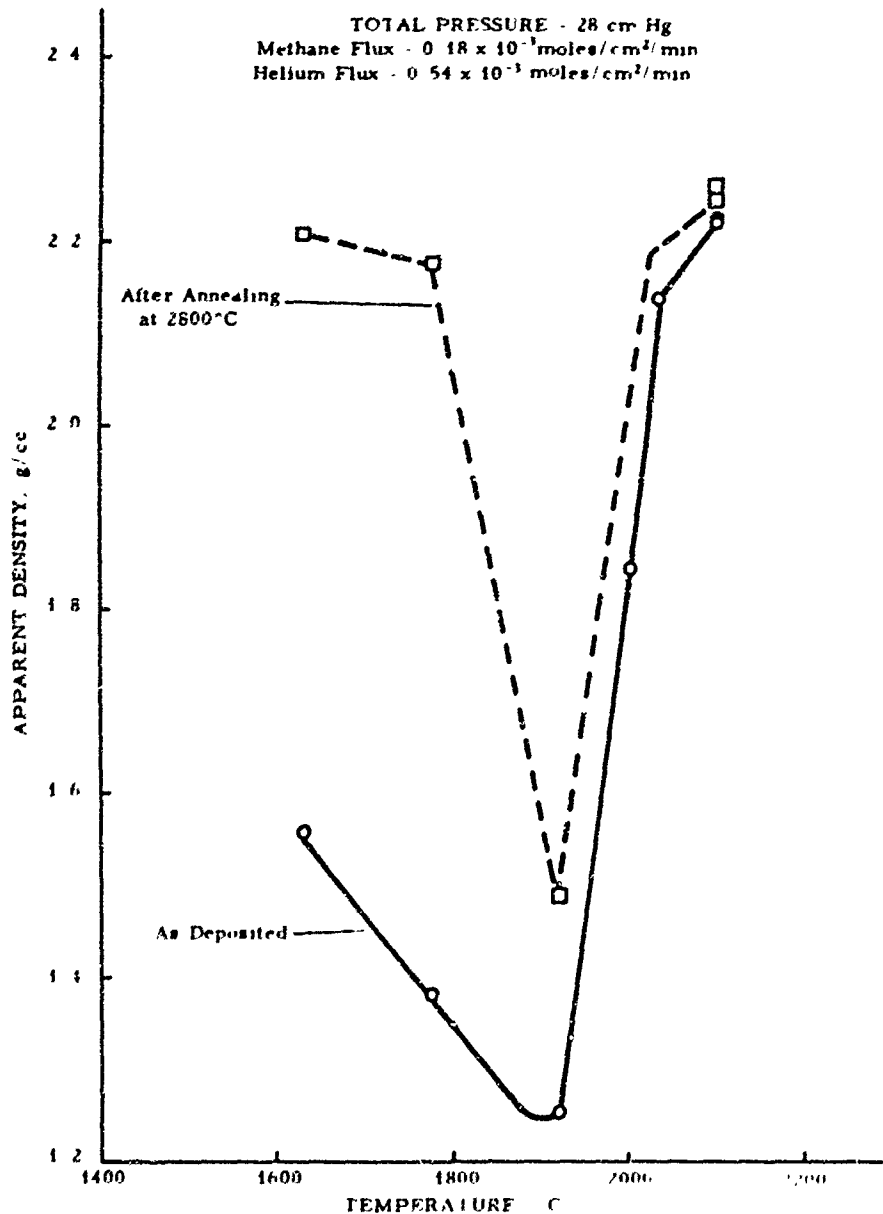


Figure 29. Density Changes in Pyrolytic Carbon as a Result of Annealing versus Deposition Temperature

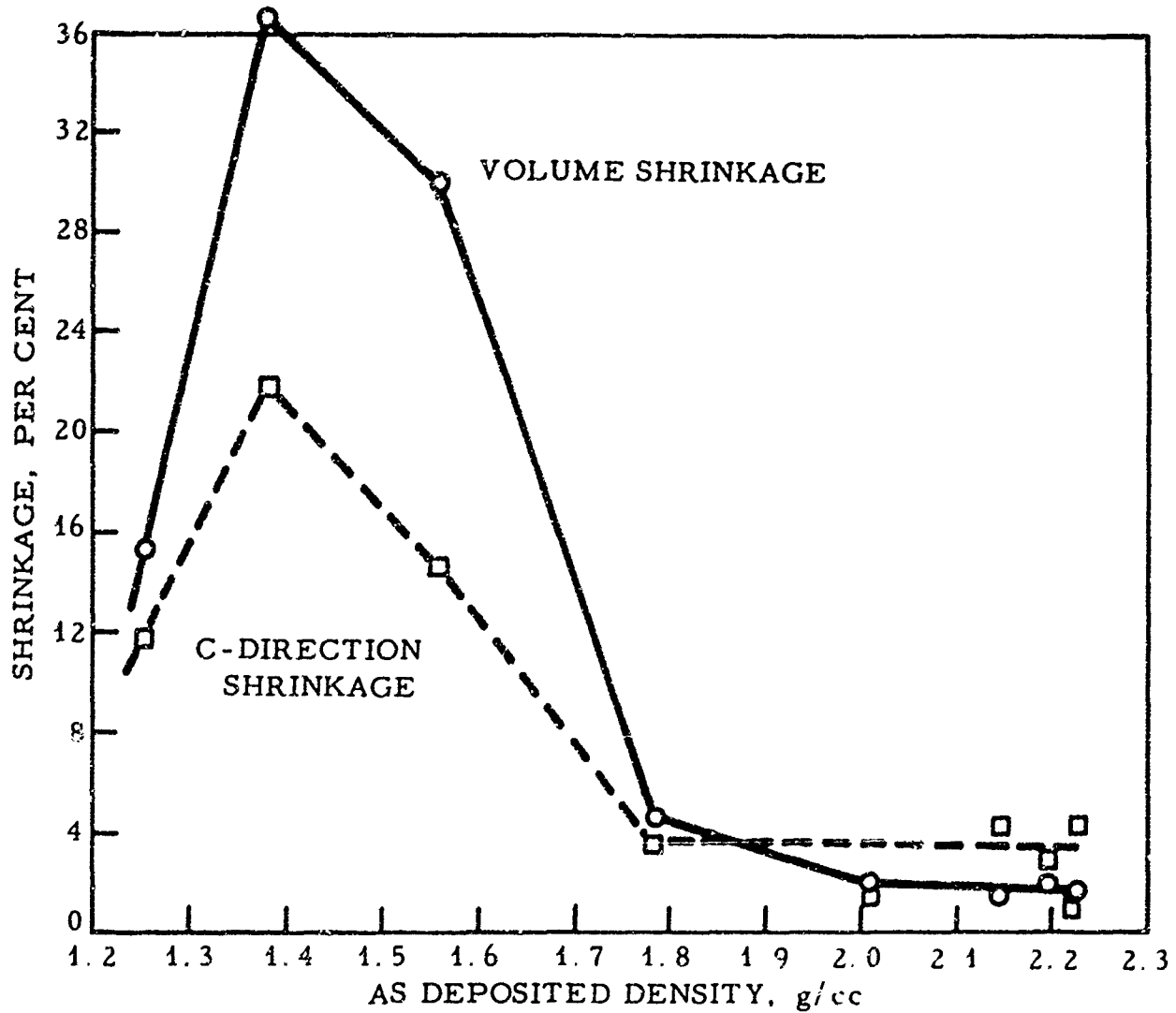


Figure 30. Volumetric and C-Direction Shrinkage of Pyrolytic Carbon as a Result of Annealing

## 2.8. Physical Properties of Pyrolytic Carbon

### 2.8.1. Specific Resistance

The specific resistance of pyrolytic carbon was measured by the four point probe method and is plotted as a function of density in Figure 31. Examination of this curve allows a general conclusion that, for unannealed samples, the specific resistance varies inversely with the density.

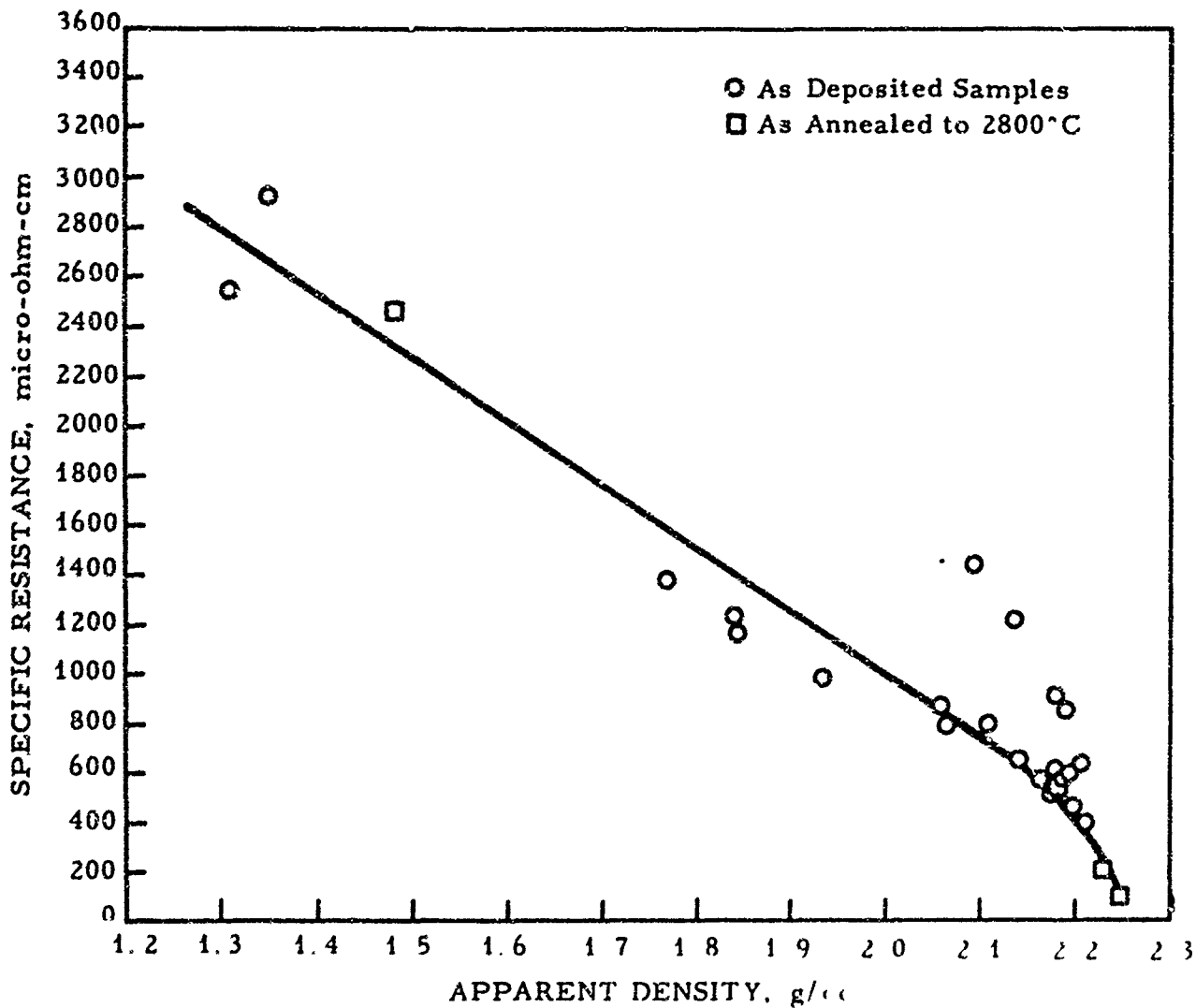


Figure 31. Specific Resistance of "As Deposited" and "As Annealed" Pyrolytic Carbon versus Density

### 2.8.2. Modulus of Rupture

In order to establish a value for the rupture strength of pyrolytic carbon, several samples were fractured in flexure on 5/16-inch rolls using a 3/16-inch span. The load was applied parallel to the "C"-direction and perpendicular to the "A-B" plane of the pyrolytic

carbon. The rupture strength was then calculated by use of the expression for the maximum fiber stress, which is:

$$S = \frac{PL}{bh^2} \quad (1)$$

where

P = load in pounds

L = distance between supports in inches

b = width of specimen in inches

h = thickness of specimen in inches

Table 2 lists the strength values obtained from the above tests. In view of the span to thickness ratio (approximately 3.5), these values of flexure strength are probably quite accurate and, in any case, would represent the minimum strengths.

Table 2. Rupture Strengths of Pyrolytic Carbon

Sample No.	Apparent Density g/cc	Breadth(b) inches	Thickness(h) inches	Load(p) lbs	Rupture Strength lbs/in <sup>2</sup>
16A	2.194	0.202	0.045	10.7	12,150
13B	2.188	0.214	0.037	10.0	16,000
15C	2.163	0.194	0.034	5.0	10,950
17B	2.054	0.207	0.051	16.2	14,100
17C	2.036	0.201	0.052	19.0	16,400
19C	1.928	0.240	0.046	10.6	9,770
21B	1.859	0.207	0.040	11.4	16,150
23D	1.787	0.196	0.065	25.7	14,450
19B	1.739	0.240	0.046	17.3	15,590
18A	1.714	0.225	0.035	10.0	17,000
25A	1.408	0.208	0.137	98.4	11,800
24C	1.380	0.202	0.080	26.6	9,700
24B	1.290	0.201	0.046	8.2	9,050

### 2.8.3. Coefficient of Thermal Expansion

The coefficient of thermal expansion (CTE) of pyrolytic carbon

in the "C"-direction was determined by the Newton's Rings method in the temperature range of 86 to 747°C and the values are listed in Table 3.

Table 3. Thermal Expansion of Pyrolytic Carbon

Temperature °C	CTE
	Mean from 27°C to Indicated Temperature $10^{-7} / ^\circ\text{C}$
86	65.87
150	122.08
204	127.19
266	126.15
310	132.72
383	147.32
426	150.18
486	162.64
545	172.24
627	173.52
674	172.39
726	180.21
747	195.15

#### 2.8.4. High Temperature Creep and Elastic Constant Determination

Specimens of pyrolytic carbon cut from a single piece were tested for flexural creep under 3-point loading at temperatures between 2200 and 3000°C, and the elastic constants were determined. All specimens were 1/8 by 1/16 by 1-1/4 inches and the span used was one inch; the single knife edge made contact with the broad face of the specimen. For comparison, creep tests were made on specimens of pyrolytic carbon with two crystalline orientations and also on specimens of ATJ graphite cut to the same dimensions and tested in a similar manner.

Figure 32 shows the creep curves for unannealed pyrolytic carbon between 2200 and 3000°C. All specimens were oriented in the "A" direction as described in the next paragraph. In these tests, the load was applied as soon as the desired test temperature was stabilized. Figure 33 illustrates the creep that occurred when the samples were annealed at 3000°C for two hours before applying the load. As can be seen, by comparing Figures 32 and 33, there is much less creep in the annealed samples. In Figure 32, it can be seen also that the specimen at 3000°C showed much less creep than the specimen at 2800°C, in-

SPECIMEN PROPERTIES

Density 2.24 g/cm<sup>3</sup>

As Deposited

TEST CONDITIONS

"A" Orientation

Load = 1000 gms

1/8 by 1/16 inch Cross Section

1 inch Between Supports

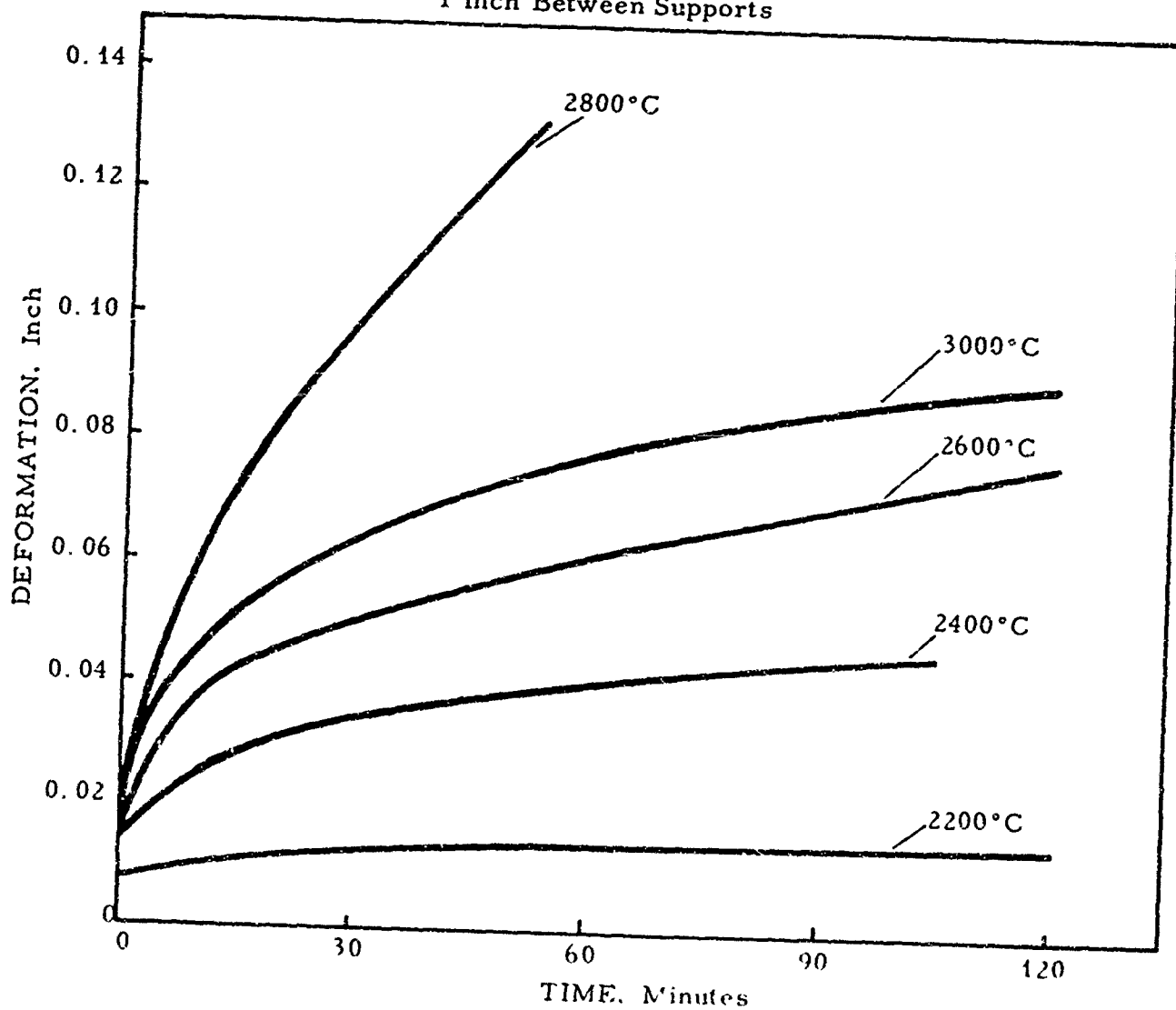


Figure 32. Creep of "As Deposited" Pyrolytic Carbon versus Time and Temperature

SPECIMEN PROPERTIES

Density 2.24 g/cm<sup>3</sup>  
Annealed 2 hours at 3000°C

TEST CONDITIONS

"A" Orientation  
Load = 1000 grams  
1/8 by 1/16 inch Cross Section  
1 inch Between Supports

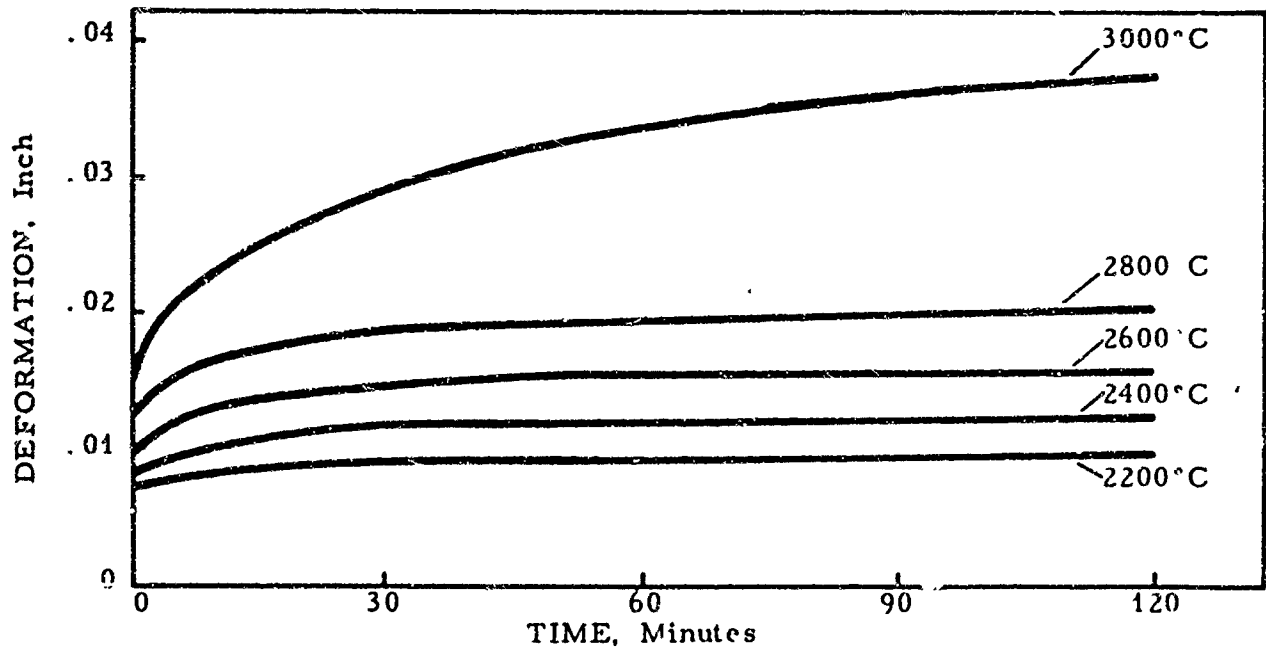


Figure 33. Creep of Annealed Pyrolytic Carbon versus Time and Temperature

dicating that a significant change takes place between 2800 and 3000°C, probably a rotation of layer planes to give a three dimensional ordering. Indications that the ordering process, which takes place during graphitization, is also a function of time are shown by a comparison of the curves at 3000°C in Figures 32 and 33. There is also an indication that the creep decreases with an increase in the time the graphite is held at its highest heat treatment temperature before being tested for creep. For all specimens in the above curves, the applied load was 1000 grams, which corresponds to a maximum fiber stress of 6770 lbs/in<sup>2</sup>.

In order to determine the effect of crystalline orientation on the creep of pyrolytic carbon, two specimens were prepared with "A" orientation, the same as used in the previous tests where the basal planes of the crystallites were parallel to the broad face of the specimens, and two specimens were prepared with "B" orientation where the crystallographic planes were perpendicular to the broad face of the specimen. The specimens were annealed for two hours at 3000°C before the creep tests began. The load used was 1500 grams, which gives a maximum fiber stress of 10,150 lbs/in<sup>2</sup>. Figure 34 shows the creep curves which were

SPECIMEN AND TEST CONDITIONS  
 Single Specimen of Pyrolytic Graphite  
 Annealed 2 Hours at 3000°C  
 Tested Successively from 2200 to 3000°C  
 Load - 1500 grams  
 1/8 by 1/16 inch Cross Section  
 1 inch Between Supports

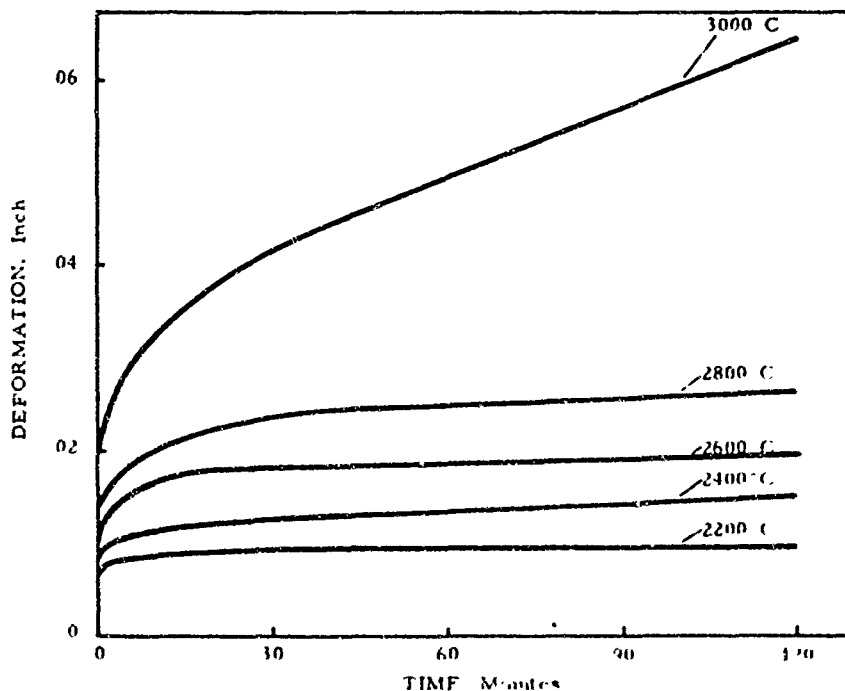


Figure 34. Creep of Pyrolytic Carbon versus Time and Temperature, "A" Orientation

obtained with one of the specimens with "A" orientation, where the tests were all made on the same specimen, starting at 2200°C and proceeding to 3000°C in steps of 200°C. The specimen was allowed to relax at the test temperature with no load for 20 minutes at the end of each test and it was then cooled to room temperature before the next test. Figure 35 shows the results for a specimen with "B" orientation under the same test conditions. A comparison of the two curves shows that there is no significant difference between the creep curves at any temperatures. This is rather surprising, because normally in the case of highly anisotropic materials, such as ZT graphite, specimens with "B" orientation show less creep than specimens with "A" orientation.

SPECIMEN AND TEST CONDITIONS

Single Specimen of Pyrolytic Graphite  
 Annealed 2 Hours at 3000°C  
 Tested Successively from 2200° to 3000°C  
 Load = 1500 grams  
 1/8 by 1/16 inch Cross Section  
 1 inch Between Supports

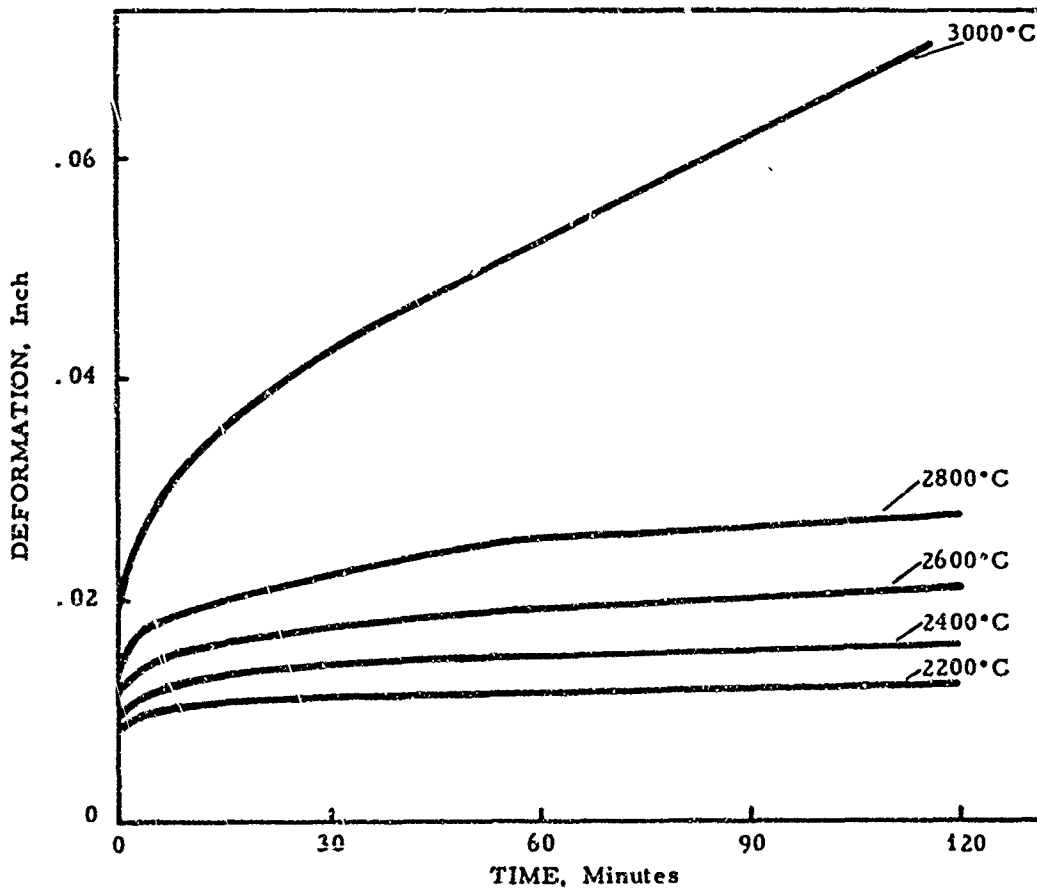


Figure 35. Creep of Pyrolytic Carbon versus Time and Temperature, "B" Orientation

In order to compare the creep curves for pyrolytic carbon and pyrolytic graphites with those of a standard graphite, specimens of ATJ graphite were prepared with the same dimensions as the pyrolytic specimens. Figure 36 shows the creep curves for ATJ samples loaded with a force of 750 grams, corresponding to a maximum fiber stress of 5075 lbs/in<sup>2</sup>. This stress is half of the maximum stress that is used on the pyrolytic specimens, but it is greater than the room temperature breaking strength of ATJ graphite. It can be seen that there is considerably less creep in pyrolytic graphite than in ATJ graphite, with the differences in the curves for the materials becoming more and more pronounced as the temperature increases.

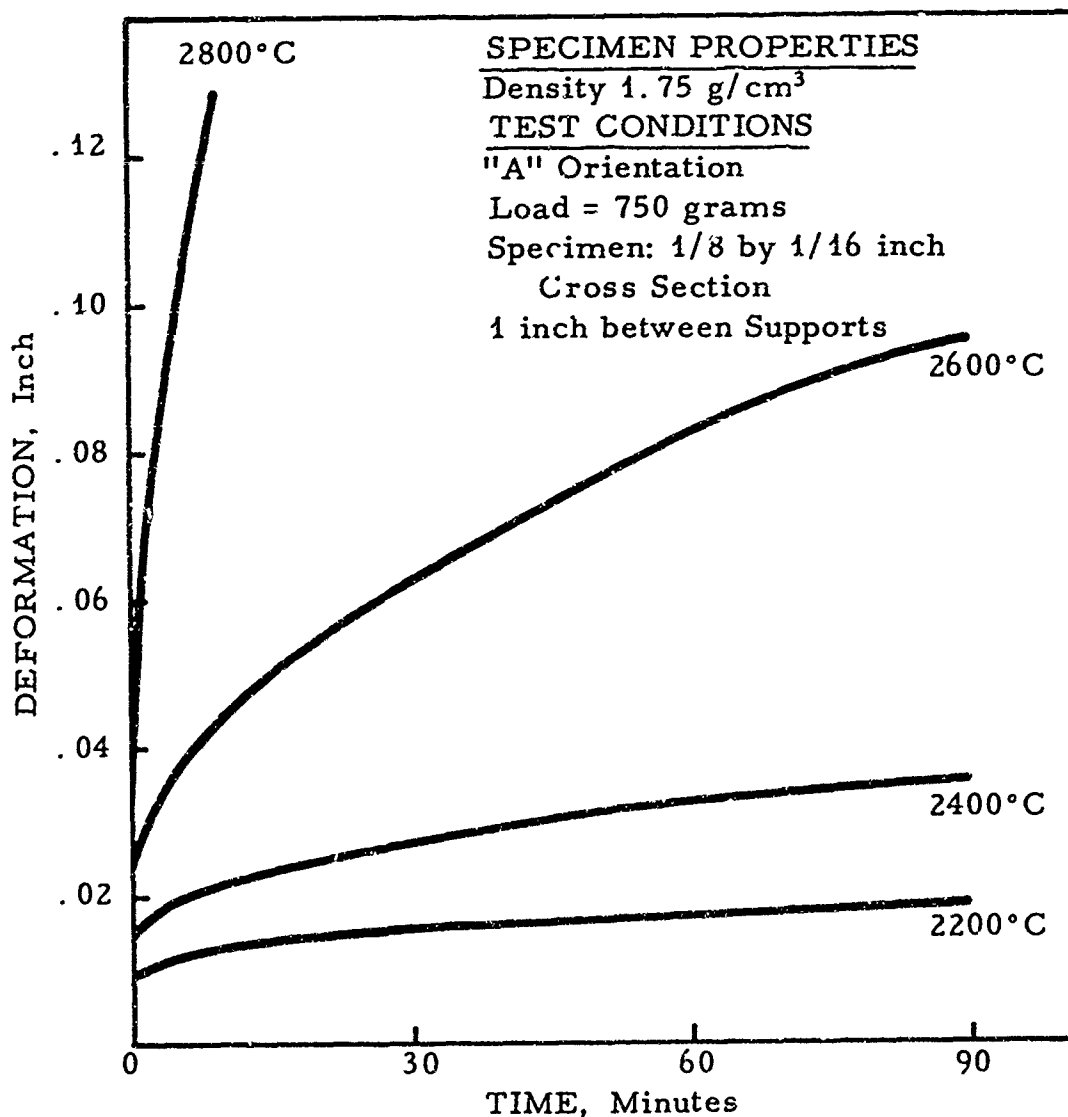


Figure 36. Creep of ATJ Graphite

The elastic constants for pyrolytic graphite were determined by using the instantaneous elastic deformation of the annealed pyrolytic specimens and the standard equation for the Young's modulus  $K$  of a beam in flexure. Table 4 shows the average values of the elastic constant  $K$  for each temperature at which creep was tested. The values were found to be independent of grain orientation, and they represent the average for two samples with "A" orientation and two samples with "B" orientation. The elastic constant decreased as the temperature was increased, but did not decrease linearly with the temperature as in the case of ATJ graphite.

Table 4. The Elastic Constant  $K$  for Pyrolytic Graphite

Temperature °C	Elastic Constant $K$ lbs/in <sup>2</sup>
2200	$3.48 \times 10^8$
2400	3.30
2600	2.74
2800	2.28
3000	1.68

### 3. PYROLYTIC CARBON COATINGS ON GRAPHITE YARN

Graphite cloth has found extensive use in many fields of application as an insulating material and electrical conductor. One limit to its usefulness, however, has been the relatively low strength of the material. The strength of the cloth can be increased by coating it with pyrolytic carbon but this method presents several disadvantages. If graphite cloth is coated with pyrolytic carbon, its increase in strength is accompanied by an increase in thermal conductivity and brittleness which limits its usefulness somewhat. With this thought in mind, it was decided to investigate the coating of individual strands of the cloth prior to weaving to see if the strength of these strands could be increased while retaining the desirable characteristics of weight, flexibility and electrical conductivity.

A furnace, shown schematically in Figure 37, was constructed

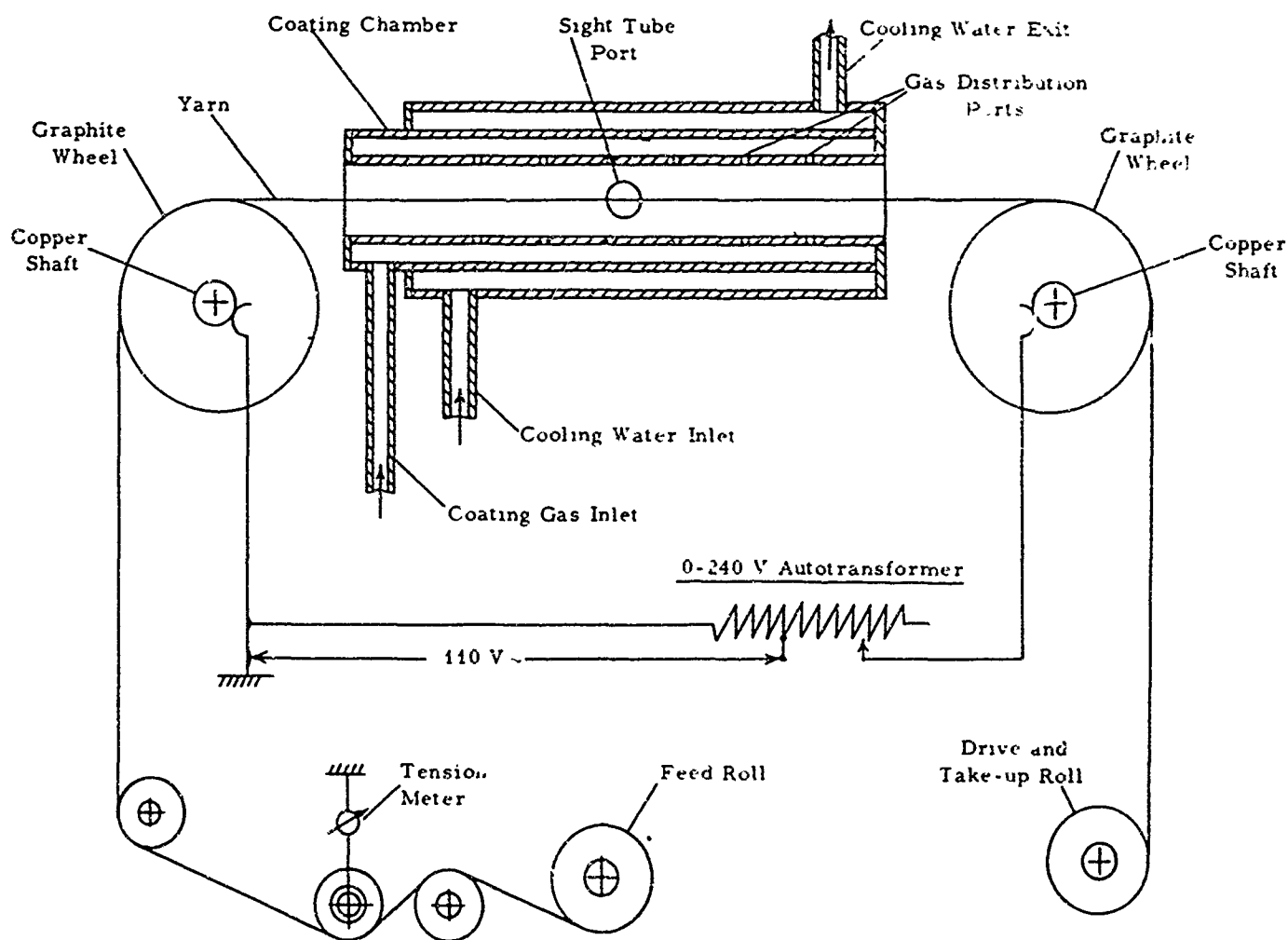


Figure 37. Schematic Drawing of Apparatus for Coating Graphite Yarn with Pyrolytic Carbon

for the pyrolytic coating of yarn on a continuous basis. The principle of this equipment is quite simple and is best described as follows: graphite yarn is fed from a standard package spool through a series of tension rollers, across two graphite wheels, passing through the coating chamber in the process, and wound again on a standard package spool. As the yarn is fed through the water-cooled coating chamber, an electric current is passed through that portion of the yarn which connects the two graphite wheels at the ends of the coating chamber. Thus, as the yarn passes through the coating chamber, it is heated to the desired temperature by controlling the power input. A mixture of argon and methane gas is fed into the chamber where it cracks on the hot surface of the yarn and deposits a coating of pyrolytic carbon. The coating chamber and graphite wheels are mounted in an insulated enclosure which is continuously flushed with argon to prevent oxidation of the yarn. Temperature is measured on the surface of the yarn by a two-color optical pyrometer. The whole assembly is depicted in Figure 38, and Figure 39 shows the interior of the enclosure while the coating process is being conducted.

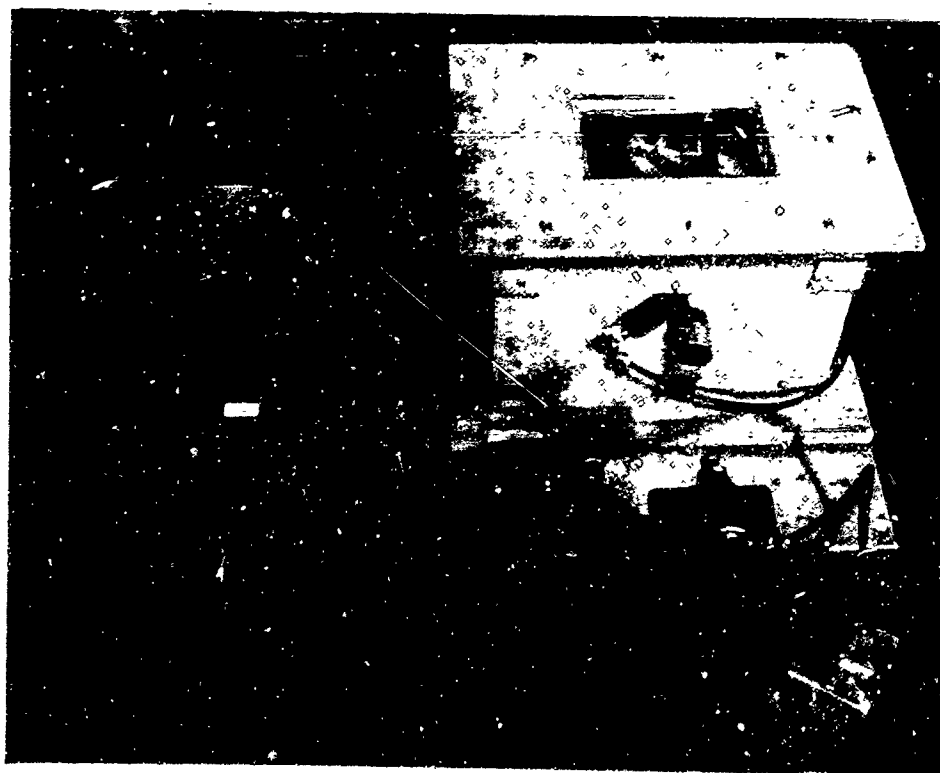


Figure 38. Equipment for Coating Graphite Yarn with Pyrolytic Carbon

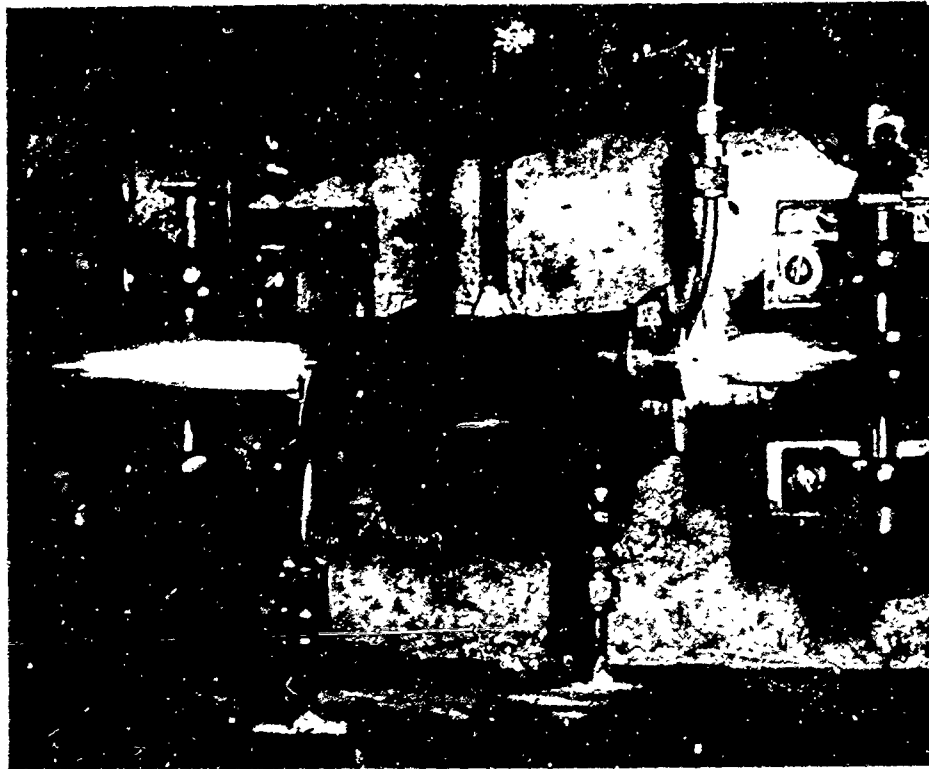


Figure 39. Interior View of Yarn Coating Apparatus in Operation

Strengths of the yarns produced in the above equipment were measured with the device as shown in Figure 40. Since clamping of the yarn, as is commonly done in textile testing, resulted in a shear stress and crushed the thin pyrolytic coating, frictional forces were used to hold the yarn. In this design (Figure 40) frictional forces are distributed exponentially over the lower fixed pulleys according to Eitelwein's formula:

$$P_x = P_{x=0} \cdot C^{\frac{-\mu x}{R}} \quad (2)$$

where:  $x$  = length coordinate for the yarn in contact with the pulley circumference

$P_x$  = force at the length  $x$  as measured from the point of first contact

$C$  = Eulers number

$\mu$  = coefficient of friction for coated yarn in contact with the graphite pulley surface

$R$  = radius of the pulley

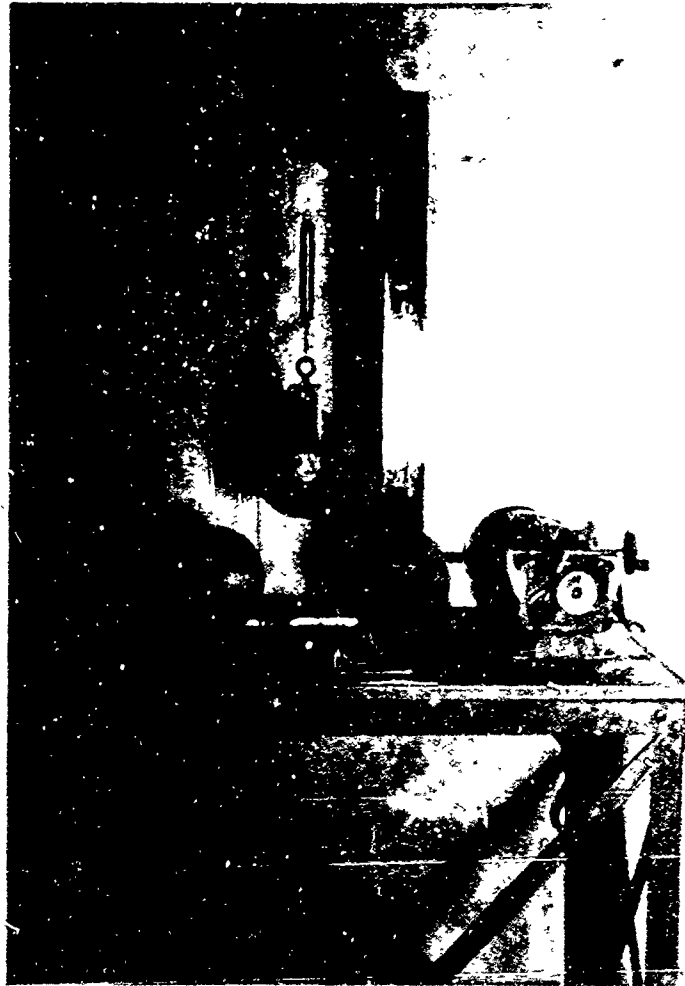


Figure 40. Pyrolytic Yarn Pull-Strength Testing Apparatus

The upper pulley in Figure 40 can turn freely, and is pulled upward by a steel cable connected to a variable speed gear motor. A spring scale located between the upper yarn pulley and the gear motor cable indicates the load. The use of the variable speed motor allows independent selection of the loading rate.

Variables involved in coating of the yarn are: (a) the yarn temperature which is also the deposition temperature, (b) the coating gas mixture, (c) the total gas flow rate, and (d) the speed of the yarn passing through the chamber. An evaluation of these variables was conducted and the results are presented in Figures 41 through 48. In each of these figures, the strength of the yarn is plotted in per cent of the original yarn strength. This procedure was necessary to correlate data from raw yarns having different strengths before coating. The strengths were then plotted at different temperatures as a function of the methane concentration in the coating gas with the independent variable being the yarn processing speed. Table 5 shows the typical physical test results for the coated and uncoated yarn.

RAW MATERIAL: Graphite yarn, 2.8 twists per inch

PROCESSING CONDITIONS: Yarn speed, 80 inches per minute

Argon flow, 42.5 std. ft<sup>3</sup>/hr

TEST CONDITIONS: Load rate: 5 lbs/min;  
6 samples per point

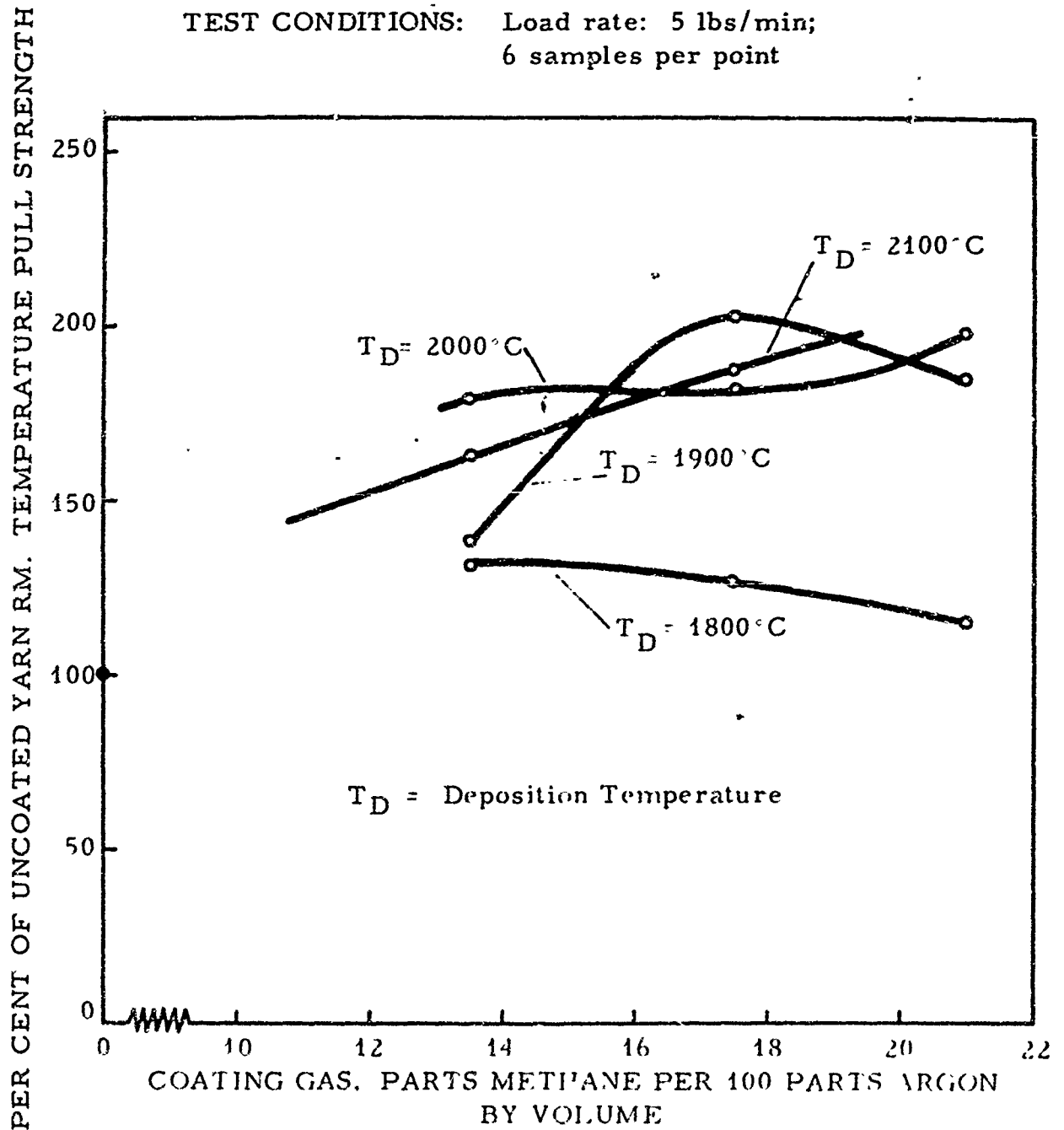


Figure 41. Pull Strength of Graphite Yarn Coated with Pyrolytic Carbon at a Process Speed of 80 in/min as a Function of the Methane Concentration in the Coating Gas

RAW MATERIAL: Graphite yarn, 2.8 twists per inch

PROCESSING CONDITIONS: Yarn speed, 100 inches  
per minute

Argon flow, 42.5 std.  
ft<sup>3</sup>/hr

TEST CONDITIONS: Load rate, 5 lbs/min;  
6 samples per point

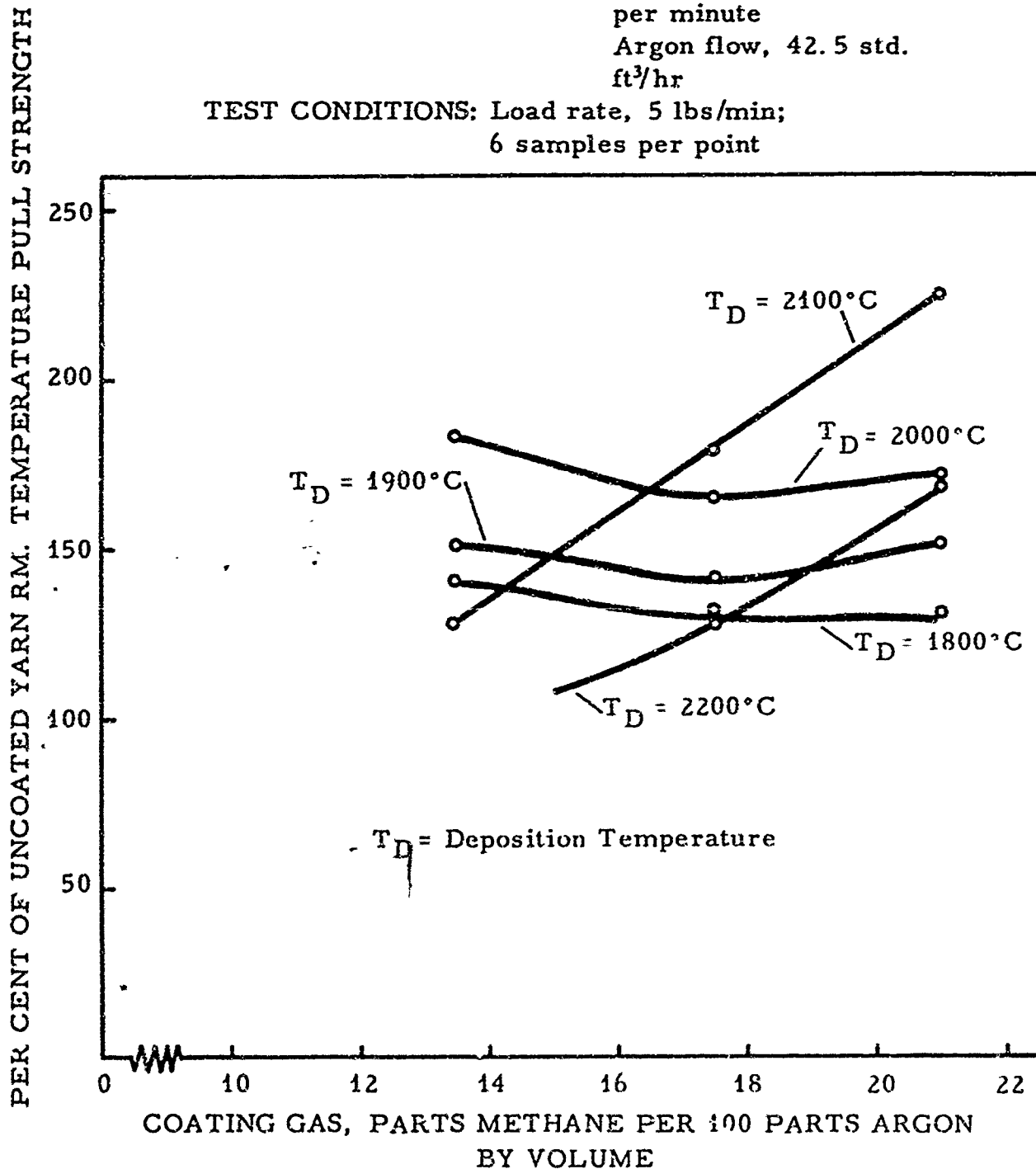


Figure 42. Pull Strength of Graphite Yarn Coated with Pyrolytic Carbon at a Process Speed of 100 in/min as a Function of the Methane Concentration in the Coating Gas

RAW MATERIAL: Graphite yarn, 2.8 twists per inch  
 PROCESSING CONDITIONS: Yarn speed, 120 inches  
 per minute  
 Argon flow, 42.5 std.  
 ft<sup>3</sup>/hr

TEST CONDITIONS: Load rate: 5 lbs/min;  
 6 samples per point

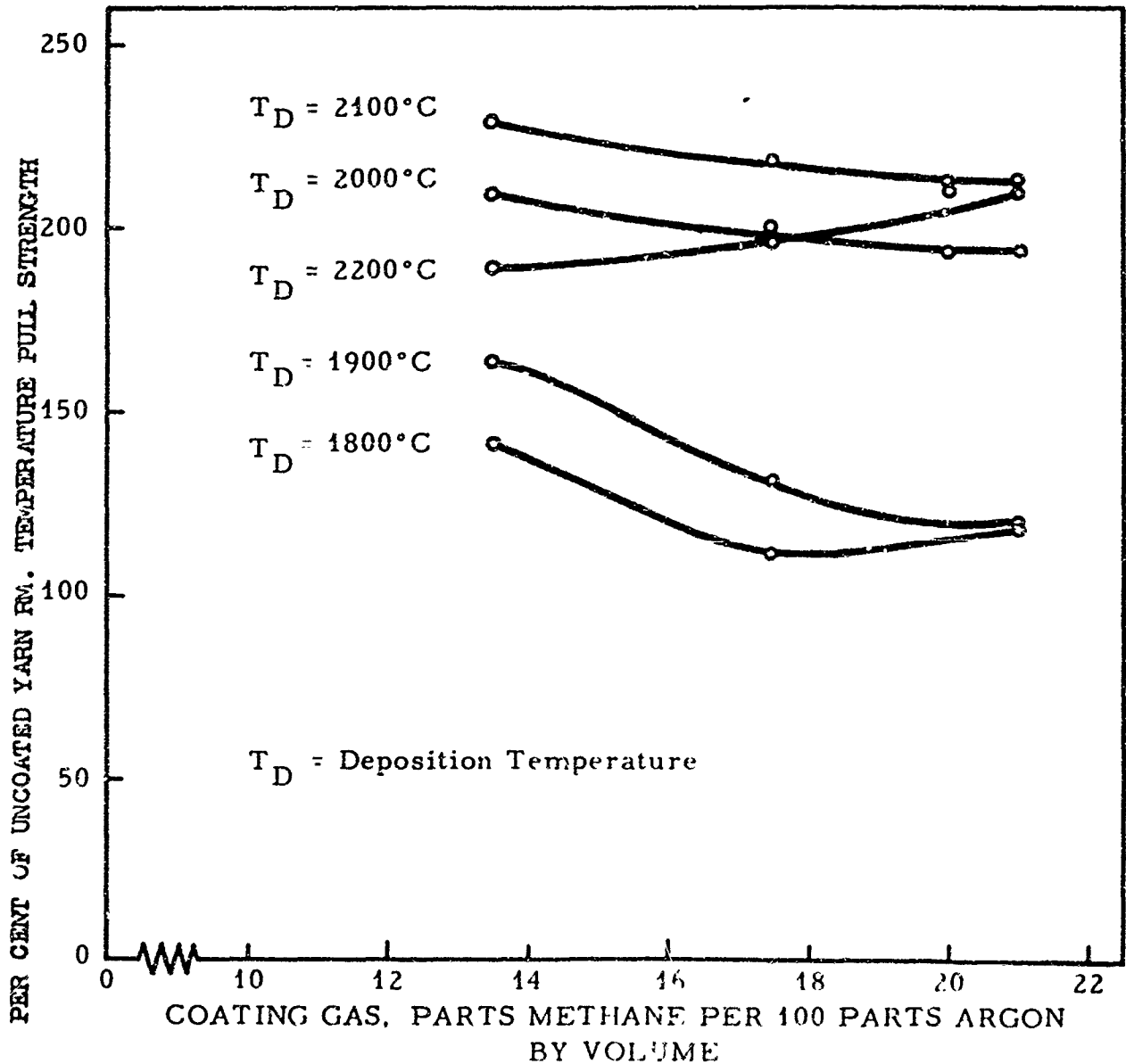


Figure 43. Pull Strength of Graphite Yarn Coated with Pyrolytic Carbon at a Process Speed of 120 in/min as a Function of the Methane Concentration in the Coating Gas

RAW MATERIAL: Graphite yarn, 2.8 twists per inch  
 PROCESSING CONDITIONS: Yarn speed, 150 inches  
 per minute  
 Argon flow, 42.5 std. ft<sup>3</sup>/hr.  
 TEST CONDITIONS: Load rate: 5 lbs/min;  
 6 samples per point

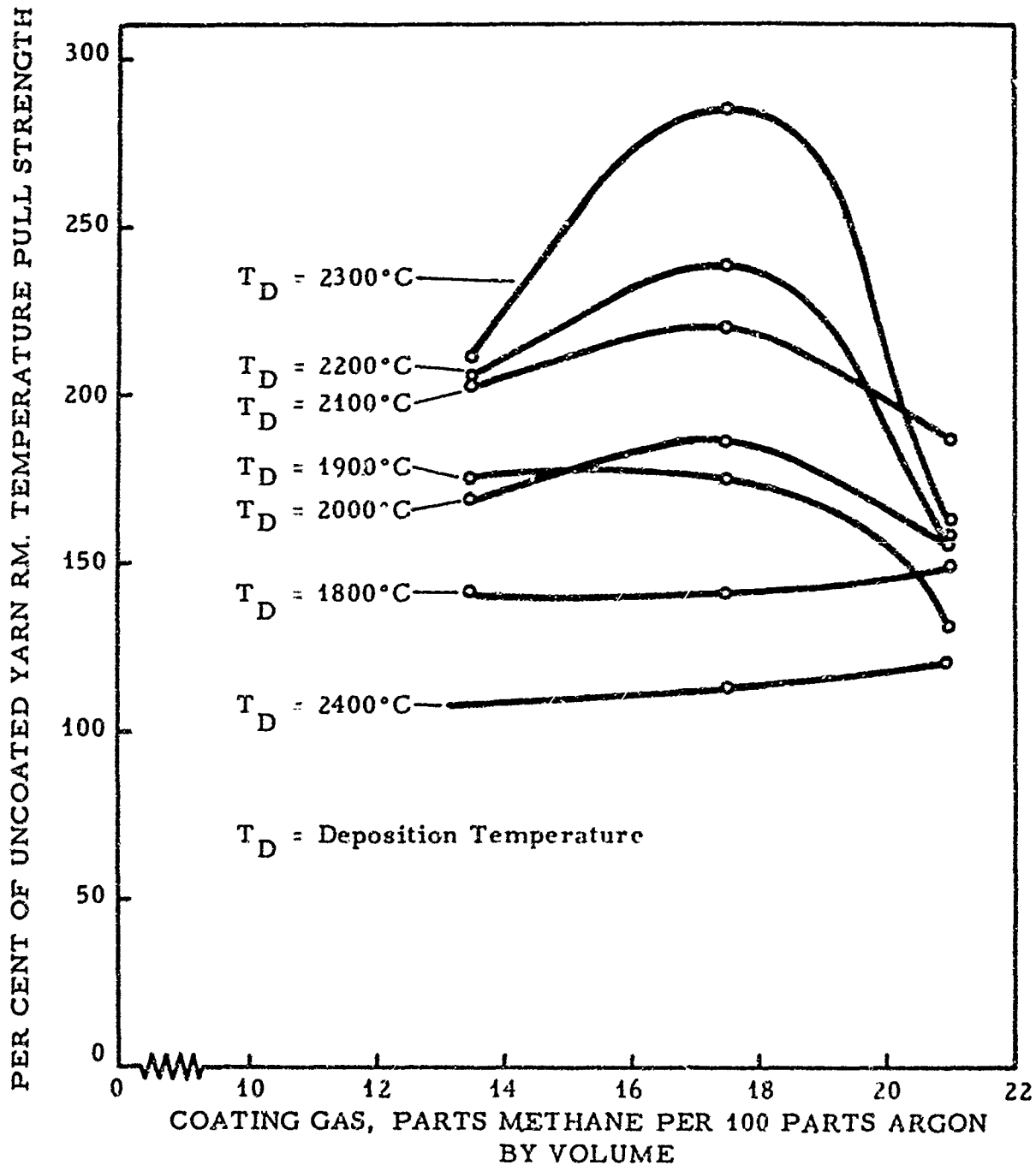


Figure 44. Pull Strength of Graphite Yarn Coated with Pyrolytic Carbon at a Process Speed of 150 in/min as a Function of the Methane Concentration in the Coating Gas

RAW MATERIAL: Graphite yarn, 2 8 twists per inch  
 PROCESSING CONDITIONS: Yarn speed, 175 inches  
 per minute  
 Argon flow, 42.5 std ft<sup>3</sup>/hr  
 TEST CONDITIONS: Strain rate, 1.0  
 inch/min;  
 5 samples per point

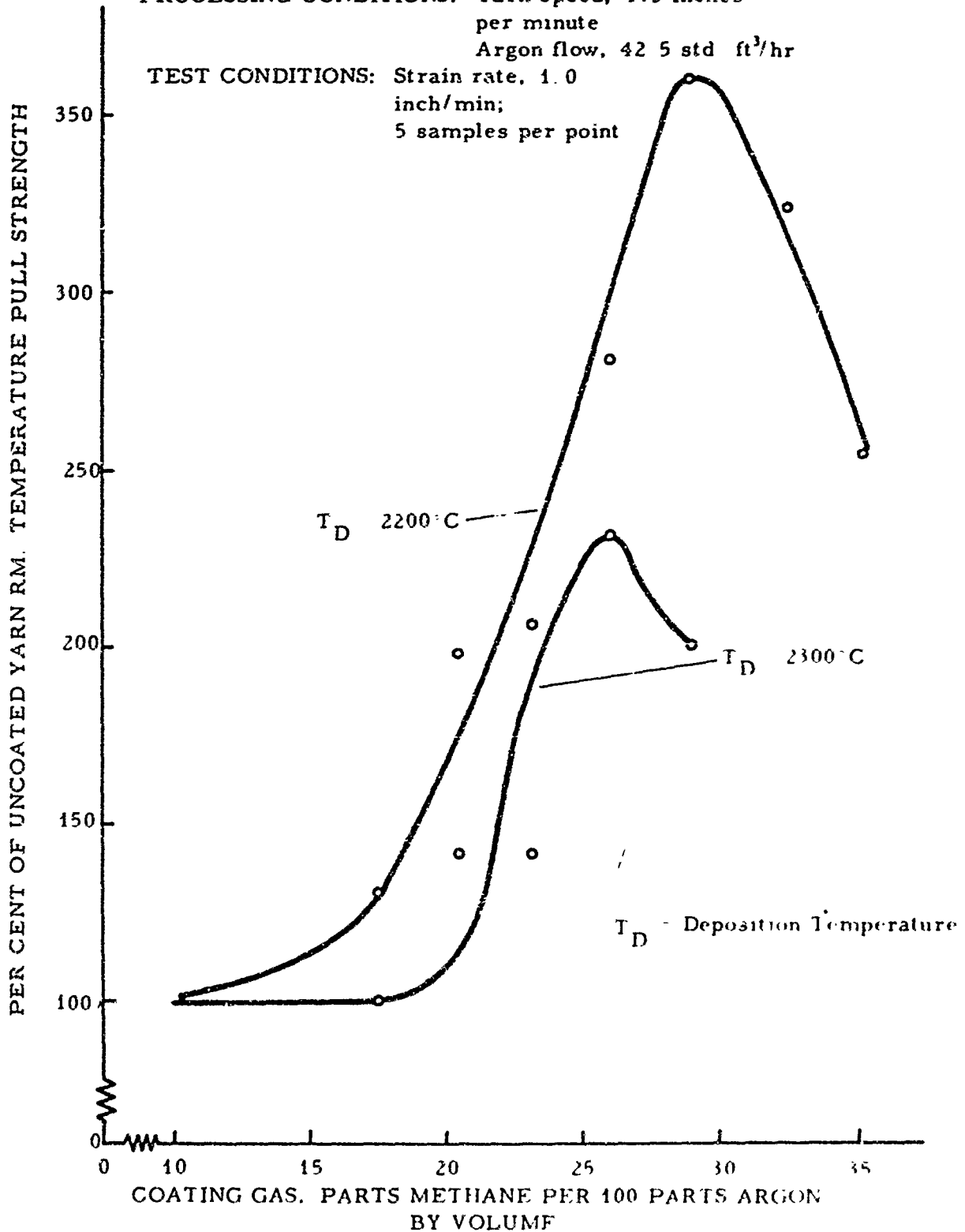


Figure 45. Pull Strength of Graphite Yarn Coated with Pyrolytic Carbon at a Process Speed of 175 in/min as a Function of the Methane Concentration in the Coating Gas

RAW MATERIAL: Graphite yarn, 2.8 twists per inch  
PROCESSING CONDITIONS: Yarn speed, 188 inches per minute  
Argon flow, 42.5 std. ft<sup>3</sup>/hr  
TEST CONDITIONS: Strain rate, 1.0 inch/min;  
5 samples per point

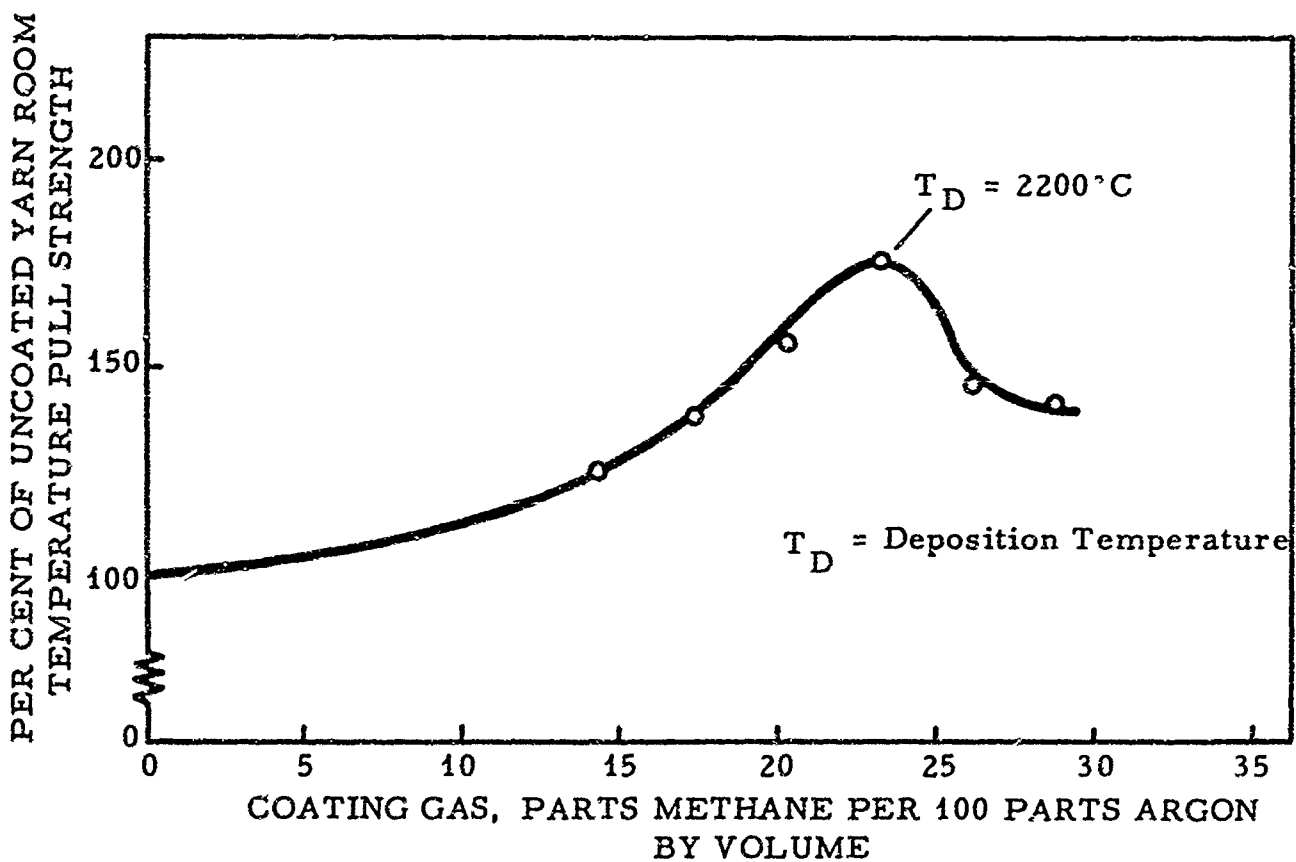


Figure 46. Pull Strength of Graphite Yarn Coated with Pyrolytic Carbon at a Process Speed of 188 in/min as a Function of the Methane Concentration in the Coating Gas

RAW MATERIAL: Graphite yarn, 2.8 twists per inch

PROCESSING CONDITIONS: Yarn speed, 200 inches  
per minute

Argon flow, 42.5 std.  
ft<sup>3</sup>/hr

TEST CONDITIONS: Strain rate: 1.0 inch/min;  
5 samples per point

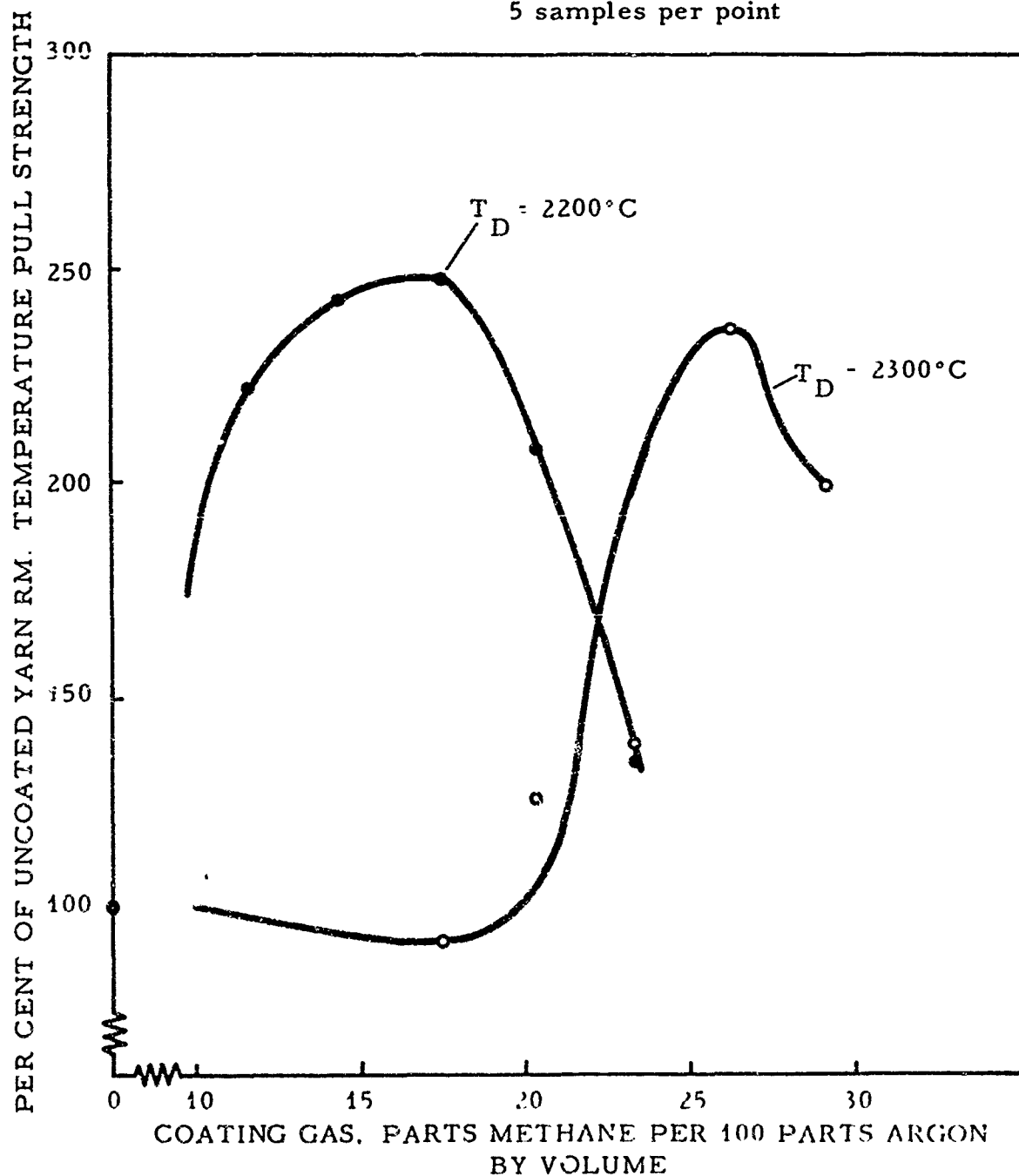


Figure 47. Pull Strength of Graphite Yarn Coated with Pyrolytic Carbon at a Process Speed of 200 in/min as a Function of the Methane Concentration in the Coating Gas

RAW MATERIAL: Graphite yarn, 2.8 twists per inch

PROCESSING CONDITIONS: Yarn speed, 225 inches  
per minute

Argon flow, 42.5 std.  
ft<sup>3</sup>/hr.

TEST CONDITIONS: Strain rate: 1.0 inch/min;  
5 samples per point

PER CENT OF UNCOATED YARN RM TEMPERATURE PULL STRENGTH

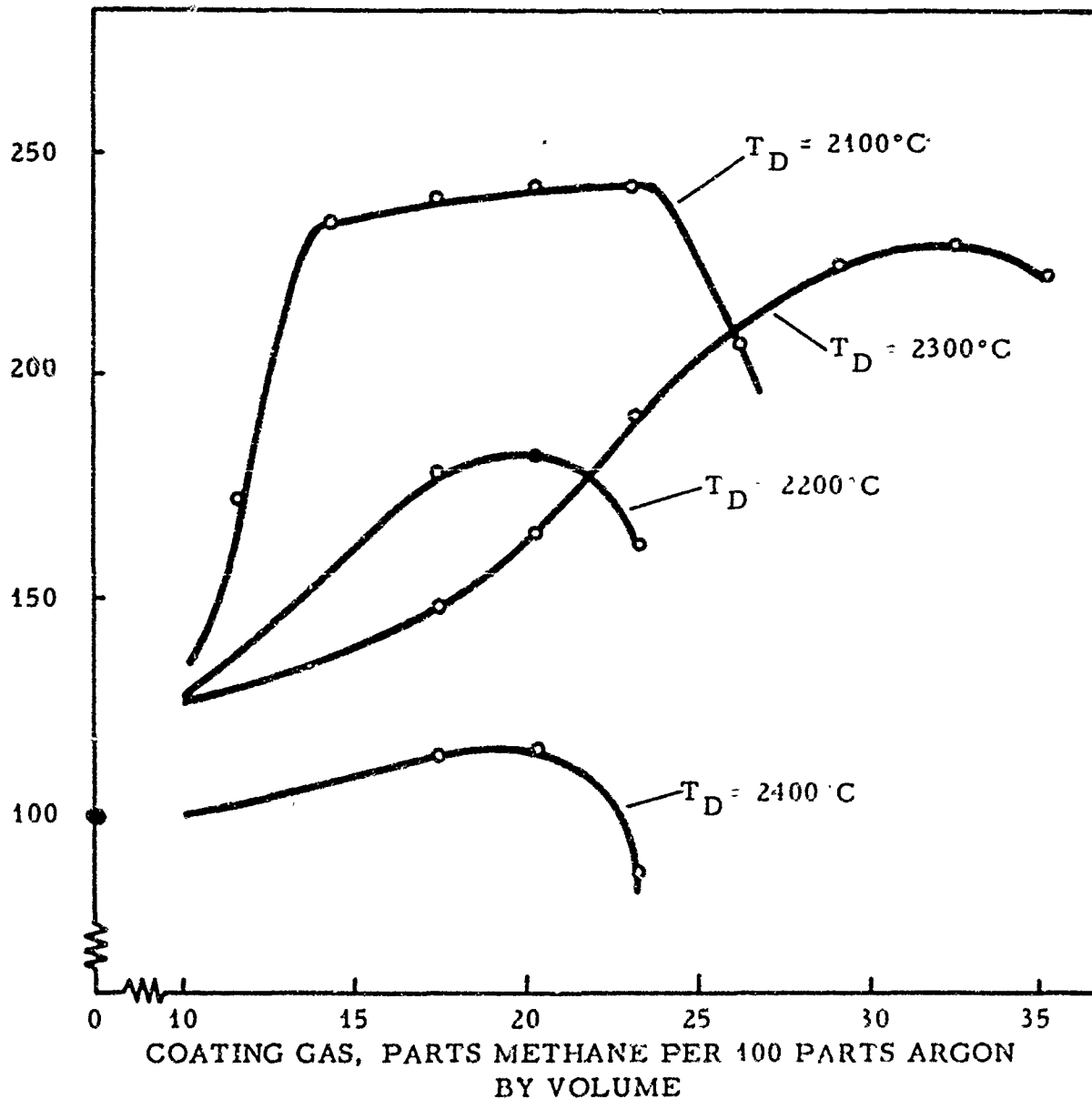


Figure 48. Pull Strength of Graphite Yarn Coated with Pyrolytic Carbon at a Process Speed of 225 in/min as a Function of the Methane Concentration in the Coating Gas

Table 5. Typical Results of Physical Tests on Coated and Uncoated Ten-Strand Graphite Yarn

Physical Properties	Uncoated Yarn		Yarn Coated with Pyrolytic Carbon				
	Sample No.		Sample No.				
	1	2	1	2	3	4	5
Denier, g/9000M	6210	6280	7190	7140	7070	7280	6880
Twist Ply, twists per inch	2.4	2.4	2.4	2.5	2.4	2.5	2.5
Breaking Strength, pounds-pull	3.5	4.2	10.3	8.8	6.4	9.7	10.6
Electrical Resistance,	3.1	3.1	1.1	1.2	1.3	1.2	1.2

Each physical property value is the average of 10 measurements

Analysis of the results presented in Figures 41 - 48 showed that there was an optimum deposition temperature for each yarn process speed which is essentially independent of the gas composition. The results also showed that the optimum deposition temperature increased with increasing yarn speed up to 150 inches per minute. Beyond this speed, the optimum deposition temperature was independent of the yarn speed (at least in the range investigated) but in no case exceeded 2300°C.

Figure 49 is a comparison of the uncoated and coated yarn. Photomicrographs (Figures 50 and 51) were taken of a section of coated yarn in order to determine the penetration of the coating into the yarn and to determine the manner in which the yarn was coated. In Figure 50 it can be seen that the coating completely surrounds those fibers located at the outer edge of the strand. Figure 51 shows the depth of penetration of the coating. It is plainly evident that the outer fibers receive the majority of the coating but that some fibers in the interior of the strands have at least a partial pyrolytic carbon coating.

Using the described coating equipment, yarns composed of ten strands (6210 denier) and 5 strands (2600 denier) have been successfully coated. Also, a single strand was separated from an original five-strand yarn and this also could be handled successfully. The single strand material (526 denier) has a two-pound pull breaking strength before coating and delicacy was required in handling the material.



Uncoated Yarn



Coated Yarn

Figure 49. Comparison of Uncoated (Top) and Pyrolytically Coated (Bottom) Graphite Yarn

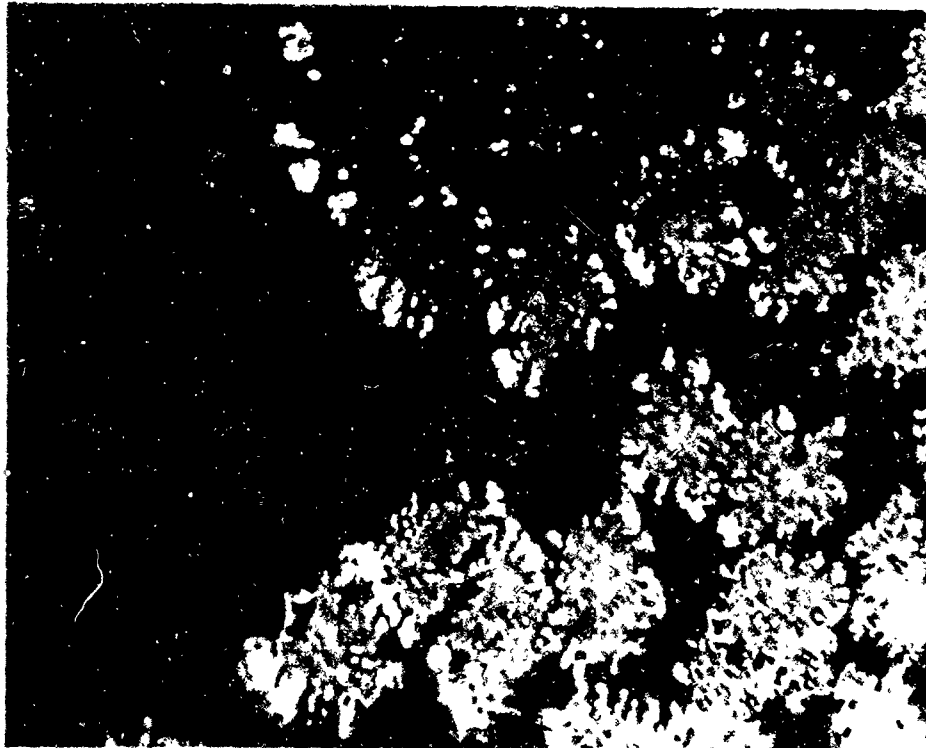


Figure 50. Graphite Yarn Fibers Coated with Pyrolytic Carbon, 1000X

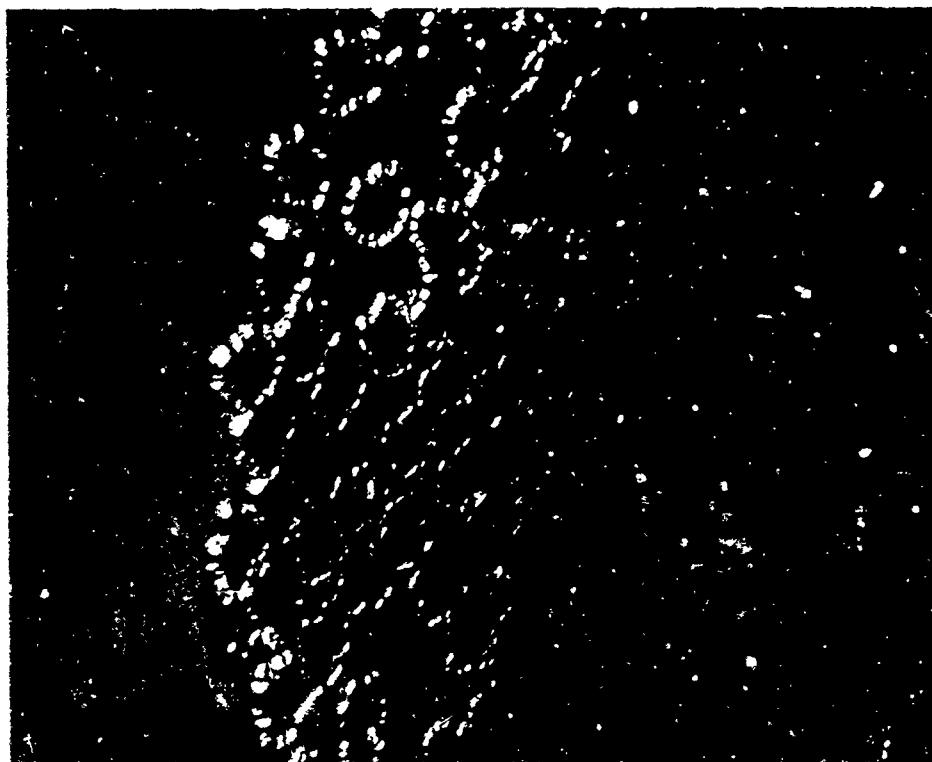


Figure 51. A Strand of Graphite Yarn Illustrating Depth of Penetration of Pyrolytic Carbon into the Individual Fibers, 500X

A curious characteristic is exhibited by the pyrolytically coated single strand yarn. The yarn can be bent to a radius of  $1/16$  of an inch and, when released, it will snap back to its original shape without any apparent filament damage. Uncoated and coated single strands are compared in Figure 52. As was the case with multiple strand yarns, the coated yarn looks like a steel cable while the uncoated yarn has the characteristic frayed appearance.



Figure 52. A Comparison of a Single Strand of Uncoated (Top) and Pyrolytically Coated (Bottom) Graphite Yarn, 12X

Figure 53, a photograph of coated yarn bent  $170^\circ$ , shows a few surface filaments projecting beyond the bend, but following the successive stages of straightening the yarn through Figures 54 and 55, until the yarn is completely straight again in Figure 56, these surface filaments blend into the strand and it is impossible to detect the point of bending even with a microscope.



Figure 53. Single Strand Graphite Yarn Coated with Pyrolytic Carbon and Bent at  $170^\circ$  Angle, 12X



Figure 54. Single Strand of Pyrolytically Coated Graphite Yarn Relaxed from  $170^\circ$  to  $45^\circ$  Angle, 12X



Figure 55. Single Strand of Pyrolytically Coated Graphite Yarn Relaxed from 170 to 20° Angle, 12X

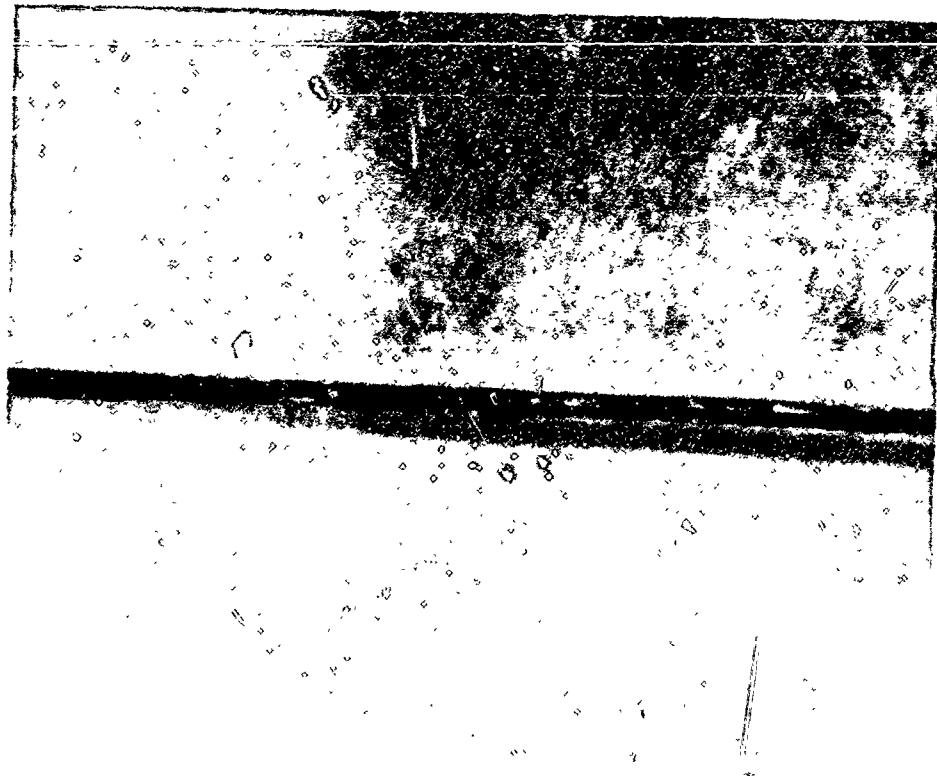


Figure 56. Single Strand of Pyrolytically Coated Graphite Yarn Completely Relaxed from 170° Angle, 12X

It was quite evident from the results obtained in these experiments that the strength of the graphite yarns was significantly increased by the application of thin pyrolytic carbon coatings. The maximum increase in strength obtained in these experiments was represented by a yarn with an uncoated pull strength of 2.4 pounds which increased to 8.67 pounds (360 per cent of the original strength) after the pyrolytic coating was applied.

In order to compare the strength of the coated and uncoated yarns with a normal yarn such as cotton or rayon, the tenacities of the yarns have been calculated. Tenacity used as an expression of strength for yarns, is based on the amount of load it takes to break a material of specified denier. Therefore, if the pull load required to break a 6000 denier yarn were 1200 grams, it would have a tenacity of 0.20 g/denier. Table 6 shows the tenacity of the uncoated and coated material for the ten, five, and single strand yarns.

Table 6. Comparison of Tenacity for Uncoated and Pyrolytic Coated Graphite Yarn

Number of Strands	Uncoated Graphite Yarn	Graphite Yarn Coated with Pyrolytic Carbon
10	0.256 g/denier	0.698 g/denier
5	0.640	1.28
1	1.99	2.41

The discussed investigation has demonstrated that pyrolytic carbon coatings can be applied successfully to graphite yarn and that the resultant yarn has increased strength while retaining the quality of flexibility that is so necessary in weaving the yarn into cloth.

#### 4. VAPOR DEPOSITED GRAPHITE

Experiments were conducted to determine the feasibility of producing pyrographite by condensation of carbon vapor at high temperatures. Two approaches, based on the same principle but each having a different physical setup, have been employed in this investigation. The principle of vapor deposition is that of heating a carbon body to a temperature where the vapor pressure is significant at atmospheric pressure, and condensing that vapor on a graphite receiver.

##### 4.1. Induction Heating for Vapor Deposition of Pyrolytic Carbon

The equipment for vapor deposition by induction heating is depicted in Figure 57. The graphite assembly is packed in lampblack

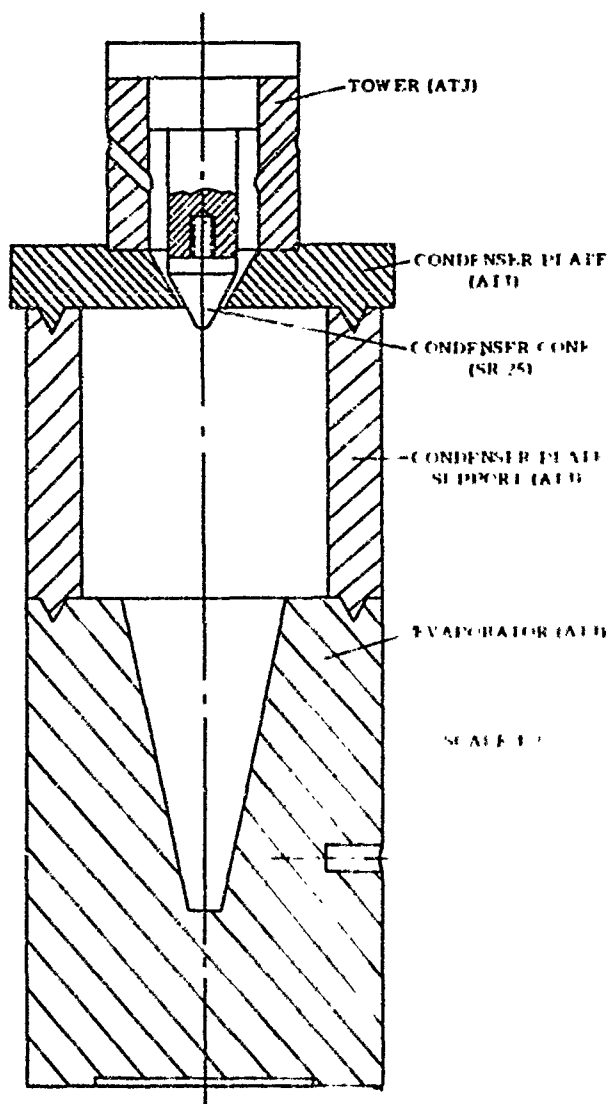


Figure 57. Graphite Assembly for Production of Vapor Deposited Pyrolytic Graphite by Induction Heating

inside a ceramic sleeve and the evaporator is centered in a 3000 cycle, 100 KW induction coil. Since the evaporator is centered in the coil, it receives the maximum heating whereas the condenser plate and cone are subject to a lesser field strength and, therefore, remain cooler. The evaporator is heated to a temperature between 3000 and 3400°C. When the vapor leaves the interior surface of the evaporator, it strikes and condenses on the condenser plate and cone. The structure and thickness of the deposit is determined by the temperature differential between the evaporator and the condenser section and by the length of time of deposition. Temperatures are measured by optical pyrometers sighted on the surface of the condenser plate and on the evaporator.

Pyrographite prepared in this manner is vastly different from that obtained by the thermal decomposition of hydrocarbons. The vapor deposited pyrolytic carbon (1/16-inch thick) shown in Figure 58 was obtained in about 20 minutes, and adhered very tightly to the substrate making removal almost impossible. The structure of vapor deposited pyrographite is illustrated at various magnifications in Figure 59. The

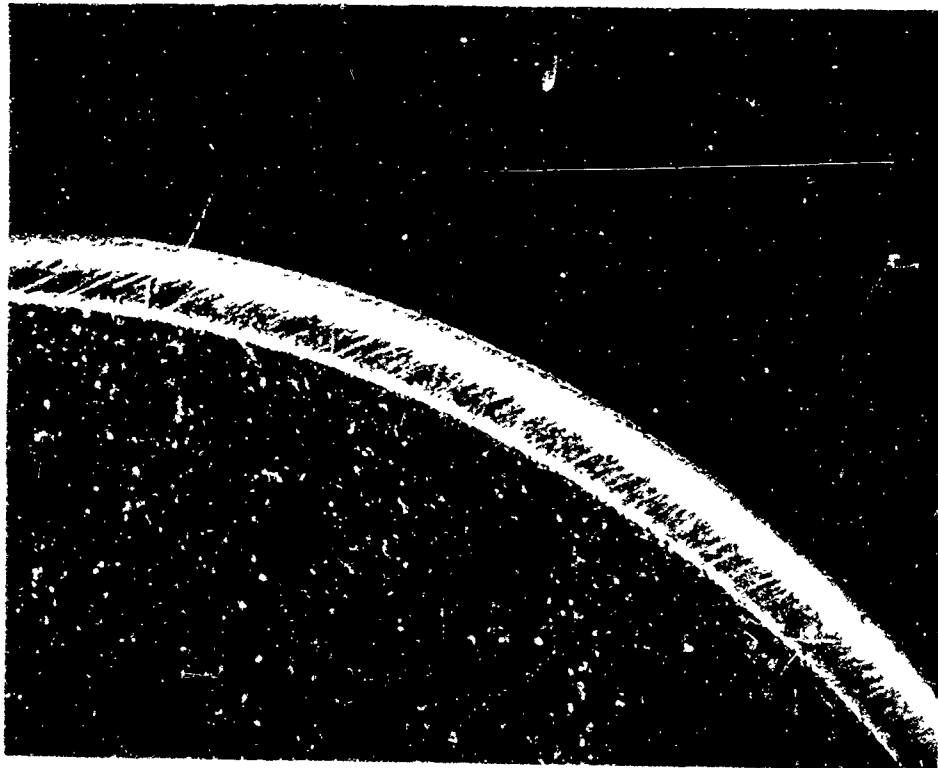


Figure 58. Macrograph of Vapor Deposited Pyrolytic Carbon, 12X



Upper Portion Vapor Deposited Graphite,  
Lower Portion Carbon Substrate

Figure 59. Pyrolytic Carbon by Vapor Deposition, 50X, 100X and 250X

structure of this material was unique in that it showed no preferential orientation. This was the exact opposite of pyrolytic graphite deposited from hydrocarbon gases which has a high degree of orientation. The vapor deposited material should, therefore, exhibit a high degree of isotropy which should permit thick deposits of pyrolytic carbon to be placed on curved surfaces. The low bulk density of the vapor deposited pyrolytic carbon, 1.61 g/cc, is confirmed by the pore spectrum analysis shown in Figure 60. Most of the pores fall within a narrow range of theoretical pore diameters which is in excellent agreement with the uniformity of the crystallites as observed in the photomicrographs of Figure 59.

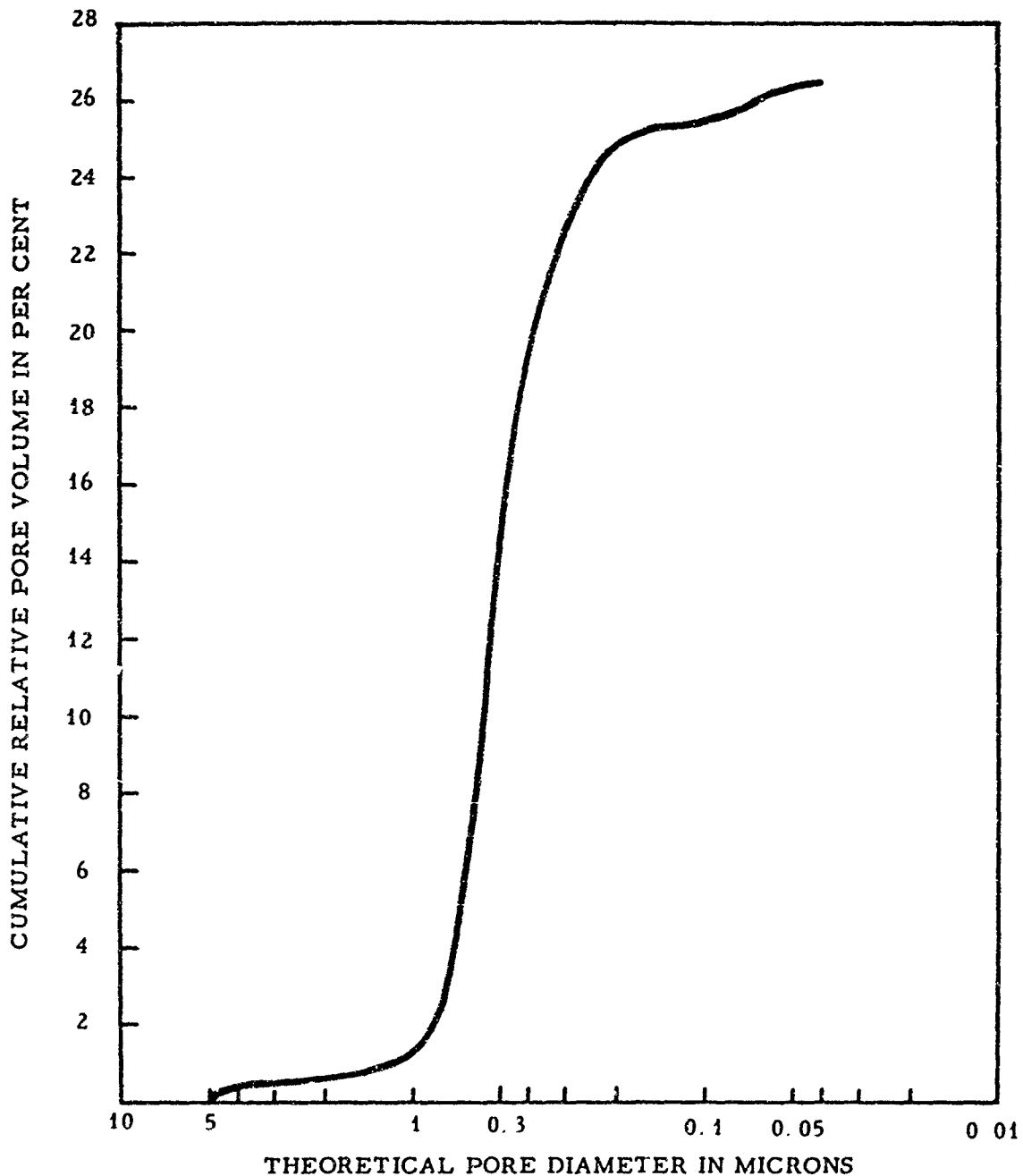


Figure 60. Porosity Characteristic of Vapor Depositing Carbon

#### 4.2. Resistance Heating for Vapor Deposition of Pyrolytic Carbon

One of the problems that was encountered in inductive heating for the vapor deposition of pyrolytic graphite was reproducibility of the evaporator and condenser temperatures. Small changes in the positioning of the graphite assembly in the coil resulted in significant changes in the temperatures. Also loading, firing and cooling time took at least 8 hours. The setup depicted in Figure 61, therefore, was constructed to make use of resistance heating of the evaporator. This equipment,

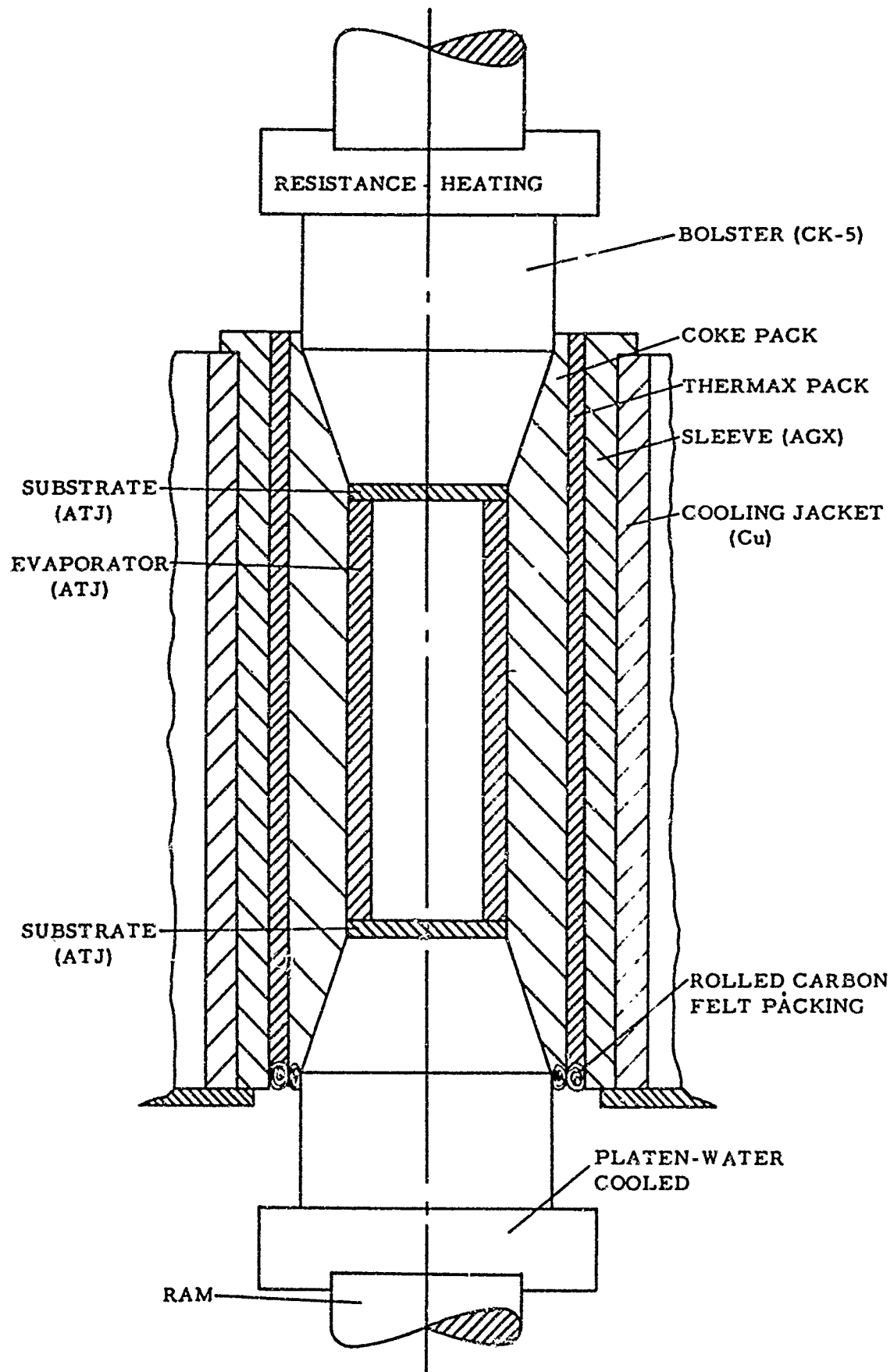


Figure 61. Apparatus for Deposition of Vapor Deposited Graphite by Resistance Heating

which can be loaded, fired, cooled and unloaded in as little as four hours, is described as follows: the evaporator and condenser plates are packed in coke particles and lampblack surrounded by a graphite sleeve. This assembly is then placed in a water-cooled jacket which is positioned between the electrical contacts. In this setup, the electrical power is supplied through the water-cooled rams of a 100 ton, double-action press. Electrical contact from the rams to the condenser plates is provided by graphite bolsters. Current is then passed through the graphite coating assembly and the evaporator is heated to sublimation temperatures (circa 3500°C). The heat sinks provided by the rams and bolster causes the condenser plates to remain at a substantially lower temperature than the evaporator, thus allowing the carbon vapor to condense on the plates. Since the specific resistance of the graphite is known and the geometry remains constant, reproducible vaporizing conditions can be obtained by using the same current density for each run.

The results using this method of vapor depositing the graphite have been even more promising than those obtained in the induction setup. Deposits of 1/8-inch thickness have been produced in 15 minutes at a current density of 1450 amps per square inch. This material, shown in Figure 62, had a density of 1.96 g/cc and a correspondingly low pore volume as shown in Figure 63.

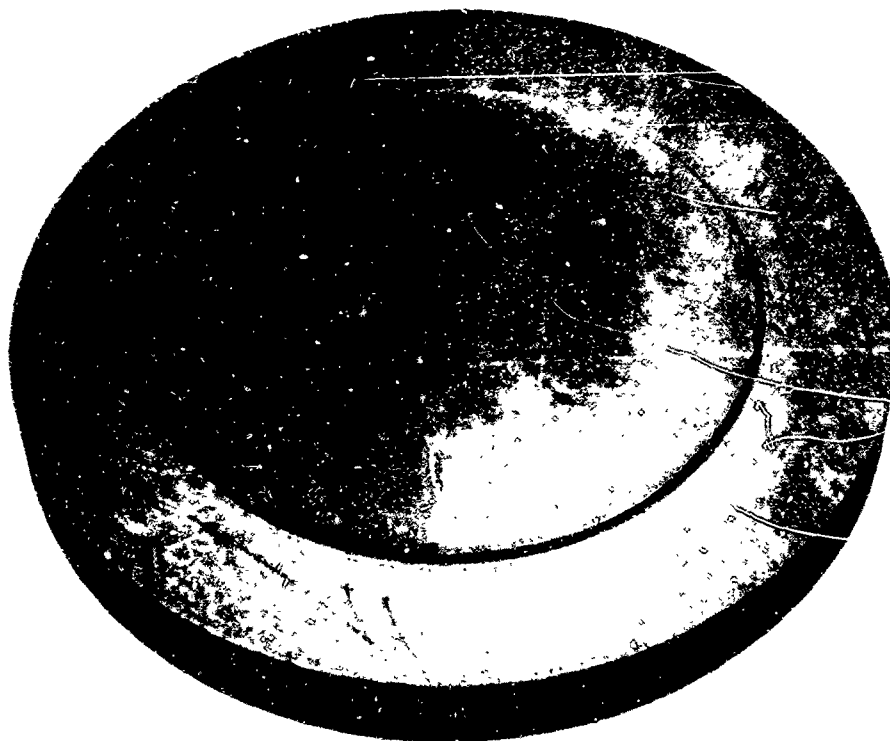


Figure 62. Pyrolytic Graphite Produced by Vapor Deposition

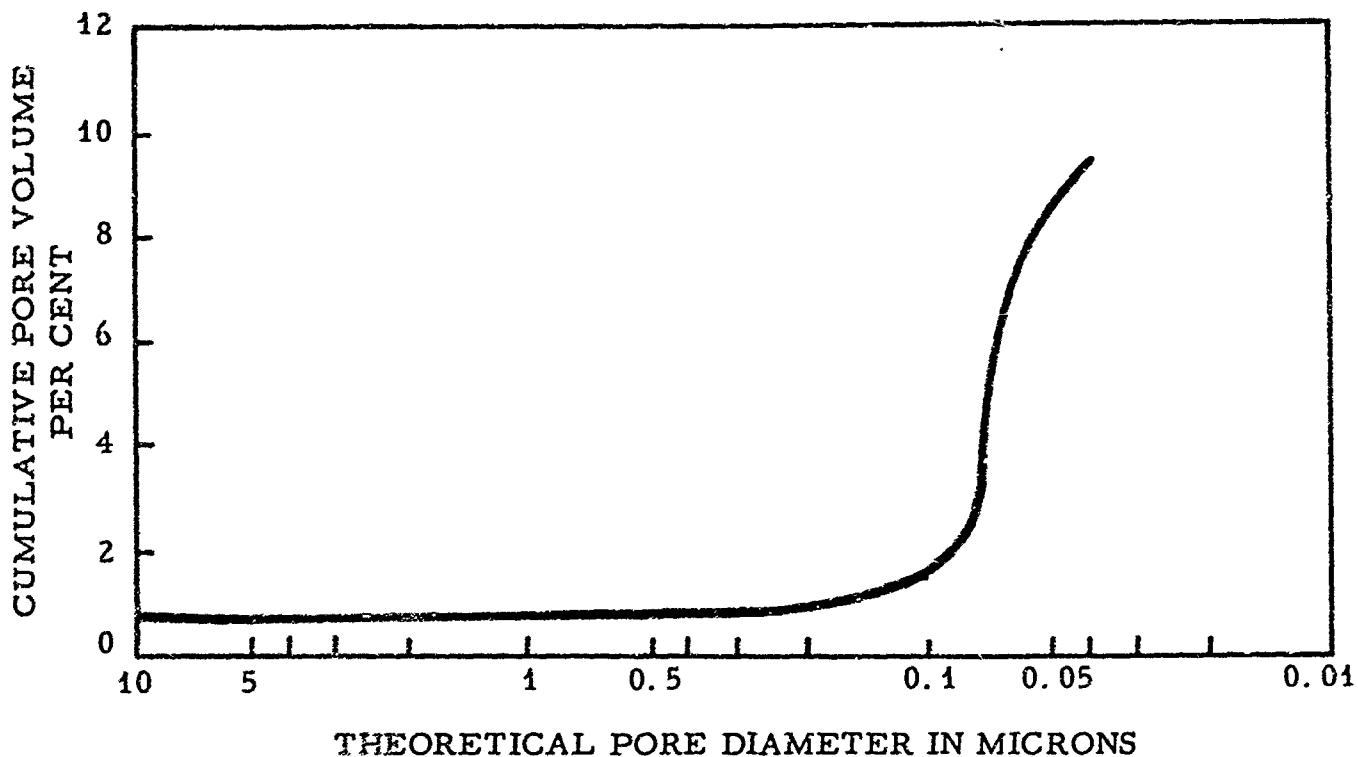


Figure 63. Porosity Characteristics of Vapor Deposited Graphite

A rather peculiar phenomenon occurred in the deposition of the material by this method in that, in certain instances, the deposit closely resembled the deposit obtained from gas decomposition. The material which is deposited by resistance heating of the evaporator normally consisted of three zones. Starting from the substrate surface, the first zone exhibited a fine needlelike structure commonly found on high quality pyrolytic graphite made by gas decomposition.

The second zone in the vapor deposited graphite is the transition region where oriented structure gradually vanishes (Figure 64) whereas the third zone shows no orientation at all (Figure 65). Neither of the structures in these latter two zones have ever been observed in pyrolytic

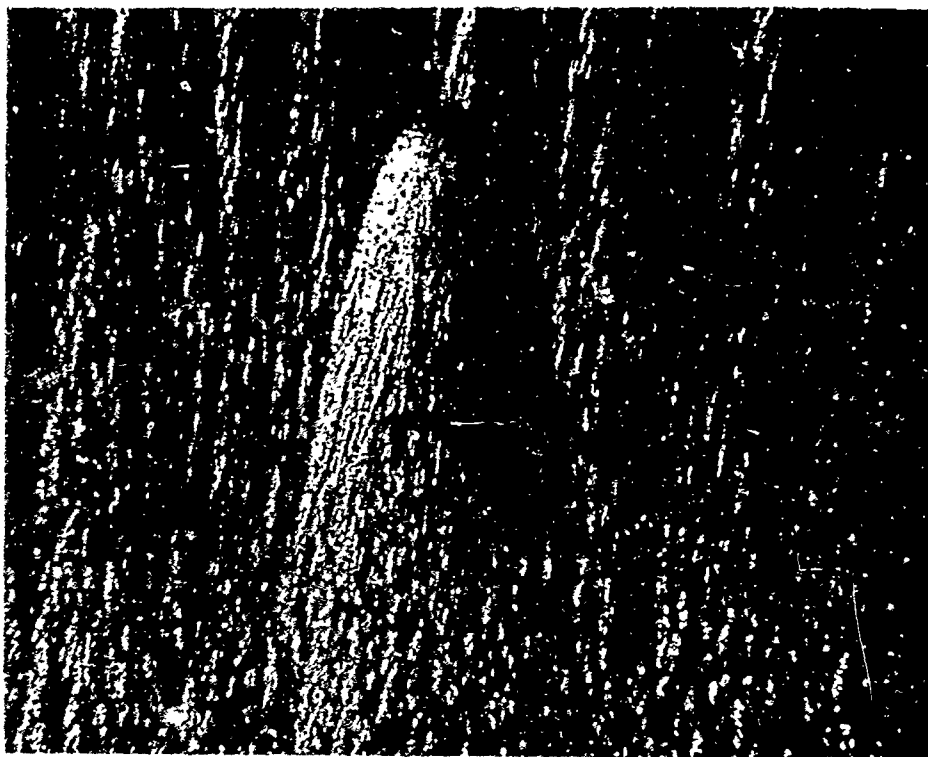


Figure 64. Structure Gradient in Vapor Deposited Pyrolytic Graphite, 500X

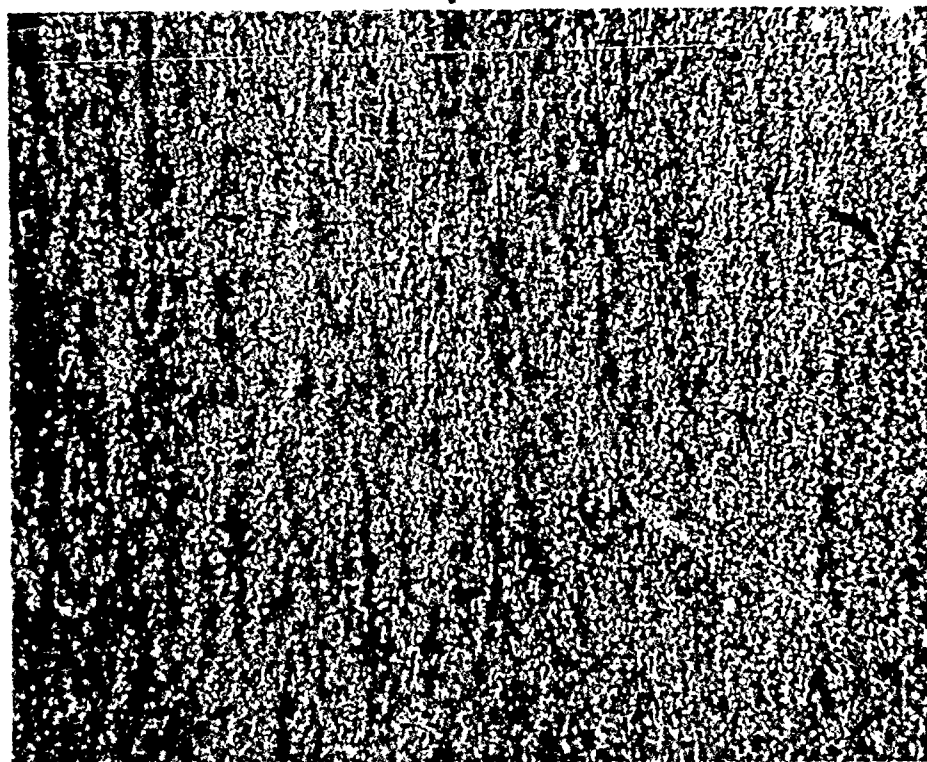


Figure 65. Isotropic Structure of Vapor Deposited Pyrolytic Graphite, 500X

graphite made by gas decomposition. It is well known that in pyrolytic materials from gas decomposition the structure generally deteriorates and certainly never improves with increasing thickness. In this new material the trend has been reversed. An attempt to explain this phenomena can be made by postulating that the condensation temperature increased as the thickness of the deposit increased. It is believed that in the resistance apparatus the initial temperature of the condenser plates may have been as low as 2000°C because of the enormous heat sinks constituted by the bolsters and the water-cooled rams. In the early stages of deposition, therefore, the carbon vapors formed a deposit closely resembling the deposit formed by gas decomposition at this temperature. Since this type material has a very low thermal conductivity in the transverse direction, the deposition surface became more and more thermally insulated against the heat sinks which brought the temperature of the condenser plate nearer to the temperature of the evaporator. By controlling the condensation temperature, the characteristics of vapor deposited graphites can be varied widely.

## 5. CONCLUSIONS

The following conclusions regarding pyrolytic carbon are drawn from the investigations discussed in this report. For convenience, the conclusions are divided into three sections, each of which covers a separate section of the report.

### 5.1. Pyrolytic Carbon Formed by Thermal Decomposition of Hydrocarbon Gas

---

- 1) The rate of deposition of pyrolytic carbon from the thermal decomposition of hydrocarbon gases:
  - a. Increases sharply with temperature up to 2000°C and approaches a constant value above 2000°C.
  - b. Increases with pressure but reaches a constant value which is dependent on other parameters.
  - c. Increases with hydrocarbon flux but reaches a saturation value for a given set of conditions.
  - d. Is independent of thermal and physical properties of the inert diluents, but is substantially reduced by a chemically active diluent such as hydrogen.
- 2) The deposition efficiencies are dependent on the conditions of temperature, pressure and gas compositions.
- 3) The density is temperature dependent, but a range of densities can be produced at a given temperature depending on the conditions.
- 4) The density varies inversely with the pressure over the limited range of 20 to 76 cm of Hg total pressure.
- 5) The microstructure of pyrolytic graphite is predominately temperature dependent over the range of 1.00 to 76.0 cm of Hg total pressure; however, the pyrolytic graphite is more oriented at low pressures and low deposition rates.
- 6) The low density deposits will anneal to very high densities and high density material will approach theoretical density upon annealing. Materials deposited at intermediate densities do not anneal.

## 5.2. Pyrolytic Carbon Coatings on Graphite Yarn

- 1) Graphite yarn can be mechanically reinforced by the application of microthin pyrolytic carbon coatings.
- 2) The increase in yarn strength is dependent on the conditions during deposition of the coating.
- 3) Significant increases in strength can be obtained at any process speed between 50 and 205 inches per minute.
- 4) There is an optimum deposition temperature for each yarn process speed which is essentially independent of gas composition.
- 5) The optimum deposition temperature increases with increasing yarn speed up to 150 inches per minute and thereafter is essentially independent of the yarn speed. In no case does the optimum deposition temperature exceed 2300°C.
- 6) Tenacity calculations show that the less the denier of the starting material (1 strand as opposed to 5 or 10 strands) the greater the increase in strength. The greatest benefit, therefore, can be derived by coating either the filaments or the single strands before spinning them into yarns.
- 7) Carbon and graphite yarns coated with pyrolytic carbon retain the desirable characteristics of flexibility and electrical conductivity.

## 5.3. Vapor Deposited Graphite

- 1) Pyrographite can be deposited at atmospheric pressure by sublimation of one graphite body and condensation of the vapor upon another body.
- 2) Pyrographite of specific structure and properties can be obtained by close control of the processing conditions.
- 3) Deposition rates are about an order of magnitude greater by this process than by conventional thermocracking of hydrocarbons.

## 6. RECOMMENDATIONS

The following recommendations are made with regard to pyrolytic carbon deposited by various means on various substrates.

### 6.1. Pyrolytically Coated Yarn

It is recommended that:

- 1) The coating of graphite or carbon yarn be extended to produce penetration of the coating gases to the core of the yarn.
- 2) The single strands and filaments of graphite and carbon yarn be pyrolytically coated before spinning them into yarn. It is believed that this procedure will produce increased tenacity of the finished yarn.
- 3) The pyrolytically coated yarn be woven into cloth to increase the overall strength of the product.

### 6.2. Vapor Deposited Graphite

It is recommended that:

- 1) Further studies of the deposition of pyrographite by sublimation and subsequent condensation of carbon be conducted to determine exact conditions for fabrication of a product with specified properties.
- 2) A full scale testing program be initiated to determine the physical properties of vapor deposited pyrographite and to determine the behavior of this material in rocket nozzles or under re-entry conditions.

## APPENDIX I. USE OF PREDICTABILITY CHARTS IN THE CALIBRATION OF FLOWMETERS

---

A predictability chart is supplied with the purchase of a flowmeter to enable the user to accurately calibrate the flowmeter for use with specific materials. To calibrate the flowmeter from the predictability curve, (Figure 66), it is necessary to know the viscosity and density of the fluid at the conditions of flow and the density of the fluid at standard conditions (70°F and 1 atm for gases). The procedure is as follows:

- 1) Calculate the weight of the immersed float  $F$  from the equation:

$$F = W \frac{\rho_f - \rho}{\rho_f} \quad (3)$$

where  $\rho$  = density of fluid in g/m at conditions of flow

$W$  = weight of the float in grams

$\rho_f$  = density of the float in g/ml.

- 2) Calculate the viscous influence  $N$  from the equation:

$$N = \frac{\mu}{\sqrt{W\rho}} \quad (4)$$

$\mu$  = viscosity of the fluid in centipoise at conditions of flow.

- 3) From the given predictability chart for the flowmeter, read off the values of  $K$  for each of the readings of the flowmeter corresponding to the value of  $N$  calculated from equation (4) above.

- 4) Calculate the instrument constant  $C$  by means of the equation:

$$C = \frac{453.6}{\rho_0} \cdot D_f \sqrt{F\rho} \quad (5)$$

where  $\rho$  = density of the fluid in g/ml at standard conditions

$D_f$  = diameter of float in inches.

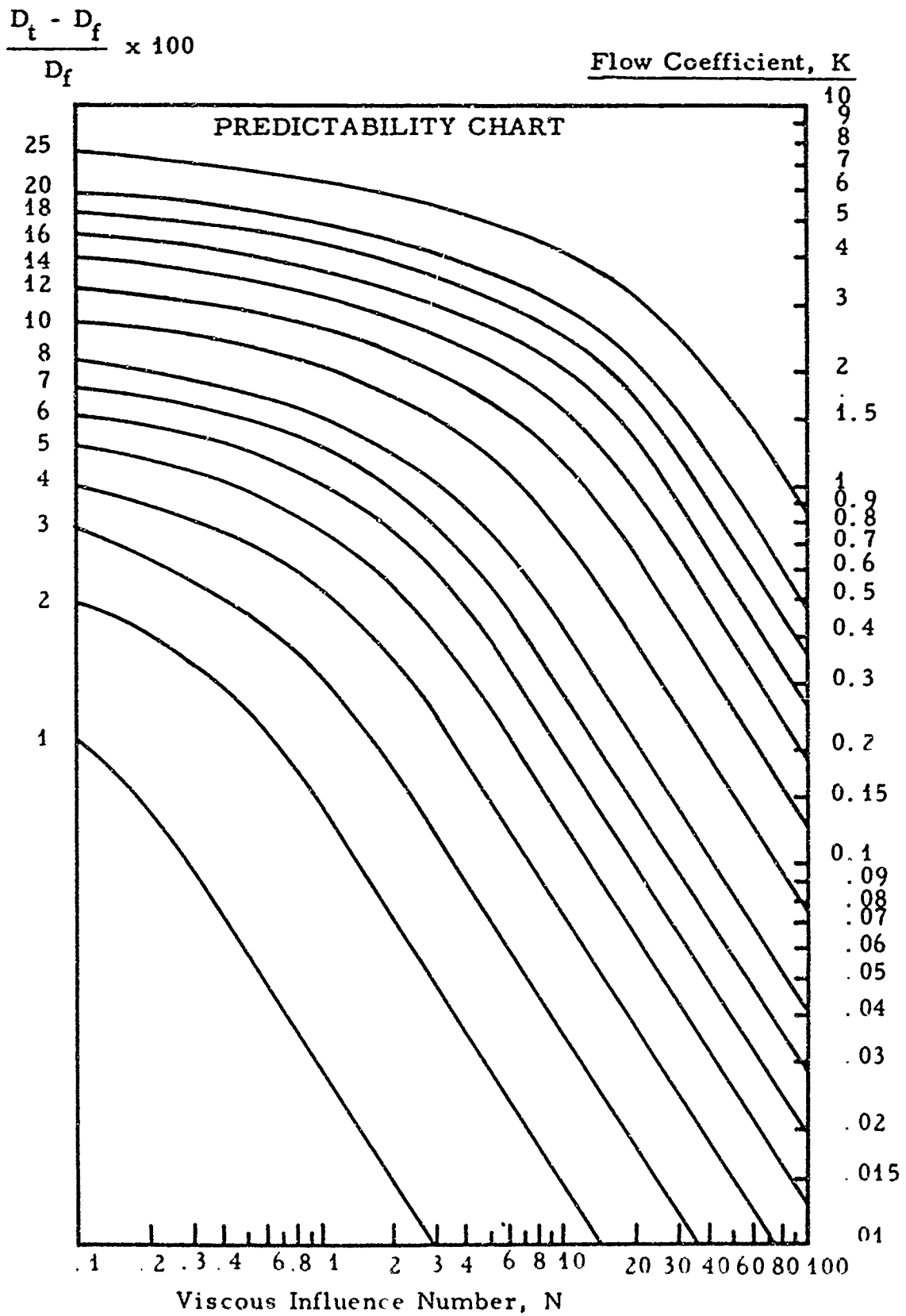


Figure 66. Predictability Chart for Use  
in Flowmeter Calibration

- 5) Calculate the flow  $V_o$  in standard ml/min for each value of K obtained by means of the equation:

$$V_o = CK. \quad (6)$$

To illustrate the method of calculation and the use of the above formulae, the calibration table for air flowing at 70°F and 1 atm. will be determined for a flowmeter using the sapphire ball float:

- 1) For air at 70°F and 1 atm.:

$$\rho = .001200 \text{ gms/ml.}$$

For Flowmeter No. 1 with sapphire ball, from Table 7:

$$W = .0084 \text{ gms.}$$

$$\rho_f = 3.98 \text{ gms/ml.}$$

Substituting in equation (3):

$$F = .0084 \left( \frac{3.98 - .0012}{3.98} \right) = .0084.$$

- 2) For air at 70°F and 1 atm:

$$\mu = .01814 \text{ cp.}$$

Substituting in equation (4):

$$N = \frac{.01812}{\sqrt{.0084 \times .00120}} = \frac{.01812}{.00318} = 5.70.$$

- 3) Reading from Predictability Chart (Figure 66), values of K are picked off each of the curves for  $(D_t - D_f) \times 100/D_f$  corresponding to the value of the viscosity influence number,  $N = 5.70$ . These values of K are given in Table 8.

- 4) For air, the density at standard conditions:

$$\rho_o = .001200 \text{ gms/ml.}$$

For flowmeter No. 1 with sapphire ball, from Table 7:

$$D_f = .0625 \text{ inches.}$$

Substituting in equation (5):

$$C = \frac{453.6}{.001200} \times .0625 \times .00318 = 75.0.$$

- 5) Multiplying each value of K by the instrument constant, C, according to equation (6) gives the required values of flow shown in the last column of Table 8.

Note that the readings on the flowmeter correspond to the percentage increase in the effective diameter of the tube,  $D_t$ , over that of the float,  $D_f$ . The effective diameter of the tube is that of a circle having the same inside cross-sectional area of the tube at the position of the reading.

Table 7. Data on Ball Floats

Flowmeter No.	Float Material	Density of Float, $\rho_f$	Weight of Float, W	Diameter of Float, $D_f$
		gms/ml	gms	inches
1	Sapphire	3.98	.0084	.0625
2	Stainless Steel	8.02	.0167	.0625
3	Sapphire	3.98	.0084	.0625
4	Stainless Steel	8.02	.0167	.0625
5	Sapphire	3.98	.0670	.125
6	Stainless Steel	8.02	.1330	.125
7	Glass	2.28	.3055	.250
8	Stainless Steel	8.02	1.066	.250
9	Glass	2.28	1.030	.375
10	Stainless Steel	8.02	3.595	.375

Table 8. Sample Calibration Table for Air at 70°F and 1 Atm. in Flowmeter No. 1 with Sapphire Ball

Reading of Flowmeter $\frac{D_t - D_f \times 100}{D_f}$	K	Flow in Std. ml. / min. at 70°F and 1 atm.
8	.570	42.8
7	.413	31.0
6	.282	21.2
5	.181	13.6
4	.103	7.7
3	.0494	3.7
2	.0175	1.3

## APPENDIX II. EFFECT OF TEMPERATURE, PRESSURE, AND COMPOSITION OF INFLUENT GAS ON THE EQUILIBRIUM COMPOSITION OF METHANE

---

Methane which is subjected to pyrolysis will yield an equilibrium composition which is affected by changes in temperature, pressure and composition of influent gas. The rate of pyrolysis is influenced not only by temperature, pressure, and composition, but also by gas flow velocity and condition of a char or catalytic surface on which the carbon is deposited.

It is informative to perform ordinary equilibrium composition calculations which disregard rate-influencing considerations and in that way to provide information about the quantitative effect of change in temperature, pressure or gas composition on the pyrolysis of methane. Such calculations have been made for the pyrolysis which is represented by equation (7).



It is emphasized that the attainment of equilibrium conditions is assumed in the following treatment.

The equilibrium constant  $K_p$  for equation (7) is

$$K_p = \frac{p_{\text{H}_2}^2}{p_{\text{CH}_4}} \quad (8)$$

in which  $p_{\text{H}_2}$  and  $p_{\text{CH}_4}$  are the partial pressures of hydrogen and methane. Equation 8 is valid provided that the fugacities and pressures of the gases are identical and that the vapor pressure of carbon is negligibly low at the temperatures which are employed. Using equation (8) it is easy to quantitatively determine the effect of changes in pressure, temperature and composition of gas on the equilibrium composition of the pyrolysis mixture.

Let  $a$  = the number of moles of  $\text{CH}_4$  added initially

$s$  = the number of moles of  $\text{H}_2$  added initially

$m$  = the number of moles of inert gas added initially

and  $x$  = the number of moles of  $\text{C}$  at equilibrium.

Then  $2x + s =$  the number of moles of  $H_2$  at equilibrium

and  $a - x =$  the number of moles of  $CH_4$  at equilibrium.

If  $P$  is the total pressure of the system, equation (8) may be restated as equation (9).

$$K_p = \frac{(2x + s)^2 P}{(a - x)(a + x + s + m)} \quad (9)$$

Solving equation (9) gives, for positive values of  $x$

$$x = \frac{-[s(K_p + 4P) + K_p m] + \sqrt{[s(K_p + 4P) \cdot K_p m]^2 - 4(K_p + 4P)[s^2 P - aK_p(a + s + m)]}}{2(K_p + 4P)} \quad (10)$$

Equation (10) permits the calculation of the equilibrium composition pyrolysis mixture under all conditions of temperature, pressure and addition of hydrogen or inert gas for which the gas mixtures behave ideally and for which the equilibrium constants or, equivalently, the standard free energy, of the reaction is known. The first two columns of Table 9 are copied directly from the American Petroleum Institute Tables which have been compiled for the reaction  $C + 2 H_2 = CH_4$ .

The  $K_p$  values in the third column are merely the reciprocals of the equilibrium constants of formation  $K_f$  calculated from  $\log K_f$ . The interconversion between  $K_p$  and  $T$  over the temperature range  $125^\circ C$  to  $1230^\circ C$  is facilitated by the use of Figure 67 which is a plot of the data in Table 9.

The general equation (10) becomes more tractable if simplifications for the three most likely cases are made.

In the first case, no gas is added at all, i. e. ;

$$s = 0$$

$$m = 0.$$

Equation (10) becomes

$$x = a \sqrt{\frac{K_p}{K_p + 4P}} \quad (11)$$

In the second case,  $s$  moles of hydrogen are introduced, but no moles of inert gas are added ( $m = c$ ). Equation (10) becomes

$$x = 1/2 \sqrt{\frac{s^2 (K_p + 4P) - 4 [s^2 P - aK_p (a+s)]}{K_p + 4P}} - \frac{s}{2} \quad (12)$$

In the third case,  $m$  moles of inert gas are added and hydrogen is not added ( $s = 0$ ). Equation (10) becomes

$$x = \sqrt{\frac{m^2}{4} \left( \frac{K_p}{K_p + 4P} \right)^2 + a(a+m) \left( \frac{K_p}{K_p + 4P} \right)} - \frac{m}{2} \left( \frac{K_p}{K_p + 4P} \right). \quad (13)$$

Equations (11), (12) and (13) may be restated in terms of mole fraction yield of carbon  $\frac{x}{a}$ . Then for the case

$$s = 0$$

$$m = 0$$

$$\frac{x}{a} = \sqrt{\frac{K_p}{K_p + 4P}} \quad (14)$$

For the case

$$s \neq 0$$

$m = 0$  define a hydrogen dilution ratio  $r = \frac{s}{a}$ . In terms of the hydrogen dilution ratio, the yield is given by

$$\frac{x}{a} = \left(1 + \frac{r}{2}\right) \sqrt{\frac{K}{K_p + 4P}} - \frac{r}{2} \quad (15)$$

Finally, for the case

$$s = 0$$

$m \neq 0$  define an inert gas dilution ratio  $t = \frac{m}{a}$ . The expected yield is then

$$x = \sqrt{\frac{t^2}{4} \left(\frac{K_p}{K_p + 4P}\right)^2 + (1+t) \left(\frac{K_p}{K_p + 4P}\right)} - \frac{t}{a} \left(\frac{K_p}{K_p + 4P}\right) \quad (16)$$

Table 9. The Equilibrium Constant for the Pyrolysis of Methane

Temperature ° K	Log $K_p$	$K_p$
0	- ∞	0
250	-11.3534	
298.16	- 8.8985	
300	- 8.8164	
350	- 6.9393	
400	- 5.4899	.000003
450	- 4.3558	.000037
500	- 3.4273	.000374
600	- 2.0004	.009991
700	- 0.9529	.1111
800	- 0.1500	.7080
900	+ 0.4881	3.077
1,000	+ 1.0075	10.18
1,100	+ 1.4345	27.19
1,200	+ 1.7936	62.17
1,300	+ 2.1006	126.1
1,400	+ 2.3638	231.1
1,500	+ 2.5923	391.1

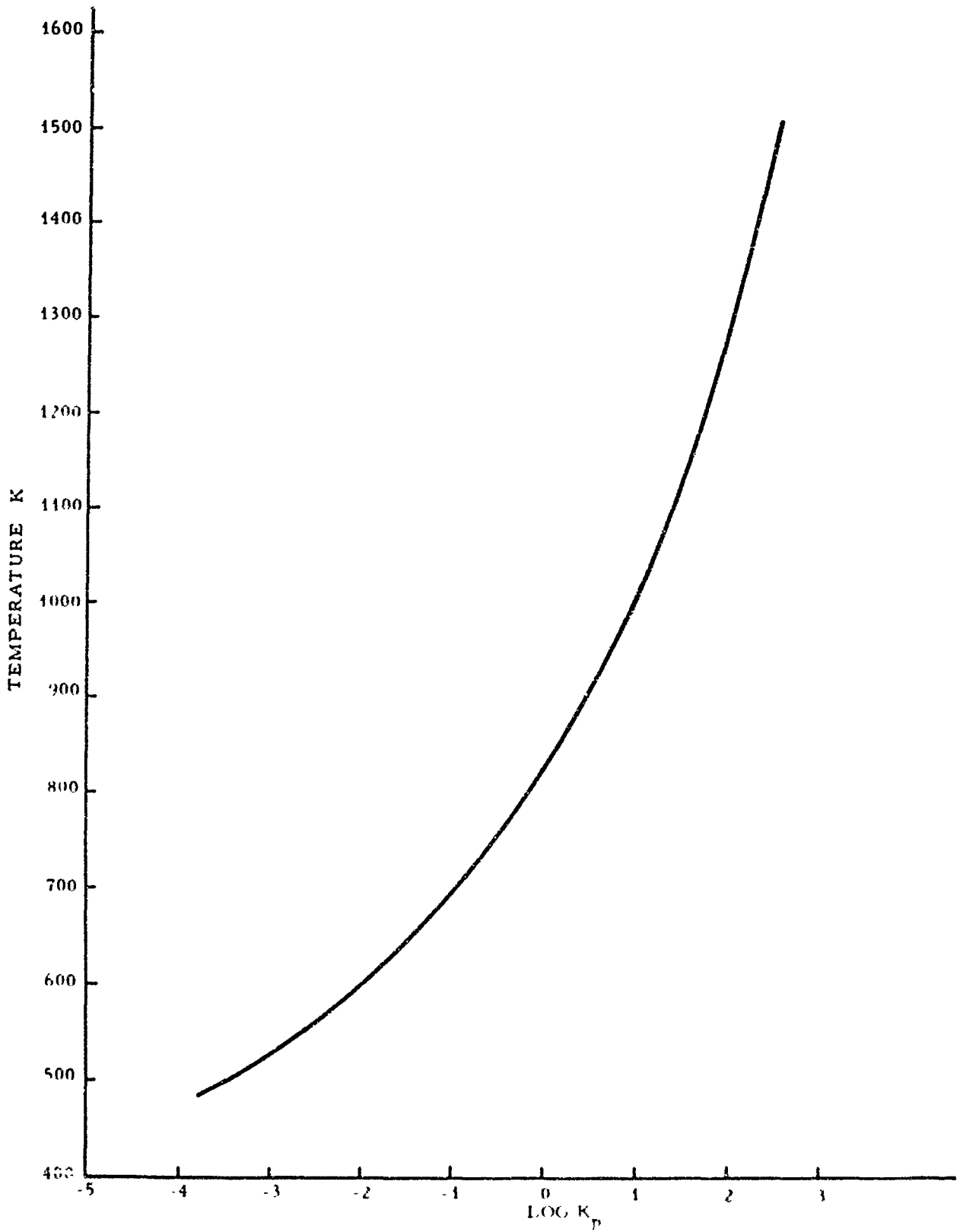


Figure 67. Variation of Log K<sub>p</sub> with Temperature

Table 10 has been compiled from the solution of equation (14) for the three pressures  $P = 0.1$  atm,  $P = 1$  atm and  $P = 5$  atm. Figure 68, which depicts the data in Table 10 graphically shows that the greatest influence of pressure on equilibrium composition occurs at low temperatures, i. e., at temperatures for which  $K_p$  is less than, equal to, or not much greater than  $P$ . At high temperatures; i. e., temperatures for which  $K_p \gg P$ , the equilibrium composition is not sensitive to changes in pressures.

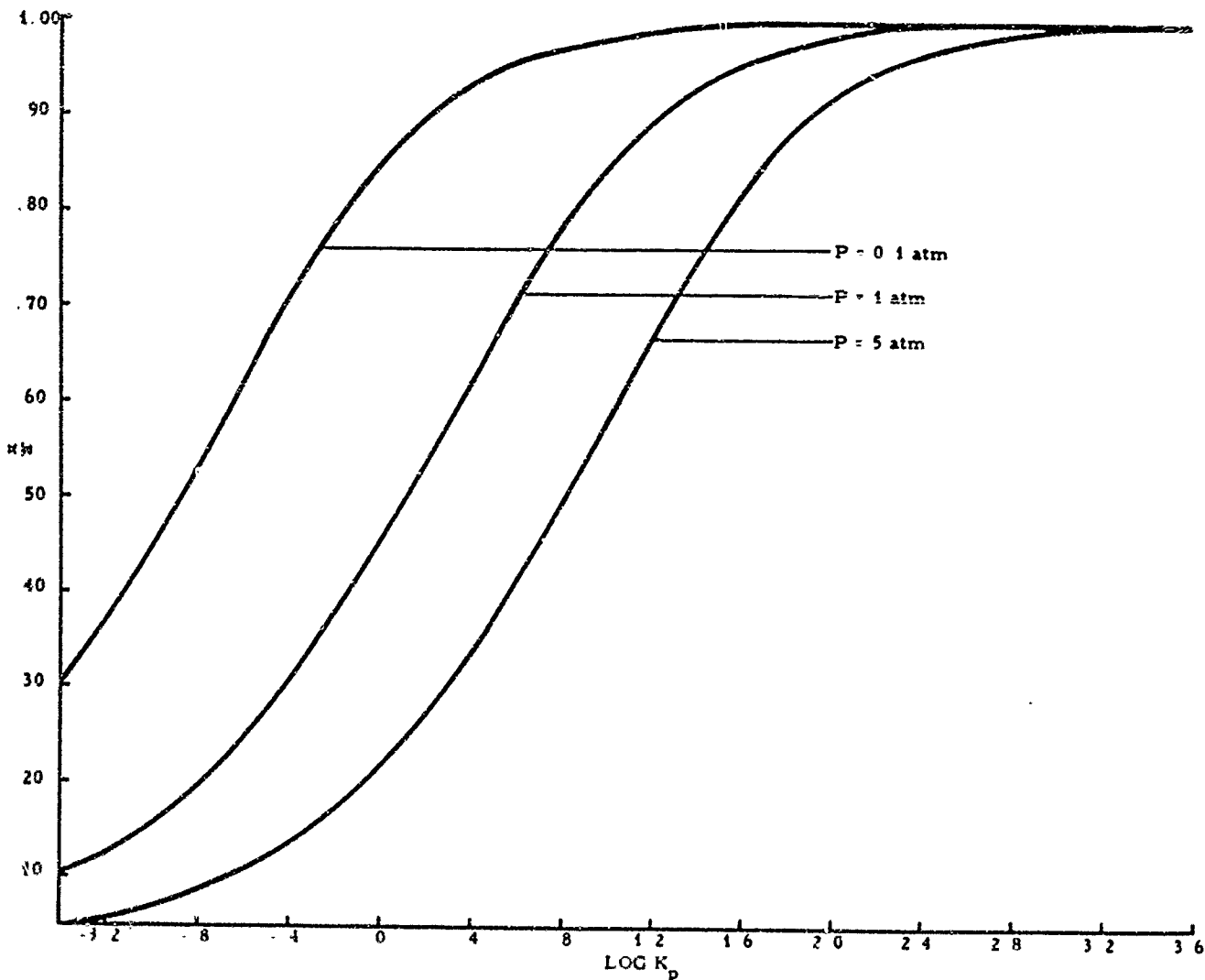


Figure 68. Equilibrium Composition ( $\frac{x}{a}$ ) Variation with  $\text{Log } K_p$  and Pressure, No Added Gases

Table 10. Equilibrium Composition of the Pyrolysis Mixture with no Added Gases

$K_p$	Log $K_p$	$\frac{x}{a}$		
		P = 0.1 atm	P = 1 atm	P = 5 atm
.05	-1.301	.333	.111	.0499
.1	-1.000	.447	.156	.0705
.2	-0.609	.577	.216	.0995
.3	-0.523		.264	.121
.4	-0.398	.707	.301	.140
.5	-0.301		.333	.156
.6	-0.222	.774	.361	.170
.7	-0.155		.386	.184
.8	-0.0969	.816	.408	.196
.9	-0.0458		.428	.207
1.0	0.0000	.845	.447	.218
2	0.301	.913	.577	.301
3	0.477		.655	.361
4	0.602	.953	.707	.408
5	0.699	.962	.745	.447
7	0.845	.972	.797	.509
10	1.000	.980	.845	.577
13	1.114	.985	.875	
16	1.204	.987	.894	.667
20	1.301	.990	.913	.707
25	1.398	.992	.928	.745
30	1.477		.939	.775
40	1.602	.995	.953	.816
50	1.699	.996	.962	.845
100	2.000	.998	.980	.913
200	2.301	.999	.990	.953
400	2.602	~ 1.000	.995	.976
800	2.903		.998	.988
1,600	3.204		.999	.994
4,000	3.602		~ 1.000	.995
10,000	4.000			.999
20,000	4.301			~ 1.000
50,000	4.699			

Equation (15) has been used in two ways. The variation of equilibrium composition with pressure and various dilutions of hydrogen is given in tabular form in Tables 11, 12 and 13 and graphically in Figures 69, 70 and 71.

Table 11. Equilibrium Composition of the Pyrolysis Mixture;  
Hydrogen Added, No Inert Gas Added  
 $P = 0.1 \text{ atm}$

K P	Log K P	$\frac{x}{a}$					
		r = 1	r = 2	r = 3	r = 4	r = 5	r = 6
.05	-1.301	0	----	----	----	----	----
.1	-1.000	.111	----	----	----	----	----
.2	-0.609	.366	.154	----	----	----	----
.3	-0.523						
.4	-0.398	.561	.414	.268	.121	----	----
.5	-0.301						
.6	-0.222	.661	.548	.435	.312	.209	.096
.7	-0.155						
.8	-0.0969	.724	.632	.540	.448	.350	.264
.9	-0.0458						
1.0	-0.0000	.768	.691	.614	.537	.460	.383
2	0.301	.869	.826	.782	.737	.693	.649
3	0.477						
4	0.602	.929	.906	.881	.857	.833	.809
5	0.699	.943	.924	.905			.848
7	0.845	.958	.944	.930	.916	.902	
10	1.000	.970	.960	.950	.940	.930	.920
13	1.114	.977					
16	1.204	.980	.974	.966	.959	.952	.945
20	1.301						.960
25	1.398	.984		.980	.976	.972	.968
30	1.477						
40	1.602	.992	.990	.986	.983	.980	.977
50	1.699	.994					.984
100	2.000	.997	.996	.995	.994	.993	.992
200	2.301	.998	.997	.996	.995	.994	.993
400	2.602	.999					
800	2.903						
1,600	3.204						
4,000	3.602						
10,000	4.000						
20,000	4.301						
50,000	4.699						

Table 12. Equilibrium Composition of the Pyrolysis Mixture;  
Hydrogen Added, No Inert Gases Added

P = 1 atm

$K_p$	Log $K_p$	$\frac{x}{a}$					
		r = 1	r = 2	r = 3	r = 4	r = 5	r = 6
.05	-1.301	----	----	----	----	----	----
.1	-1.000	----	----	----	----	----	----
.2	-0.609	----	----	----	----	----	----
.3	-0.523	----	----	----	----	----	----
.4	-0.398	----	----	----	----	----	----
.5	-0.301	0	----	----	----	----	----
.6	-0.222	042	----	----	----	----	----
.7	-0.155	.079	----	----	----	----	----
.8	-0.0969	.112	----	----	----	----	----
.9	-0.0458	142	----	----	----	----	----
1.0	0.000	171	----	----	----	----	----
2	0.301	365	154	----	----	----	----
3	0.477	482	310	137	----	----	----
4	0.602	560	414	267	121	----	----
5	0.699	617	490	362	235	107	----
7	0.845	695	594	492	391	289	188
10	1.000	767	690	612	535	457	380
13	1.114	812	750	687	625	562	500
16	1.204	841	788	735	682	629	576
20	1.301	869	826	782	739	695	652
25	1.398	892	856	814	784	748	712
30	1.477	908	878	847	817	786	756
40	1.602	930	906	882	859	835	812
50	1.699	943	924	905	886	867	848
100	2.000	970	960	950	940	930	920
200	2.301	985	980	975	970	965	960
400	2.602	992	990	987	985	982	980
800	2.903	997	996	995	994	993	992
1,600	3.204	999	998	997	997	996	996
4,000	3.602						
10,000	4.000						
20,000	4.301						
50,000	4.699						

Table 13. Equilibrium Composition of the Pyrolysis Mixture;  
Hydrogen Added, No Inert Gas Added

P = 5 atm

K <sub>p</sub>	Log K <sub>p</sub>	$\frac{x}{a}$					
		r = 1	r = 2	r = 3	r = 4	r = 5	r = 6
1	0.000	----	----	----	----	----	----
2	0.301	----	----	----	----	----	----
3	0.477	.042	----	----	----	----	----
4	0.602	.112	----	----	----	----	----
5	0.699	.171	----	----	----	----	----
7	0.845	.264	.018	----	----	----	----
10	1.000	.322	.096	----	----	----	----
13	1.114	.441	.254	.068	----	----	----
16	1.204	.500	.332	.165	----	----	----
20	1.301	.561	.414	.268	.121	----	----
25	1.398	.618	.490	.363	.235	.108	----
30	1.477	.663	.550	.438	.325	.213	.100
40	1.602	.724	.632	.540	.448	.356	.264
50	1.699	.768	.690	.613	.535	.458	.380
100	2.000	.870	.825	.783	.739	.696	.652
200	2.301	.930	.906	.883	.859	.836	.812
400	2.602	.964	.952	.940	.928	.916	.914
800	2.903	.981	.974	.968	.961	.955	.948
1,600	3.204	.990	.986	.983	.979	.976	.982
4,000	3.602	.997	.996	.995	.994	.993	.992
10,000	4.000	.999	.998	.998	.997	.997	.996

If so much hydrogen is added so that

$$K_p < \frac{p^2_{H_2}}{p_{CH_4}} \quad (17)$$

the yield of carbon will be zero.

Solving equation (15) for the condition that x = 0 gives

$$K_p = \frac{r^2}{1+r} P \quad (18)$$

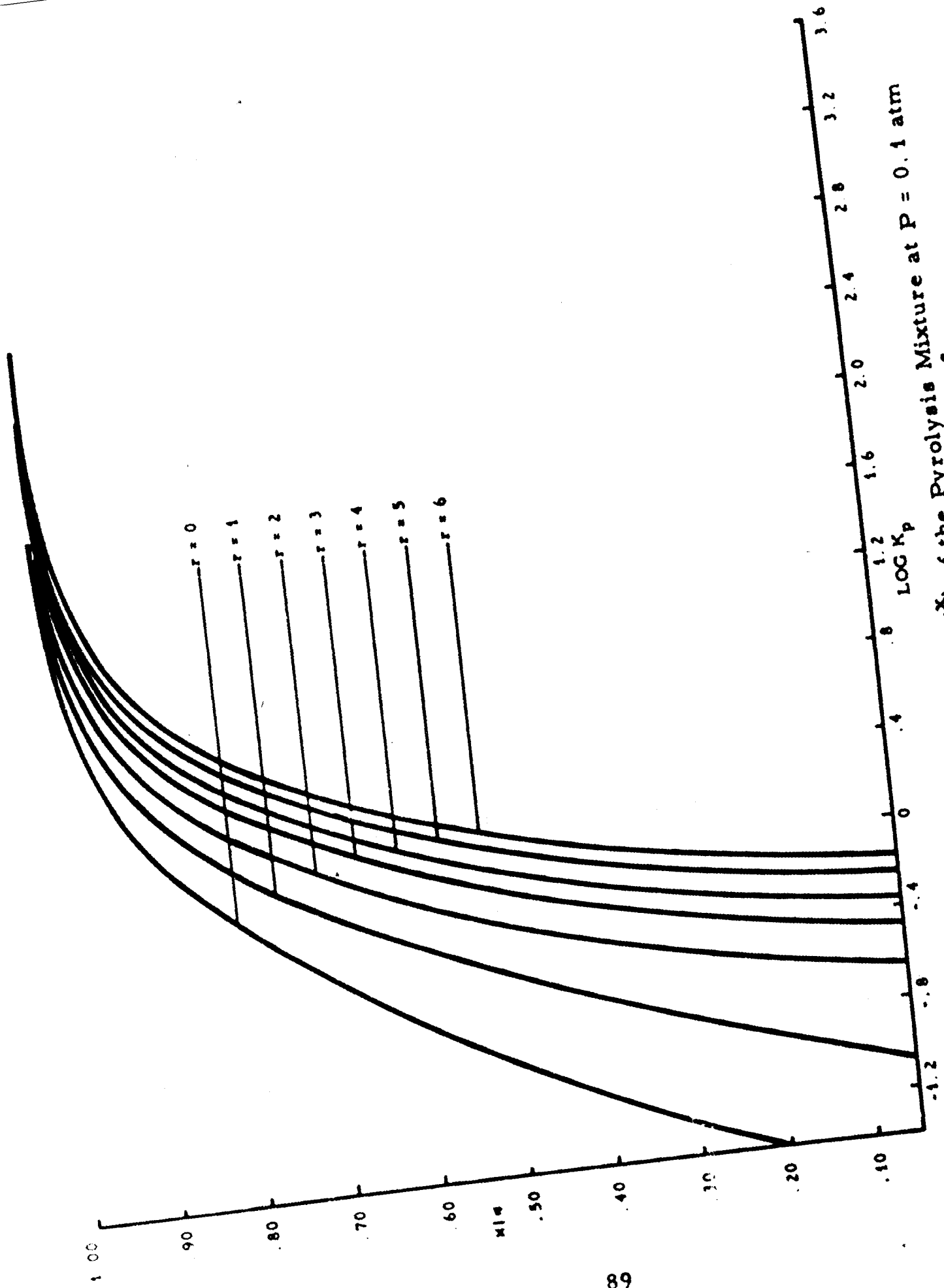


Figure 69. Equilibrium Composition ( $X_a$ ) of the Pyrolysis Mixture at  $P = 0.1 \text{ atm}$   
 6 Moles  $\text{H}_2$  Added to Give a Dilution Ratio  $r = \frac{b}{a}$

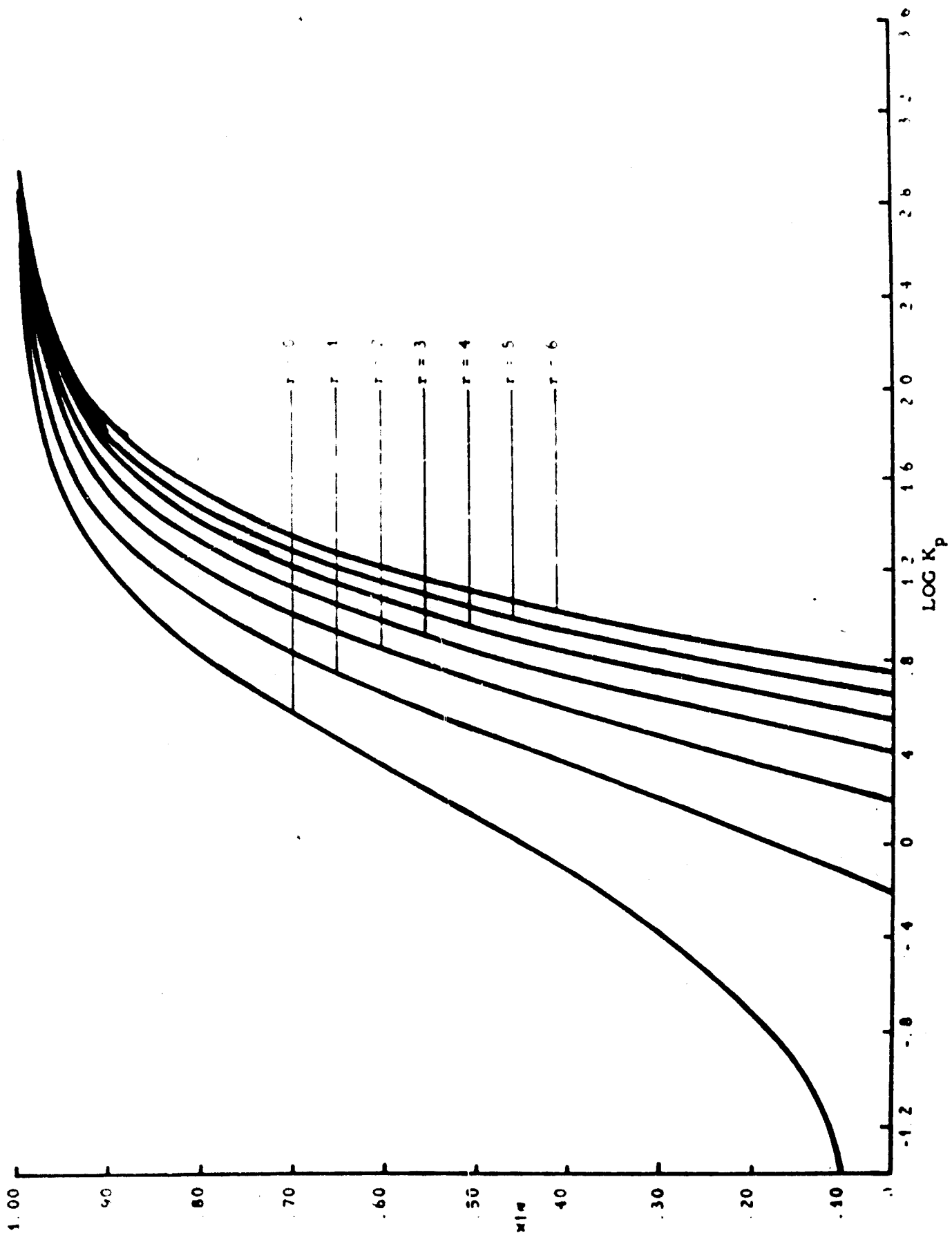


Figure 70. Equilibrium Composition ( $x_a$ ) of the Pyrolysis Mixture at  $P = 1$  atm  
 • Moles  $H_2$  Added to Give a Dilution Ratio  $r = \frac{b}{a}$

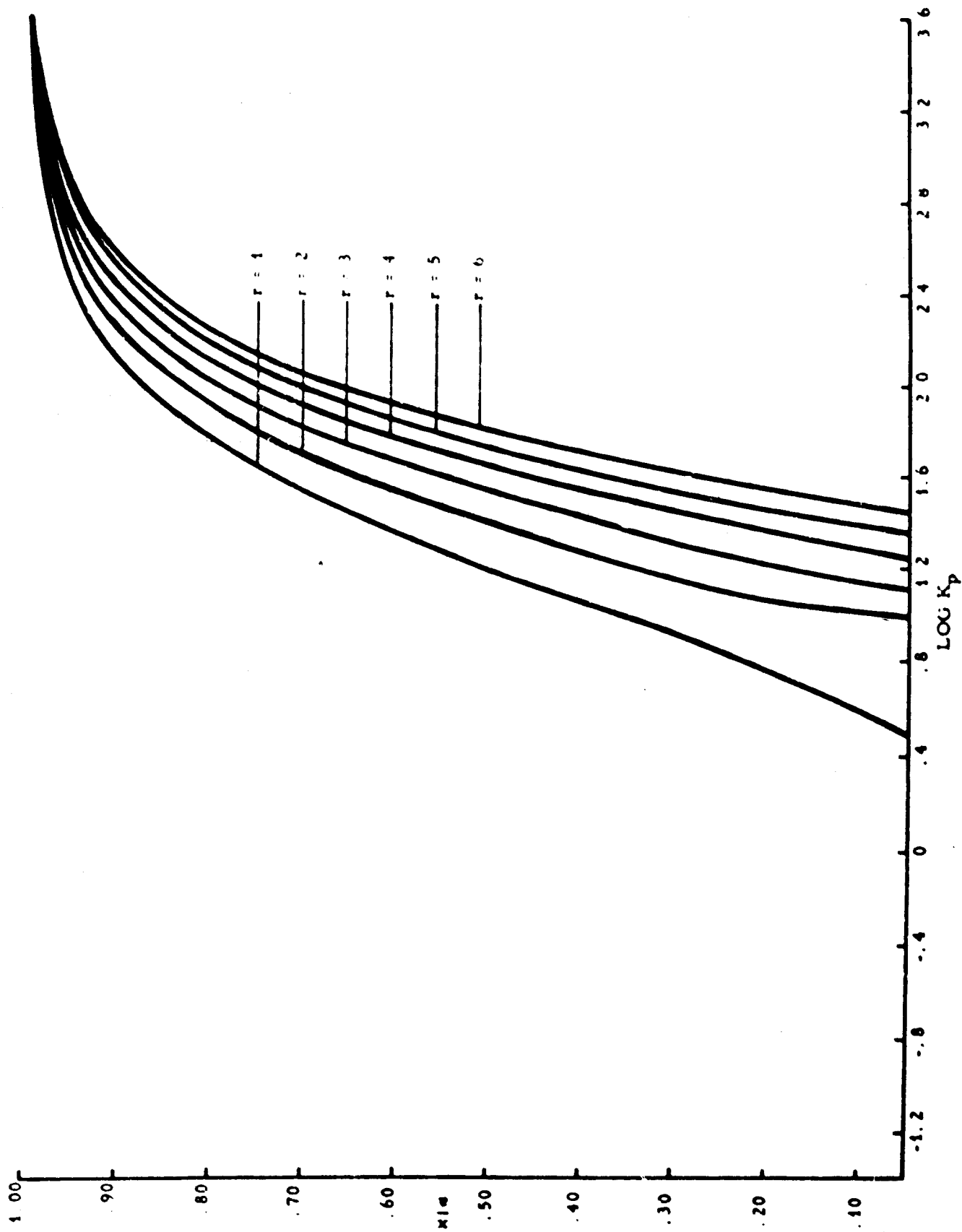


Figure 71. Equilibrium Composition ( $x_a$ ) of the Pyrolysis Mixture at  $P = 5 \text{ atm}$   
 5 Moles  $\text{H}_2$  Added to Give a Dilution Ratio =  $\frac{5}{2}$

Equation (18) has been used to give the maximum temperature for a given composition and total pressure which will give no carbon. Table 14 contains the results of the calculation of the solution to equation (18) at different hydrogen dilutions and total pressures. Figure 72 is a plot of the data in Table 14.

Table 14. Maximum Permissible Temperatures for Zero Yields of Carbon

	P = 0.1 atm T°C	P = 1 atm T°C	P = 5 atm T°C
r = 1	390	505	580
r = 2	440	570	660
r = 3	460	610	700
r = 4	480	635	740
r = 5	495	655	770
r = 6	510	670	800
r = 1/2	345	450	540

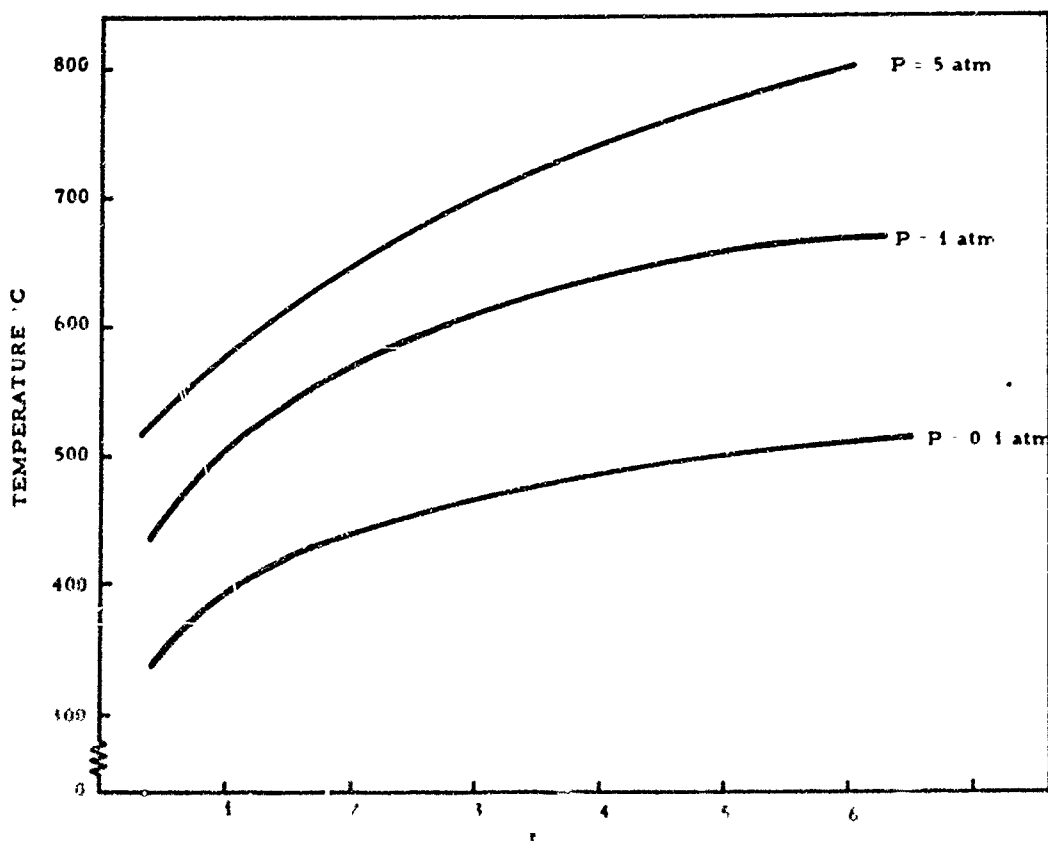


Figure 72. Maximum Permissible Temperatures for Zero Yields of Carbon

Equation (16) has been solved for the same pressure and temperature conditions as equations (14) and (15). The results of the calculations appear in Tables 15, 16 and 17. The plots of the data appear in Figures 73, 74 and 75. It is noteworthy that the equilibrium molar yield  $\frac{x}{a}$  is increased by increase of dilution with an inert gas.

Table 15. Equilibrium Composition of the Pyrolysis Mixture; Inert Gas Added, No Hydrogen Added

P = 0.1 atm

$K_p$	Log $K_p$	$\frac{x}{a}$		
		t = 1	t = 2	t = 3
.05	-1.301	.419	.477	.556
.1	-1.0	.541	.600	.677
.2	-0.699	.667	.721	.787
.3	-0.523	.734	.784	.840
.4	-0.398	.781	.823	.871
.5	-0.301	.812	.850	.892
.6	-0.222	.836	.870	.907
.7	-0.155	.855	.885	.918
.8	-0.097	.868	.897	.928
.9	-0.046	.881	.907	.934
1.0	0.00	.891	.915	.941
2	0.301	.940	.955	.969
3	0.477	.959	.969	.979
4	0.602	.969	.976	.984
5	0.699	.974	.981	.987
7	0.845	.982	.987	.991
10	1.00	.987	.990	.994
13	1.114	.990	.993	.995
16	1.204	.992	.994	.996
20	1.301	.994	.996	.997
25	1.398	.995	.997	.998
30	1.477	.997	.997	.998
40	1.602	.997	.998	.999
50	1.699	.998	.998	
100	2.00	.999	.999	
200	2.301	.999	1.000	
400	2.602	1.000	1.000	
800	2.903			

Table 16. Equilibrium Composition of the Pyrolysis Mixture;  
Inert Gas Added, No Hydrogen Added

P = 1 atm

K P	Log K P	$\frac{x}{a}$		
		t = 1	t = 2	t = 3
.05	-1.301	.151	.181	.226
.1	-1.000	.209	.248	.304
.2	-0.609	.281	.333	.402
.3	-0.523	.340	.393	.467
.4	-0.398	.383	.439	.517
.5	-0.301	.419	.477	.556
.6	-0.222	.450	.509	.588
.7	-0.155	.476	.536	.615
.8	-0.0969	.500	.560	.639
.9	-0.0458	.521	.580	.659
1.0	0.000	.541	.600	.677
2	0.301	.667	.721	.787
3	0.477	.736	.783	.840
4	0.602	.781	.823	.871
5	0.699	.812	.850	.892
7	0.845	.855	.885	.919
10	1.000	.891	.915	.941
13	1.114	.912	.933	.953
16	1.204	.927	.944	.962
20	1.301	.940	.954	.969
25	1.398	.944	.963	.975
30	1.477	.959	.968	.979
40	1.602	.969	.976	.984
50	1.699	.975	.981	.987
100	2.000	.987	.991	.994
200	2.301	.994	.995	.997
400	2.602	.997	.998	.999
800	2.903	.998	.999	.999
1,600	3.204	.999	1.000	1.000
10,000	4.000			
20,000	4.301			
50,000	4.699			

Table 17. Equilibrium Composition of the Pyrolysis Mixture;  
Inert Gas Added, No Hydrogen Added

P = 5 atm

.05	-1.301	.070	.085	.107
.1	-1.00	.093	.117	.148
.2	-0.609	.136	.163	.204
.3	-0.523	.165	.196	.244
.4	-0.398	.188	.223	.277
.5	-0.301	.209	.248	.304
.6	-0.222	.227	.268	.328
.7	-0.155	.244	.287	.350
.8	-0.0969	.259	.304	.368
.9	-0.0458	.273	.319	.386
1.0	0.00	.286	.334	.402
2	0.301	.384	.439	.517
3	0.477	.450	.508	.588
4	0.602	.500	.560	.638
5	0.699	.541	.600	.677
7	0.845	.602	.661	.733
10	1.00	.667	.721	.787
13	1.114	.713	.763	.803
16	1.204	.747	.794	.847
20	1.301	.781	.823	.871
25	1.398	.813	.850	.892
30	1.477	.836	.870	.907
40	1.602	.869	.897	.927
50	1.699	.891	.915	.941
100	2.00	.940	.954	.969
200	2.301	.969	.976	
400	2.602	.984	.988	.991
800	2.903	.992	.994	.996
1,600	3.204	.996	.997	
4,000	3.602	.999	.999	1.000
10,000		1.000.	1.000	

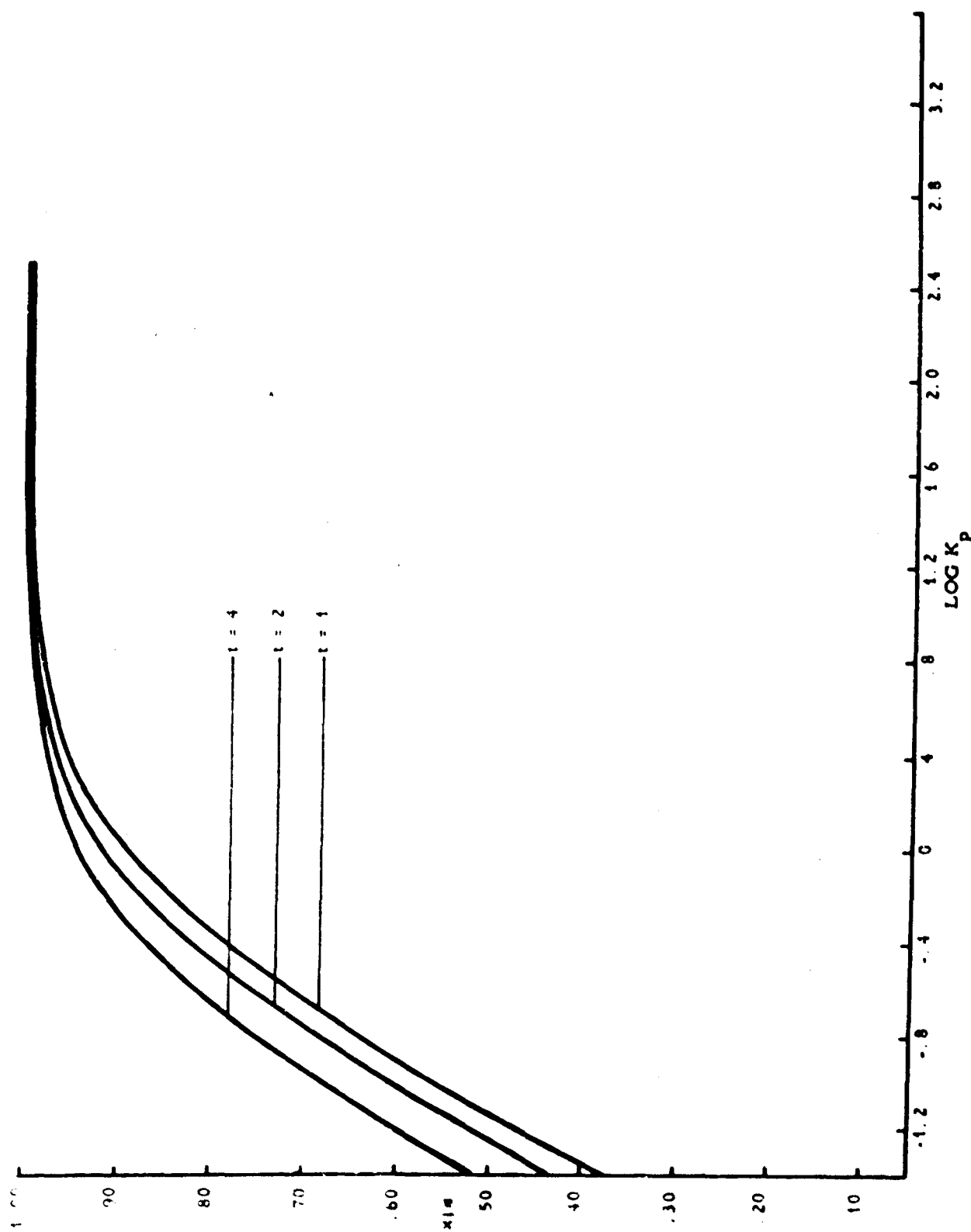


Figure 73. Equilibrium Composition ( $X_a$ ) of the Pyrolysis Mixture at  $P = 0.1$  atm  
 m Moles Inert Gas Added to Give a Dilution Ratio  $t = \frac{m}{a}$

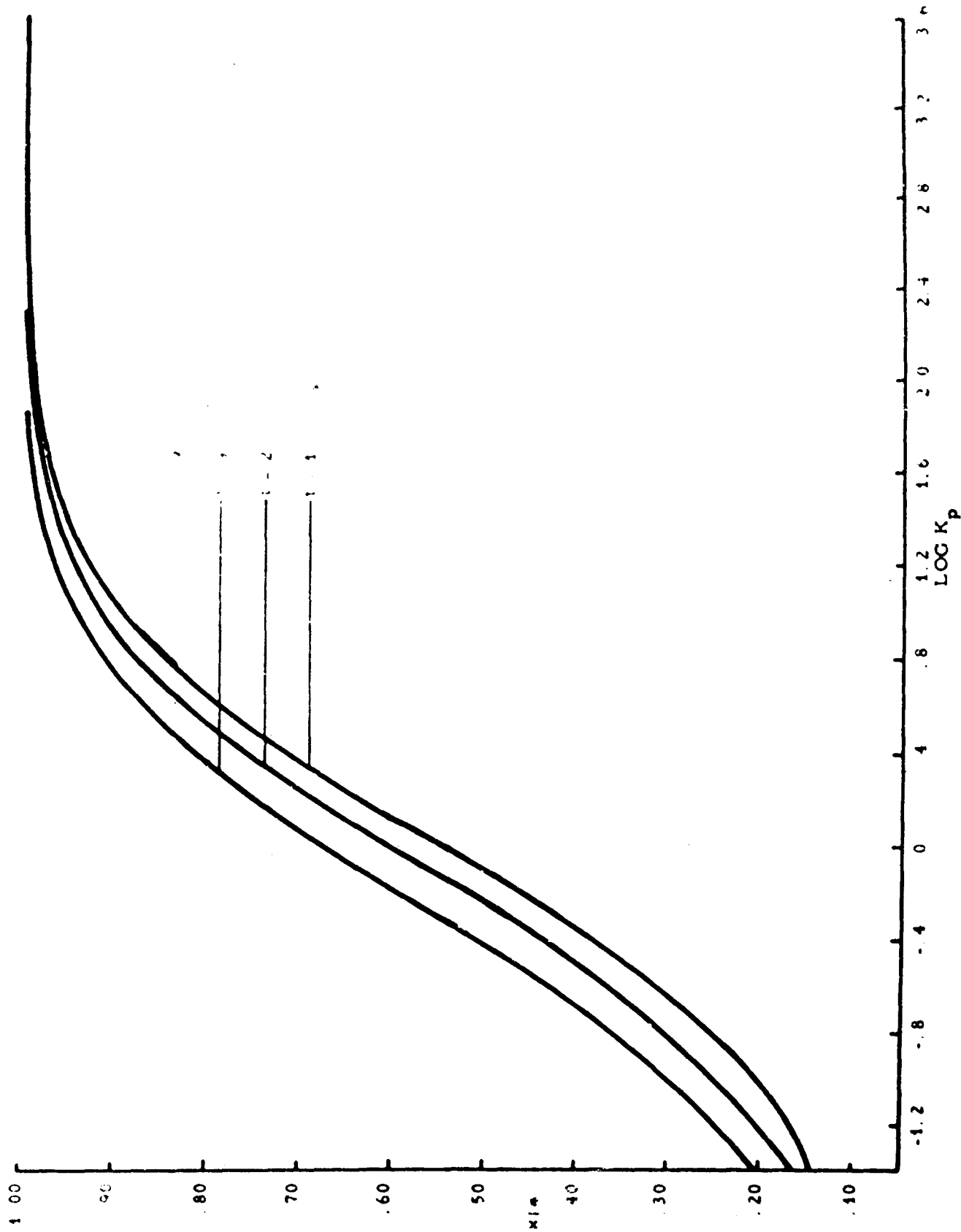


Figure 74. Equilibrium Composition ( $x_a$ ) of the Pyrolysis Mixture at  $P = 1$  atm  
 m Moles Inert Gas Added to Give a Dilution Ratio  $t = \frac{m}{a}$

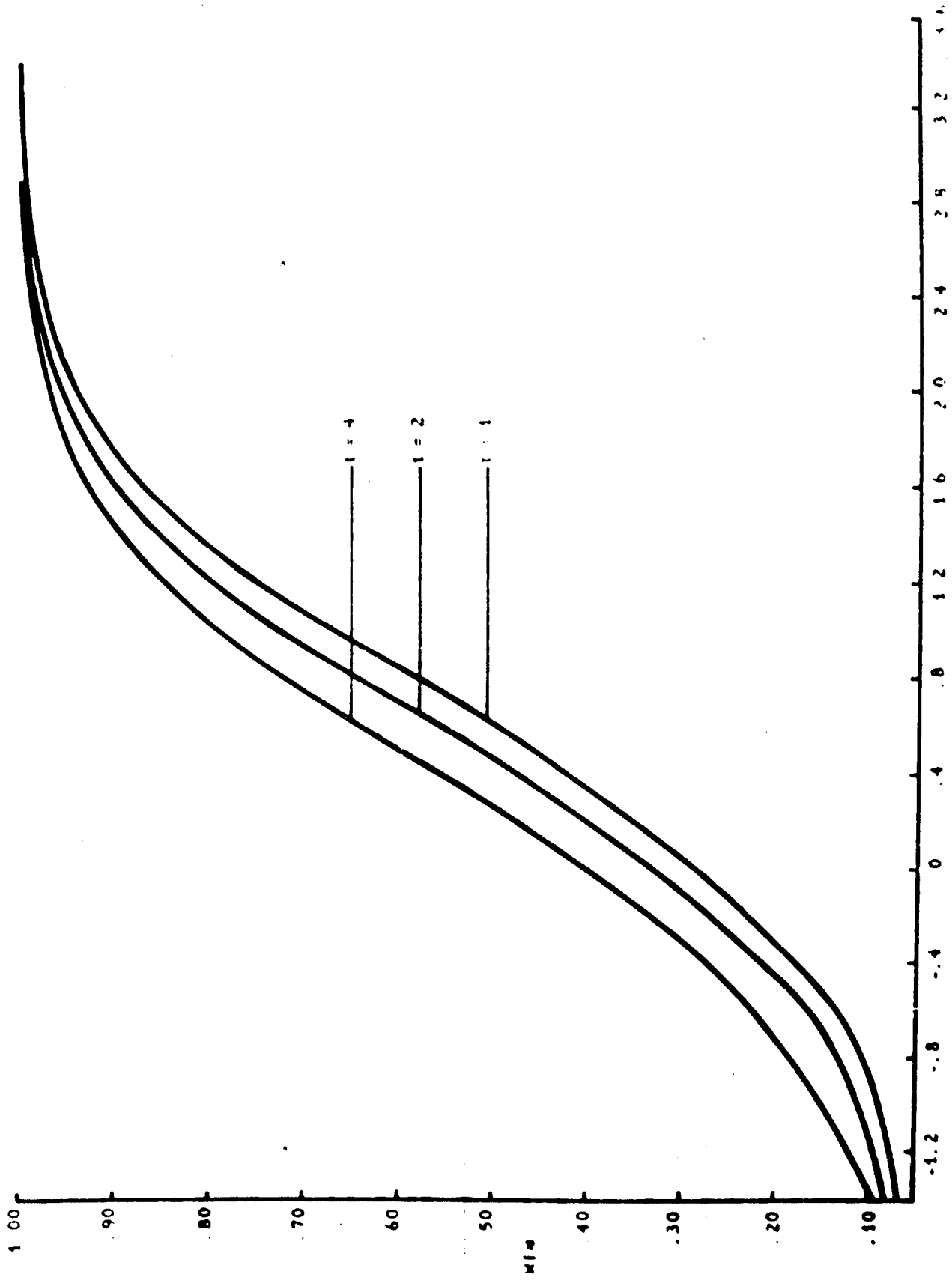


Figure 75. Equilibrium Composition ( $\frac{x}{a}$ ) of the Pyrolysis Mixture at  $P = 5$  atm  
 m Moles Inert Gas Added to Give Dilution Ratio  $t = \frac{m}{a}$